Near-field optical spectroscopy of two-dimensional materials

Mignuzzi, Sandro

Awarding institution:
King's College London

Near-field optical spectroscopy of two-dimensional materials

Sandro Mignuzzi

This dissertation is submitted for the degree of

Doctor of Philosophy

Department of Physics

King's College London

March 2017

Contents

List of Publications

Peer Reviewed Journals

1. B. R. Carvalho, Y. Wang, **S. Mignuzzi**, D. Roy, M. Terrones, C. Fantini, V. H. Crespi, L. M. Malard, M. A. Pimenta. *Intervalley double-resonance Raman scattering in 2D Molybdenum Disulfide*, Nature Communications, 8, 14670 (2017).

2. **S. Mignuzzi**, F. Huang, D. Roy, D. Richards, *Near-field Raman enhancement of single molecules and point scatterers*, submitted (2017).

3. T. Sainsbury, S. Gnaniah, S. J. Spencer, **S. Mignuzzi**, N. A. Belsey, K. R. Paton, A. Sattib, *Extreme mechanical reinforcement in Graphene oxide based thin-film nanocomposites via covalently tailored nanofiller matrix compatibilization*, Carbon, 114, 367 (2016)

4. W. Su, N. Kumar, **S. Mignuzzi**, J. Crain, D. Roy, *Nanoscale mapping of excitonic processes in single-layer MoS_2 using tip-enhanced photoluminescence microscopy*, Nanoscale, 8, 10564 (2016).

5. **S. Mignuzzi**, N. Kumar, B. Brennan, I. S. Gilmore, D. Richards, A. J. Pollard, D. Roy, *Probing individual point defects in graphene via near-field Raman scattering*, Nanoscale, 7, 19413 (2015).

6. **S. Mignuzzi**, A. J. Pollard, N. Bonini, B. Brennan, I. S. Gilmore, M. A. Pimenta, D. Richards, D. Roy, *Effect of disorder on Raman scattering of single-layer MoS_2*, Phys. Rev. B, 91, 195411 (2015).

7. N. Kumar, **S. Mignuzzi**, W. Su, D. Roy, *Tip-enhanced Raman spectroscopy: principles and applications*, EPJ Techn. Instrum., 2:9 (2015).

8. A. J. Pollard, N. Kumar, A. Rae, **S. Mignuzzi**, W. Su, D. Roy,

Nanoscale optical spectroscopy: an emerging tool for the characterization of graphene and related 2-D materials, J. Mat. Nanosci., 1(1), 39-49 (2014).

Conference Presentations (talks)

1. **S. Mignuzzi**, N. Kumar, A. J. Pollard, B. Brennan, D. Richards, D. Roy. *Tip-enhanced Raman spectroscopy imaging of graphene defects on the nanoscale*, Graphene Week, Manchester, UK 2015.

Conference Presentations (posters)

1. B. R. Carvalho, Y. Wang, **S. Mignuzzi**, D. Roy, M. Terrones, C. Fantini, V. H. Crespi, L. M. Malard, M. A. Pimenta. *Intervalley double-resonance Raman scattering in 2D Molybdenum Disulfide*, Graphene Week, Warsaw, Poland (2016).

2. **S. Mignuzzi**, A. J. Pollard, B. Brennan, D. Richards, D. Roy. *Raman spectroscopy of defective single-layer MoS_2*, Graphene Week, Manchester, UK (2015).

3. **S. Mignuzzi**, A. J. Pollard, B. Brennan, N. Bonini, D. Richards, D. Roy. *Characterisation of ion-bombarded single-layer MoS_2 with Raman spectroscopy*, Materials Research Society Spring Meeting and Exhibit, San Francisco, California, USA (2015).

4. **S. Mignuzzi**, A. J. Pollard, B. Brennan, N. Bonini, D. Richards, D. Roy. *Raman spectroscopy investigations of defective single-layer MoS_2*, NPL Graphene and 2-D Materials Conference, from Research to Applications, Teddington, UK (2014).

5. **S. Mignuzzi**, A. J. Pollard, S. J. Spencer, N. Bonini, D. Richards, D. Roy. *Raman spectroscopy of defects in single-layer transition metal dichalcogenides*, International Conference on Raman Spectroscopy, Jena, Germany (2014).

6. R. C. T. Howe, F. Torrisi, F. Tomarchio, **S. Mignuzzi**, A. C. Ferrari, T. Hasan. *Large-scale exfoliation of molybdenum disulphide in solvent mixtures*, ImageNano, Bilbao, Spain (2013).

Acknowledgement

I would like to express my sincere gratitude to my supervisors, Prof David Richards and Dr Debdulal Roy, for giving me the opportunity to pursue a joint PhD at the department of Physics of King's College London and at the National Physical Laboratory (UK). I am grateful for their continuous intellectual and financial support during my research project.

I also would like to sincerely acknowledge my PhD advisor, Dr Nicola Bonini, for his valuable assistance during the entire course of my PhD studies. I am grateful for his precious help with the density functional theory calculations presented in Chapter 4.

Big thanks go to Prof Marcos Pimenta and Mr Bruno Carvalho, for helpful and insightful discussions on the Raman spectrum of defective MoS_2. The outcome of this productive collaboration is reported in Chapter 4.

Very special thanks to the outstanding individuals I have had the privilege of working with at the National Physical Laboratory on a daily basis. Particularly, special recognition must be given to Dr Andrew Pollard. I have benefited a great deal from his incredibly optimistic and hard-working attitude, and I learned a lot from his impressive leadership and management skills.

I acknowledge Dr Barry Brennan and Dr Ian Gilmore for their help with the ion bombardment of the graphene and MoS_2 samples using the state-of-the-art secondary ion mass spectrometry instrument available at the National Physical Laboratory.

I am also really grateful to Naresh Kumar and Dr Weitao Su for sharing with me their expertise on the tip-enhanced Raman spectrometer.

Thanks to Ali Rae for providing valuable assistance with optical instrumentation.

I acknowledge funding from the Innovation Research and Development Programme of the National Measurement System, UK, Projects No. 115948 and 118616.

On a personal note, I would like to thank my parents and friends for their continuous support and unconditional encouragement during my PhD studies.

Abstract

Real materials contain structural defects which significantly affect their properties. Defects, in a general sense, are ubiquitous and encompass the diverse variety of elements capable of disrupting the continuity and translational symmetry of a crystalline lattice, both in terms of its structural morphology, and in terms of local modulation of its electrical and optical properties. In this perspective, atomic vacancies, line vacancies, atomic rearrangements, local doping inhomogeneity, chemically adsorbed adatoms, all fall within the broad category of defects. Thus, the nanoscale details of surface structure plays a pivotal role in understanding the impact defects may have on the overall properties of the material, and this is particularly true for "all-surface" materials such as two-dimensional (2-D) crystals. Even the interface between two atomically thin layers has a strong impact on the electronic and optical properties of few-layered stacks; therefore, also the interface associated with stacking and layer orientation can be viewed as an extend defect in two dimensions.

While macroscopic morphological characterization methods can provide averaged information over a lateral extent defined by their spatial resolution, high resolution (i.e. nanoscale) imaging has the potential to unveil important insights into the role of defects that dominate several aspects of surface chemistry and physics. On the one hand, defects in 2-D materials can be seen as deleterious as they may alter their electrical, chemical, magnetic and mechanical properties. On the other hand, the intentional creation of nanoscale defects may offer an additional degree of freedom for engineering their properties. In this perspective, having structural defects can be either

detrimental or beneficial, depending on the targeted application.

Despite the ever expanding literature on the study of the interplay between defects and the optical, electrical and mechanical properties of two dimensional materials, direct and non-destructive imaging of defect formation at the nanoscale remains a significant challenge. Although techniques such as electron microscopies or scanning tunnelling microscopy can be used to resolve individual lattice defects, they may be destructive or restricted to specific (e.g. conductive) substrates.

This thesis presents a nanoscale optical investigation of 2-D materials, such as graphene and single-layer MoS_2, with a particular focus on the characterisation of defects.

The field enhancement at the tip-apex of a metal-coated atomic force microscopy (AFM) tip is used to decrease the spatial resolution beyond the diffraction limit. In the case of the investigation of Raman scattering, this near-field optical technique is known as tip-enhanced Raman spectroscopy (TERS).

TERS is here demonstrated to be a valid technique to probe the distribution of point-like defects at the nanoscale, especially in the case of barely defective graphene. An analytical model to describe near-field imaging of point-like Raman scatterers, which is of general applicability to zero-dimensional scatterers such as molecules, is presented. The near-field image, constructed from the Raman intensity, is found to depend on the Raman tensor and the orientation of the scatterer. The model can be also used to explain the different values of near-field Raman enhancement observed for different Raman bands.

Motivated by the successful optical characterization of defects in graphene by means of Raman spectroscopy, it is now timely to expand the study of structural defects to other 2-D materials, such as semiconducting transition metal dichalcogenides. MoS_2 is one of the most prominent members of this newly discovered category of chalcogenide monolayers.

Defect-induced Raman scattering of single-layer MoS_2 is studied by means of a controlled introduction of defects using ion-bombardment. Phonon confinement is used to explain the evolution of peak widths and shifts, and a

metric based on Raman intensities is proposed to quantify defects. To gain insight into the defect-induced Raman processes, polarised and resonance Raman spectroscopy are employed.

1

2-D Nanomaterials

In the past four decades silicon-based electronics has proven to follow Moore's law, which states that the number of transistors per chip roughly doubles every two years. This demanding trend has been so far enabled by the continuous improvement of current technology, targeting the progressive reduction of the gate length of transistors. However, silicon-based technology has almost reached its integration limit, thereby triggering a common effort in the scientific community towards development of new materials and technology that could lead to realistic venues towards replacement of silicon. In this context, 2-D materials exfoliated from their bulk counterpart are receiving a growing interest[1] thanks to their remarkable electrical, optical and mechanical properties.

In layered materials, atoms within each layer are held together by covalent bonds, while weak van der Waals interactions keep the layers together. The existence of these materials in the form of single layers was theoretically proven to be impossible[2–4], due to Mermin-Wagner theorem, which

states that a 2-D, perfectly flat crystal is not stable at non-zero temperature because of thermal fluctuations. However, the ripples and corrugations observed in these atomically thin materials may provide reasons for their stability[5]. The first 2-D material to be intensely investigated over the last decade was graphene, a monolayer of carbon atoms packed into a 2-D honeycomb lattice[6]. It is a gap-less semi-metal that shows remarkable electronic properties, including an exceptionally high carrier mobility[7] exceeding 10^6 $cm^2V^{-1}s^{-1}$. Many other layered materials are now known to be exfoliable down to a single layer, the most promising candidates for opto-electronics applications being transition metal dichalcogenides[8], featuring metallic and semiconducting properties that cover the $1-2$ eV band-gap range, and hexagonal boron nitride, an insulator with 5.9 eV bandgap[9]. Amongst layered transition metal dichalcogenides, MoS_2 is a subject of intense research because of its electronic[10] and optical properties[11], such as strong PL[11,12], electroluminescence[13], controllable valley and spin polarisation[14,15]. In a not-too-distant future, it is hoped that this wide variety of 2-D materials could be used to form complex electronic heterostructures (only a few atoms thick) that may become the building blocks for future flexible and transparent electronics.

1.1 Graphene

1.1.1 Structure

Graphene is an allotrope of carbon consisting of a monolayer of carbon atoms packed into a 2-D honeycomb lattice[6]. It is the building structural unit for many carbon materials of other dimensionalities, such as 3-D graphite, 1-D carbon nanotubes and 0-D fullerene[6]. Graphite consists of coherently stacked layers of graphene which are arranged in a ABA structure (known as "Bernal Stacking"), held together by weak interlayer van der Waals forces, resulting in a interlayer spacing of 0.335 nm[16].

The carbon electronic configuration is $1s^2\ 2s^2\ 2p^2$, with the $2s$ and $2p$ orbitals combining together to form hybrid orbitals sp^i $(i = 1, 2, 3)$. In graphene $2p_z$, $2p_x$ and $2p_z$ orbitals form three sp^2 hybridized orbitals, which

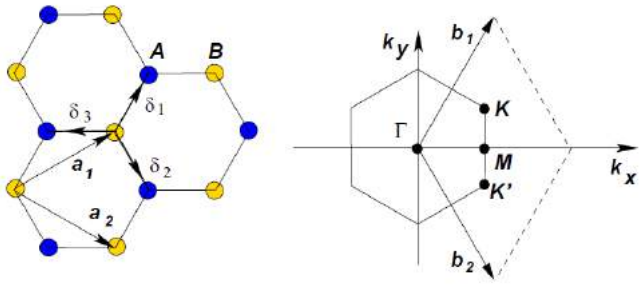

Figure 1.1: On the left: the lattice structure of graphene, consisting of two interpenetrating triangular lattices (A and B). On the right: corresponding Brillouin zone. **K** and **K'** denote the Dirac points.[17]

are arranged at an angle of 120°, forming σ covalent bonds with neighbor atoms. The bond length is a_{c-c}=0.142 nm[16]. The $2p_z$ orbital is perpendicular to the basal plane and remains free, determining the optical and electronic properties of graphene.

The following nomenclature will be used throughout this thesis: single layer graphene (SLG), few-layer graphene (FLG), multilayer graphene (MLG).

1.1.2 Electronic Properties

The graphene structure can be seen as a triangular lattice with a basis of two atoms per unit cell[17] (Fig.1.1), forming a hexagonal lattice. The lattice vectors can be written as:

$$a_1 = \frac{a}{2}(\sqrt{3}, 1), \qquad a_2 = \frac{a}{2}(\sqrt{3}, -1), \tag{1.1}$$

where $a = \sqrt{3}a_{c-c}$=0.246 nm is the lattice constant. In the reciprocal space, the first Brillouin zone is also hexagonal. The reciprocal lattice is defined by vectors given by:

$$b_1 = \frac{2\pi}{a}(\sqrt{3}, 3) \qquad b_2 = \frac{2\pi}{a}(\sqrt{3}, -3). \tag{1.2}$$

The low-energy electronic band structure of graphene can be well described by a tight-binding Hamiltonian. Near **K** or **K'** in the Brillouin zone

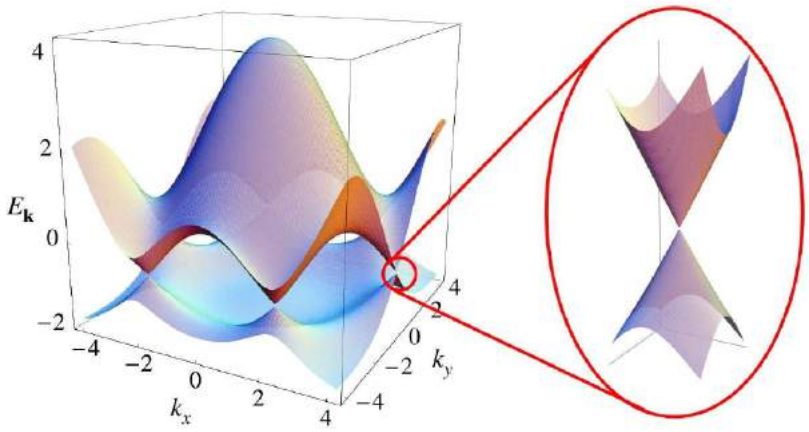

Figure 1.2: Energy band structure of graphene, and a zoom-in of the energy bands close to one of the Dirac points.[17]

(see Fig. 1.1), the electronic dispersion is linear (Fig.1.2):

$$E^{\pm}(\kappa) = \pm\hbar\nu_F|\kappa|, \tag{1.3}$$

where $\kappa = \mathbf{k} - \mathbf{K}$, ν_F is the Fermi (electronic group) velocity: $\nu_F = \sqrt{3}\gamma_0 a/2\hbar \sim 1 \times 10^6 m/s$, γ_0 is the hopping energy between first neighbour π orbitals, the $\mathbf{k}= (k_x, k_y)$ vectors represent the ensemble of the available electronic momenta, and $\mathbf{K}= \frac{2\pi}{3a}(1, \frac{1}{\sqrt{3}})$ is the vector, in the momentum space, representing the position of the **K** point of the Brillouin zone.

Eq.1.3 describes touching cones at the **K** and **K'** points. Owing to this linear dispersion, electrons in graphene behave like Dirac fermions (**K** and **K'** points are also called "Dirac points"). In undoped graphene, the Fermi energy level E_F resides at the Dirac points whereas it increases (decreases) in the presence of n- (p-) doping.

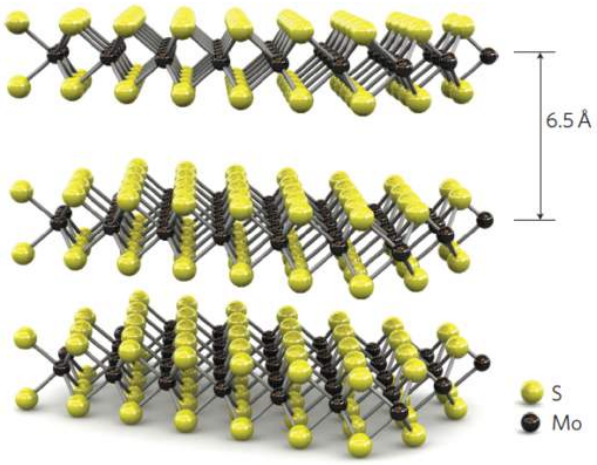

Figure 1.3: Three dimensional representation of the structure of MoS_2.[10]

1.2 Molybdenum Disulfide

1.2.1 Structure

Molybdenum Disulfide (MoS_2) belongs to the family of transition metal dichalcogenides. It is composed of a layered structure, held together by van der Waals forces. The crystal structure of the MoS_2 sheets is depicted in Fig.1.3, consisting of two sublattices, for Mo and S atoms respectively. Due to the chemical ratio Mo:S=1:2, the Mo sublattice layer is sandwiched between two nearby S sublattice layers. The thickness of a MoS_2 sheet is about 0.313 nm[18]. Most few-layered transition metal dichalcogenides exhibit a Bernal stacking, but deviations from this stacking configuration are also possible, especially when transition metal dichalcogenide layers are stacked manually via transfer techniques.

1.2.2 Optoelectronic Properties

MoS_2 has technologically interesting optoelectronic properties, as its band structure changes from bulk to single layer, thus giving rise to different band

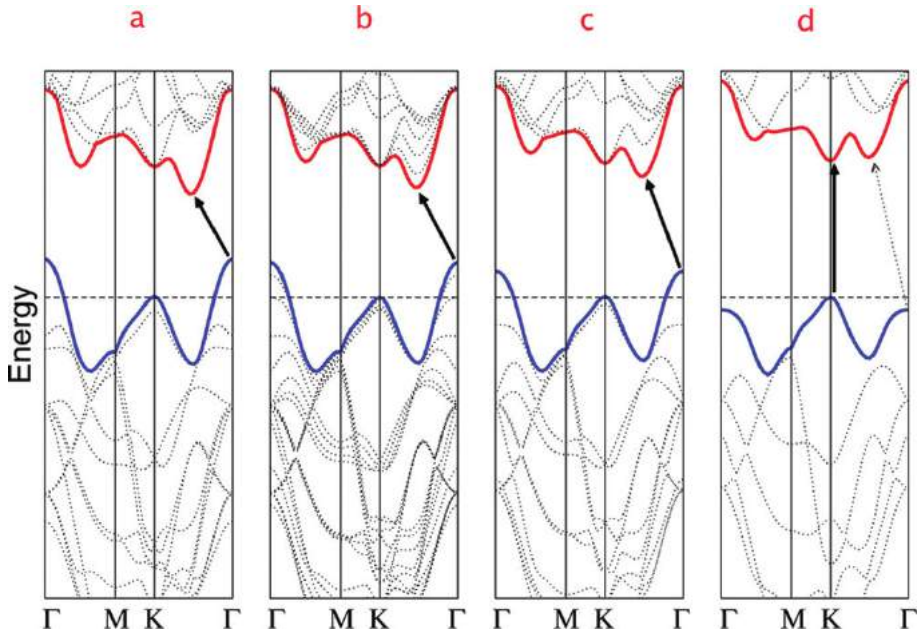

Figure 1.4: Calculated band structures of (a) bulk MoS_2, (b) quadrilayer MoS_2, (c) bilayer MoS_2, and (d) monolayer MoS_2. The solid arrows indicate the lowest energy transitions. Bulk MoS_2 is characterized by an indirect bandgap. The direct excitonic transitions occur at high energies at **K** point. With reduced layer thickness, the indirect bandgap becomes larger, whereas the direct excitonic transition barely changes. Monolayer MoS_2 in (d) becomes a direct bandgap semiconductor.[12]

gap values (Fig.1.4). The change of bandgap in MoS_2 from indirect to direct is reflected in its photoconductivity[11], absorption[11] and PL[11,12].

By considering infinitely wide single S-Mo-S sheets, stacked with ABA sequence with intersheet distance w fixed to the bulk value, it is possible to calculate the variation of the band gap in multilayer MoS_2 sheets as a function of the number (N) of layers. The calculated band gap monotonically increases from bulk to the single layer, starting from 1.29 eV when N tends to infinity, (bulk material) to 1.8 eV for the single layer[11,12,19]. In the case of a MoS_2 bilayer composed of two single sheets stacked in an AB configuration, the bandgap increases monotonically with w; when the inter-sheet separation is greater than 0.45 nm, the gap reaches the value found for a single sheet, as the inter-sheet interaction vanishes[19]. Note that both AB-stacked sheets contain three atomic layers (S-Mo-S) and that w refers to the z-axis distance

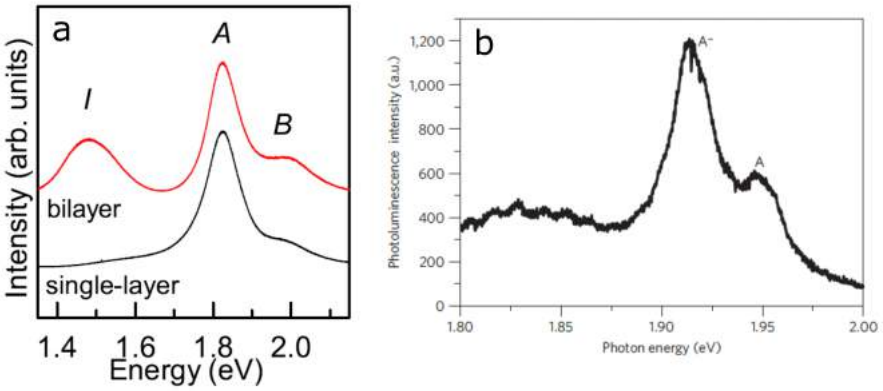

Figure 1.5: (a) PL spectra of single-layer and bilayer MoS_2 on Si/SiO_2 substrate excited with 2.33 eV. The transitions I, A, and B are indicated. Adapted from Ref.20. (b) PL spectrum of a monolayer MoS_2 sample on a h-BN substrate at a temperature of 10 K with fully resolved exciton (A) and trion (A^-) emission. Adapted from Ref. 21

between the upper S layer of sheet B and the lower S layer of sheet A [19].

As bulk MoS_2 is an indirect semiconductor with a band gap of 1.29 eV, it does not show any PL. Its absorption spectrum is constituted by two excitonic transitions, namely A (≈1.8 eV) and B (≈2.0 eV), originating from the **K** point of the Brillouin zone. When the thickness of MoS_2 is reduced to few layers the material starts showing an increasingly intense PL signal, which becomes most prominent in monolayer MoS_2. Such emerging PL has been attributed to the increase of the indirect band gap due to confinement effects, which leads to the transition to a direct semiconductor.

Figure 1.5(a) shows the PL spectra of bilayer (red curve) and monolayer (black curve) MoS_2. For the former, the A and B excitonic features are accompanied by a low-energy feature (I), which has been attributed to the indirect gap in Ref. 11. In monolayer MoS_2, the A excitonic feature can be accompanied by an additional peak, such that the overall PL signal can be deconvoluted into the neutral A exciton peak, also commonly referred to as A^0 (located at ≈660 nm), an A^- peak (at ≈670 nm), attributed to negatively charged trions [14], along with the B excitonic peak. The A^- peak has been found to originate from bound states of two electrons to a hole,

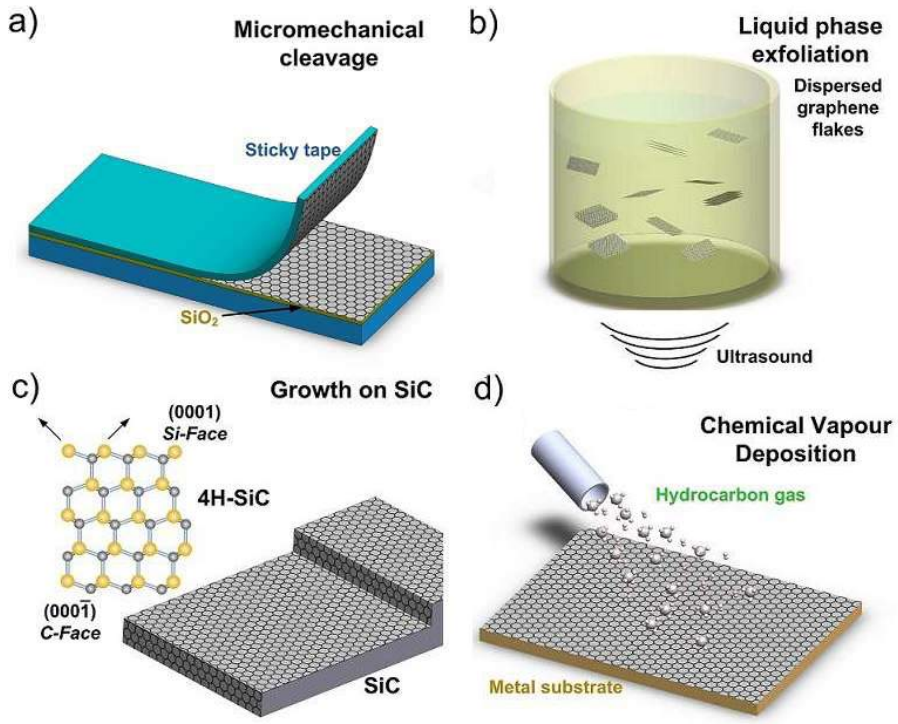

Figure 1.6: Schematic illustration of the main graphene production techniques. (a) Micromechanical cleavage. (b) Liquid phase exfoliation.(c) Growth on SiC. (d) Chemical vapor deposition. Adapted from Ref. 22.

i.e. negatively charged excitons. Both the exciton and trion features can be generally identified in the PL of monolayer MoS_2 at room temperature, although the resonances are significantly broadened. Low-temperature PL measurements allow resolving the A and A^- peaks unambiguously, as shown in Figure 1.5(b).

1.3 Synthesis of 2-D Materials

This section briefly reviews the most common methods to produce graphene and related 2-D materials.

Micromechanical Cleavage Micromechanical cleavage is the first method used to produce individual 2-D nanosheets from layered materials,

and has been widely employed to prepare graphene[1] and MoS_2[10,23]. This method involves peeling off a piece of material by means of an adhesive tape[1], as shown in Fig. 1.6a. The produced monolayers can achieve up to millimetres in size and have high structural and electronic quality[24]. The graphene and MoS_2 flakes used throughout this thesis have been produced by mechanical exfoliation. As the flakes have been subjected to progressive and controlled introduction of defects, it was particularly important to start with a highly crystalline material in the first place, allowing reliable collection of a benchmark Raman spectrum, representative of the pristine condition. Flake sizes of $\approx 10\ \mu m$ can be achieved for MoS_2 and other transition metal dichalcogenides[25]. Due to the low yield, this method is suitable just for fundamental research, and is thus impractical for large-scale applications.

Chemical Vapour Deposition Chemical Vapour Deposition (CVD) is a process used in the semiconductor industry to produce high-purity thin films. Volatile precursors reacts and/or decompose on a substrate, building up the film (see Fig. 1.6d).

This method has been used to grow monolayer graphene films on a variety of metal substrates by feeding a source gas (such as methane) at a suitable temperature. One of the first substrates used was nickel. The main growth mechanism on this substrate is carbon segregation at metal surfaces and grain boundaries. The grain size of such a graphene is relatively small and there is often presence of multilayers at the metal grain boundaries. This is mainly due to the high solubility of carbon in nickel that causes carbon atoms to precipitate into the metal during the growth. Thin nickel films and fast cooling process can be used to avoid this. However, this process leads to thicker graphene layers as well as to presence of structural defects. Graphene can also grow on copper substrates[26], where carbon solubility is very low. In this case, the grow mechanism is a surface-catalyzed process. It is possible to achieve larger grain size and single layer graphene with less than 5 % of the total area featuring thicker flakes.

CVD was recently adopted to synthesize MoS_2 layers on insulating substrates[27–29], using solid precursors (such as S and MoO_3 powders) heated to

high temperature[27,30].

Epitaxial Growth Epitaxial growth of a material refers to the formation of a crystal on top of a crystalline substrate that exhibits a similar structure (see Fig. 1.6c). The substrate used for graphene is SiC[31]. Under high temperature (>1000 °C) and ultra-high vacuum, SiC (Si(0001)- or C(000$\bar{1}$)-terminated) undergoes graphitisation, a process first proposed in 2012 by Charrier et al.[32], due to the evaporation of Si atoms.

Liquid Phase Exfoliation Liquid-phase exfoliation involves dispersing the material in solvents, with the help of ultrasonication, as shown in Fig. 1.6b. To produce graphene, both water[33–36] and organic solvents[34,37,38] have been used; for the synthesis of transition metal dichalcogenide nanosheets, successful solvents were similarly found[39], including mixtures[40].

1.4 Raman spectroscopy of 2-D materials

Raman scattering is the inelastic scattering of photons by phonons. In a classical framework, the electromagnetic field of the incident light induces in a medium an oscillating dipole which acts, in turn, as an emitter of radiation at the Rayleigh frequency (corresponding to the frequency of the incident light) and at the Raman frequency. A deeper understanding of the origin of Raman light can be obtained using a full quantum mechanical description that involves photons, electronic transitions, and electron-phonon scattering events. Raman scattering happens when, with a much lower probability than Rayleigh scattering, the incident photon loses (or gains) energy in the interaction process with phonons in the medium, thus exiting the sample with a slightly lower (or higher) energy.

Raman spectroscopy is an integral part of graphene and 2-D materials research[41]. The absence of a bandgap in graphene makes Raman scattering a resonant process in the visible range, thus the Raman spectrum contains information about the electronic properties of graphene[41]. The Raman spectrum of graphene can be utilised to determine the number of layers, level of

disorder, defects and edges, strain, doping, presence of functional groups and perturbation due to magnetic fields[41]. Raman spectroscopy is also becoming of interest to characterise other 2-D materials, such as single-layer MoS_2[42–44].

Raman Spectrum of Graphene

Graphene has two atoms per unit cell, thus six normal vibrational modes (Fig.1.7(a)), which transform at the **Γ**-point (centre) of the Brillouin zone, according to the $A_{2u}+B_{2g}+E_{1u}+E_{2g}$ representation of the D_{6h} point group[45,46]. The E_{2g} and B_{2g} are optical modes whereas A_{2u} and E_{1u} are acoustic modes. The Raman spectrum of graphene is presented in Fig. 1.7(b) and consists of several bands which can be normally Raman-active or can be activated by the presence of defects (the spectrum is restricted to one- and two-phonon peaks). In Fig. 1.7(c) the phonon dispersion of graphene is reported, as it is essential to interpret its Raman spectrum. In general, first-order one-phonon processes at **Γ** are Raman-active if their group symmetry is correct and if they satisfy the fundamental Raman selection rule, i.e. the phonon wave

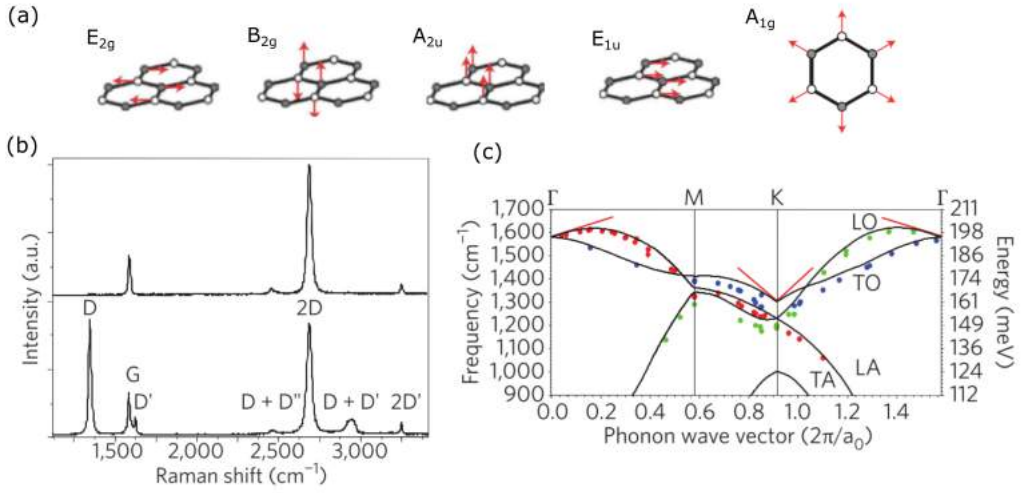

Figure 1.7: (a) **Γ**-point phonon displacement patterns for graphene vibrations. Inequivalent carbon atoms are distinguished using empty and filled circles. Red arrows show atom displacements. (b) Raman spectrum of pristine (top) and defective (bottom) graphene. (c) Phonon dispersion relation of graphene. Red lines indicate Kohn anomalies. Adapted from Ref. 41.

vector $\mathbf{q} \approx 0$. As will be described below, the fundamental Raman selection rule can be satisfied also by any pair of phonons with opposite momenta, **q** and -**q**, giving rise to two-phonon processes in the spectra.

The G-peak ($\approx$ 1580 cm^{-1}) is due to the in-plane bond stretching of all pairs of sp^2 atoms; it corresponds to a one-phonon (E_{2g}) process originating from the degenerate LO and TO branches at the **Γ**-point[41]. The D-peak is due to the breathing modes of six-atom rings and originates from TO phonons in proximity of the **K**-point of the Brillouin zone[41]. The D-peak is a one-phonon process but does not obey the fundamental Raman selection rule, and indeed requires a defect in order to be activated. The activation mechanism of the D-peak is an inter-valley double-resonance, where the phonon connects two points belonging to two different cones (at **K** and **K'**) in the electronic dispersion[47–52]. An equal and opposite momentum, in order for the overall momentum to be conserved, is given by the defect. Due to a Kohn anomaly at **K** in the phonon dispersion, the D-peak is strongly dispersive with excitation energy[53]. Intra-valley processes, where the phonon connects two points belonging to the same cone (at **K** or **K'**), give rise to the defect-activated D'-peak, which is due to LO phonons in proximity to (but not at) the **Γ**-point[41,54]. The 2D- and the 2D'-peak are overtones of the D- and D'-peaks, respectively. Finally, the D+D" peak is assigned to a combination of one D- and one D"-phonon, the latter belonging to the LA branch at $\approx$ 1100 cm^{-1}. Contrary to the D"-peak, D+D" requires no defects in order to be activated. An overview of the main Raman processes in graphene is reported in Fig. 1.8. Double and triple resonance processes are depicted in Fig. 1.8(b-g, j,k) and 1.8(h,i,l) respectively. Defect-activated peaks (D and D') will be discussed in detail in the following section.

Defect-activated processes Graphene edges can be regarded as extended defects, as they break the translational symmetry of the crystal, and are in general constituted by a combination of zigzag and armchair segments[55,56]. In the Raman processes (D and D') involving one phonon and one defect (or edge), two conditions need to be satisfied[55]: (i) since the electron and the hole, generated by the incident radiation, have opposite momentum, the

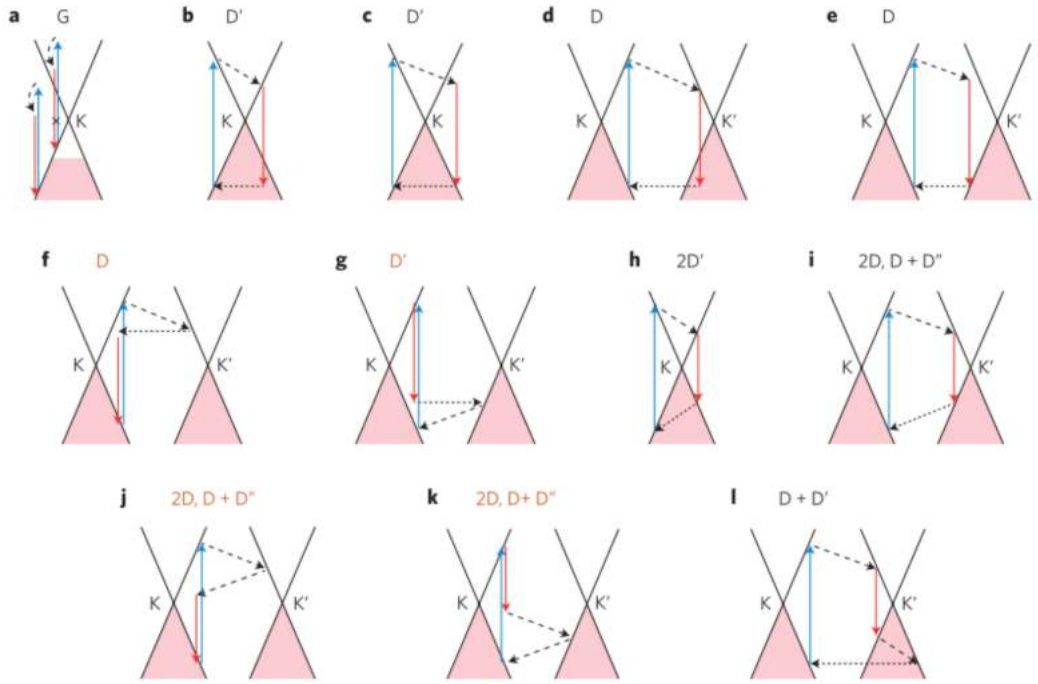

Figure 1.8: Raman processes. Electron dispersion (solid black lines), occupied states (shaded areas), interband transitions neglecting the photon momentum, accompanied by photon absorption (blue arrows) and emission (red arrows), intraband transitions accompanied by phonon emission (dashed arrows), electron scattering on a defect (horizontal dotted arrows). (a) One-phonon processes responsible for the G peak, which interfere destructively. Some processes can be eliminated by doping, such as the one that is crossed out. (b-g) In the presence of defects, the phonon wave vector need not be zero, producing the D' peak for intravalley scattering (b,c), and D peak for intervalley scattering (d-f). Besides the e-h or h-e processes, where the electron and the hole participate in one act of scattering each (b-e), there are contributions (e-e, h-h) where only the electron (f) or the hole (g) are scattered. (h-k) For two-phonon scattering, momentum can be conserved by emitting two phonons with opposite wave vectors, producing the 2D' peak for intravalley scattering (h) and the 2D, D+D" peaks for intervalley scattering (i-k). The e-e and h-h processes are shown in (j, k, l). With defects, one intravalley and one intervalley phonon can be emitted, producing the D+D' peak. The processes (f, g, j, k) give a small contribution, as indicated by the orange peak labels. Adapted from Ref. 41

.

phonon and defect scattering need to be back-scattering events, in order for the electron-hole pair to recombine (Fig. 1.9(a)); (ii) the phonon wavevector

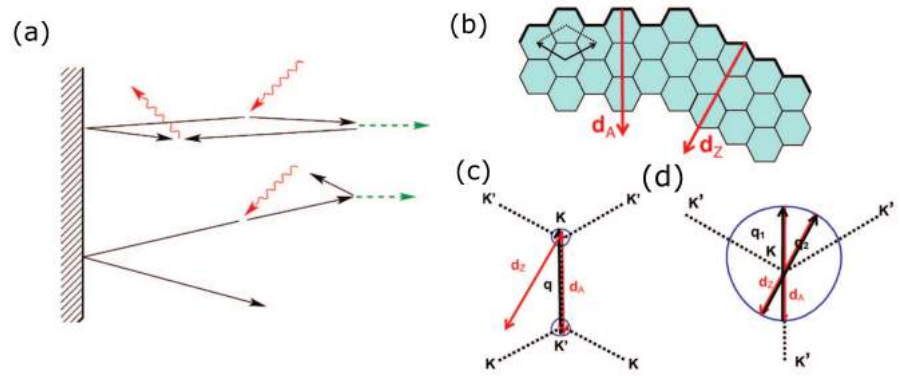

Figure 1.9: (a) Scattering processes involving one phonon (green arrow) and one defect. Red lines indicate incident photons, generating electron-hole pairs, and scattered photons from the recombination of electron-hole pairs. Black arrows indicates quasi-classical trajectory of electron and holes. The upper scheme depicts a backscattering process, with normal incidence, giving rise to a defect-activated Raman peak. The bottom part depicts a scattering process where an oblique incidence impedes the electron-hole pair to recombine. (b) Wavevector directions for the backscattering process by armchair ($\mathbf{d}_A$) and zigzag ($\mathbf{d}_Z$) edges. (c) Schematic of the intervalley process giving rise to the D-peak, where only $\mathbf{d}_A$ connects two valleys of the electron dispersion. (d) Schematic of the intravalley processes giving rise to the D'-peak. Adapted from Ref.55.

needs to connect two points in the electronic dispersion (double resonance). The D-peak can be produced only by armchair edges[55,56], as perfect zigzag edges cannot scatter electrons between **K** and **K'**. This can be seen in Fig. 1.9(b,c) where the wavevectors in real and reciprocal space ($\mathbf{d}_A$ for armchair and $\mathbf{d}_Z$ for zigzag edges), for the backscattering processes, are reported. On the other hand, the D'-peak can be activated both by armchair and zigzag edges as intravalley scattering is allowed (Fig. 1.9(b,d)). It is interesting to consider the D-peak Raman process in real space, as one can see how the D-peak is localised in proximity to a graphene edge or a defect. As it can be seen in Fig. 1.8(d,e), in the Raman scattering process giving rise to the D peak, at least one of the elementary scattering processes bring the electron (hole) into a virtual state; that is, energy conservation is violated by an amount of the order of the phonon energy, $\hbar\omega_D \approx 0.17$ eV. As a consequence, the electron-hole pair lifetime can be calculated, from the uncertainty principle,

as $1/\omega_D \approx$3 fs. The length scale of this process corresponds to the distance travelled over the lifetime of the virtual electron-hole pair, $V/\omega_D \approx 4$ nm, where $V \approx 1.1 \times 10^6$ m/s ≈ 7.3 eV $\cdot\hbar$ is the electron velocity (the slope of the Dirac cones).

Raman Spectrum of single-layer MoS_2

Single-layer MoS_2 has D_{3h} symmetry[57]. An unit cell consisting of one Mo and two S atoms leads to 9 normal vibrations, which decompose at the $\mathbf{\Gamma}$ point into the following irreducible representation: $A_1' + E'' + 2A_2'' + 2E'$. The A_1', E', and E'' symmetries correspond to Raman active modes[57]. The two main first order Raman peak of monolayer MoS_2 are located at ≈403 cm^{-1} and ≈384 cm^{-1}, and they correspond to one of the two E' modes, and to the A_1' mode, respectively. The latter is an out-of-plane vibration of only S atoms in opposite directions. The E' and A_1' peaks are denoted as E^1_{2g} and A_{1g}, respectively, for the case of multilayer MoS_2, as the group symmetry of the crystal varies with its thickness[57]. In the following, the E', A_1' notation will be adopted for monolayer MoS_2 only, whereas the general E^1_{2g}, A_{1g} notation will be used for multilayer MoS_2. The other modes are either infrared (IR) active, or they require an uncommon scattering geometry involving a polarization along the out-of-plane z component, i.e. parallel to the c-axis of the crystal (or, equivalently, perpendicular to its basal plane) and they are thus normally not observed in a backscattering Raman setup.

The Raman characterization of exfoliated MoS_2 is less developed in comparison to the rich amount of work performed on the Raman spectrum of graphene, and the interpretation of its spectrum is still the subject of intense debate in the scientific community. For instance, attempts have been made to infer the number of MoS_2 layers from its Raman peaks, similarly to what has been reported for the 2D peak of graphene. Lee et al.[43] reported a dependence of the E^1_{2g} and A_{1g} peak frequencies on the number of layers, intensities and widths in ultra-thin MoS_2 flakes. Li et al.[23] confirmed the monotone variation of the E^1_{2g} and A_{1g} peak frequencies with thickness, but did not find a thickness dependence of their intensities and widths. In par-

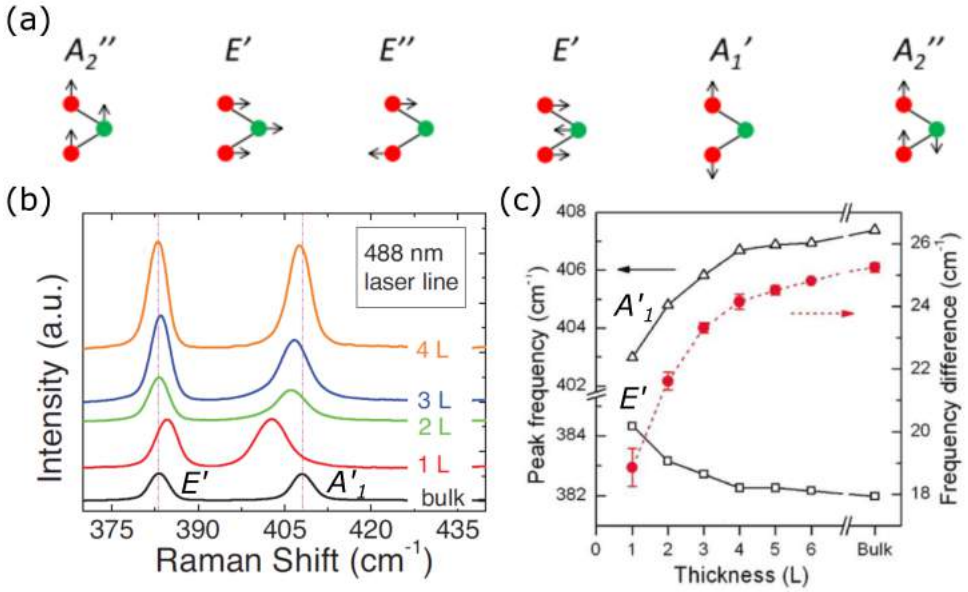

Figure 1.10: (a) Single-layer MoS_2 normal modes of vibration. Adapted from Ref. 57. (b) Raman spectra of MoS_2 flakes with different thicknesses. The left and right dashed lines indicate the positions of the E^1_{2g} and A_{1g} peaks in bulk MoS_2 respectively. Adapted from Ref.[23]. (c) Experimental peak frequency of A'$_1$ and E' and their difference as a function of thickness. Adapted from Ref. 43.

ticular, it was found that the frequency of the E^1_{2g} peak decreases whereas that of A_{1g} increases with increasing layer number (Fig.1.10). This trend can be explained as follows. With an increasing number of layers, the interlayer van der Waals force suppresses atomic vibrations, resulting in higher force constants and therefore in an increase of frequency[58]. The blue-shift of A_{1g} is consistent with this interpretation, whereas the red-shift of E^1_{2g} suggests that other interactions take place. This anomalous behaviour may be attributed to long-range Coulombic interlayer interactions and may reflect the influence of stacking-induced structural changes[43]. Despite the large amount of work on the the D and D' peaks for graphene, which are indicative of the degree of disorder within the crystalline lattice, no comprehensive report on the interplay between disorder and the Raman peaks of MoS_2 has been so far presented in the literature. This will be the subject of Chap. 4, for the case of monolayer MoS_2.

2

Experimental set-up and techniques

2.1 Near-field optical spectroscopy

Tip-enhanced Raman spectroscopy (TERS) combines the chemical sensitivity of surface enhanced Raman spectroscopy (SERS) with the high spatial resolution of scanning probe microscopy (SPM), thus enabling chemical imaging of surfaces at the nanometre length-scale. The concept of TERS was first proposed by Wessel in 1985[59], and it was experimentally realised in 2000[60–62]. Since then, TERS has rapidly progressed to become a non-destructive SPM tool for surface chemical characterisation[63], and opened up the opportunity to study single macro molecules with sub-nm spatial resolution[64]. Over the last 15 years, the technique has been used to study scientific problems in biology[65], photovoltaics[66], catalysis[67], semiconductors[68], carbon nanotubes[69], graphene[70] and single molecule detection[64].

Unlike electron spectroscopy and microscopy techniques such as scanning electron microscopy (SEM), transmission electron microscopy (TEM) and X-ray photoelectron spectroscopy (XPS) that require vacuum for their operation, TERS can be used in an ambient environment and it is also well-suited for the investigation of samples in aqueous media[71,72]. Although super-resolution fluorescence microscopy techniques can be used for imaging of biological samples below the diffraction limit, the fluorescent labels prevent observation of the samples in their native state[73]. Being a label-free technique, TERS can be used to study the molecules directly, particularly for investigating chemical composition and molecular dynamics in biological samples. Therefore TERS applications on biological samples such as pathogens[74], lipid and cell membranes[75], nucleic acid[76], peptides[77] and proteins[78] have drawn a significant interest.

2.2 Plasmon-mediated enhancement mechanism

A sharp metal or metal-coated SPM tip is positioned at the centre of a laser focus, and the electromagnetic (EM) field at the tip-apex is confined and enhanced due to a combination of localised surface plasmon (LSP) resonance and lightning rod effect (enhancement hot spot, due to curvature induced electric-field enhancement). Such EM field increase enhances the Raman signal from target objects (e.g. molecules) in the vicinity of the tip apex and enables nanoscale chemical imaging of surfaces, overcoming the diffraction limit of SERS and conventional Raman spectroscopy.

The optical properties of metals such as gold, silver, copper, aluminium arise from the presence of free conduction electrons. The free electrons of a metal can move in a background of fixed positive ions, which ensures overall neutrality. This system forms a plasma, that is generally refereed to as free-electron plasma. Being a collective motion of the free electrons as a whole, a plasmon is a quasi-particle representing the elementary oscillations, or modes, of the charge density oscillations. Such oscillation, if not

maintained by an external source of energy, undergoes decay through various loss mechanisms (collisions etc.). The characteristic oscillation frequency is given by the free-electron plasma frequency. In a metal nanoparticle (which can be seen as an approximation of the tip apex), the plasmon oscillates locally around the nanoparticle centre with a frequency known as the LSP resonance. The oscillation frequency is determined by several factors: the density of electrons, the effective electron mass, and the shape and size of the charge distribution. Therefore, the optical response of metal nanoparticles can be tuned by controlling their size, shape, and dielectric environment. The shape effect manifests itself as two concomitant phenomena: (i) firstly, a shift of the LSP resonance (which is ultimately responsible for the EM enhancement); (ii) secondly, a modification of the local field enhancement on the particle surface. In general, larger sizes lead to red-shifted (i.e. moved to longer wavelengths), broadened LSP resonances. The redshift is due to the onset of so-called retardation effects (i.e. the conduction electrons do not all move in phase anymore).

2.3 Tip-enhanced optical spectroscopy set-up

The experimental TERS work presented in this thesis is based on an inverted microscope system. A schematic of the setup is shown in Fig. 2.1. A Raman spectrometer (iHR320 Horiba Scientific, UK), is coupled with an AFM system (CombiScope 1000, AIST-NT, The Netherlands). A 532 nm diode laser, matching the plasmonic resonance of the Ag tips, is used to excite the sample. The illumination wavelength is thus selected to match the plasmon resonance position of the metal tip apex. Generally, the spectral profile of the plasmon resonance is broad (≈100 nm). Au tips often exhibit plasmon resonances in the 600-800 nm range. Furthermore, TERS experiences Raman enhancement not only via the amplification of the incident light, but via the Raman scattered light, with the relative amplitudes of the enhancement being related to the strength of the plasmon at the spectral position of both the excitation and Raman emission wavelengths. Therefore, the Raman signal is enhanced by $(E/E_0)^4$, where E is the enhanced

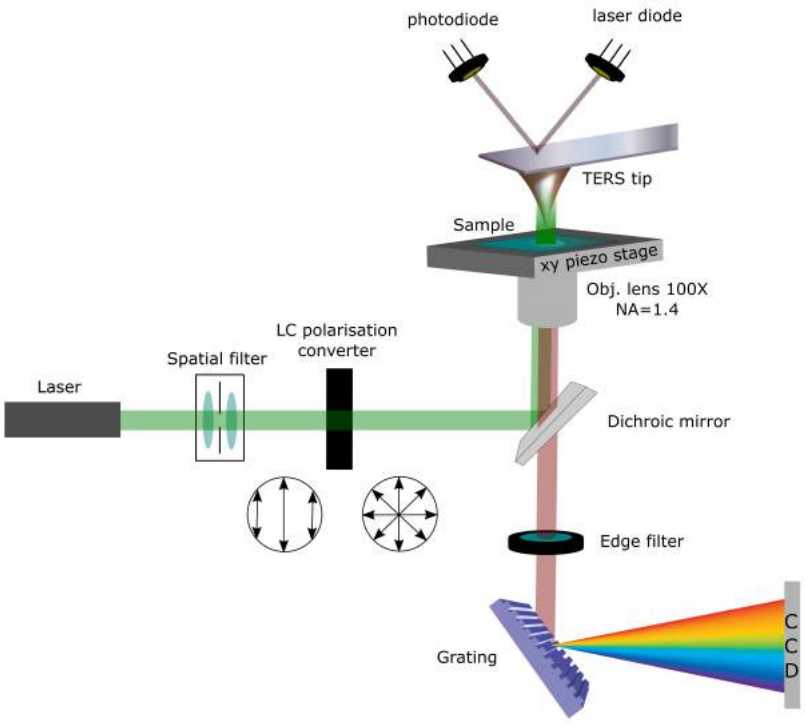

Figure 2.1: Transmission-mode tip-enhanced optical set-up used in thesis. The green and red light paths corresponds to the excitation laser and the Raman scattered light, respectively.

electric field and E_0 is the excitation electric field. As a consequence, it is usually desirable to utilise an excitation wavelength relative to the tip apex plasmon spectrum such that the enhancement is high at both the excitation and Raman-scattered wavelengths. The linearly polarised laser light initially passes through a spatial filter, which is used to remove the unwanted multiple-order energy peaks and unwanted components due to scattered light. The polarisation is converted to radial by means of a liquid crystal polarisation converter (ARCoptix, Switzerland), which will be described in detail later. A dichroic mirror directs the light to an oil immersion 100× objective lens (numerical aperture, NA=1.4) which focuses it on the sample, positioned on a 170 μm-thick glass coverslip. The sample is supported and controlled by a xy piezo translational stage. A Ag-coated AFM probe is used, with tip apex in contact with the sample and aligned with the focal spot. The Ra-

man scattered light is collected from the same objective and dichroic mirror. The excitation light is blocked using an edge filter. The Raman light is analysed in the spectrometer using one of the gratings available (300, 600 and 1800 lines/mm) depending on the level of spectral resolution needed, and an electron multiplying CCD (EMCCD) detector (Newton, Andor Technology, Ireland).

2.3.1 Laser polarisation

The laser polarisation is a critical parameter in TERS, as the tip enhancement is maximised when the laser polarisation is parallel to the tip axis. In the setup used in this work, this can be achieved using a radially polarised beam which, when tightly focused using a high-NA objective lens, gives rise to a strong longitudinal polarisation at the focal spot [79,80] (Fig. 2.2a). In order to obtain a radially polarised beam at the back aperture of the objective, a liquid crystal polarisation converter is used. A schematic of the converter, shown in Fig.2.2b, consists of three components: the polariser converter itself (θ-cell), a retarder cell and a polarisation rotor. The retarder cell is divided in an upper and a lower part. The upper part of the retarder cell can be controlled electrically to change the inclination of the liquid crystal molecules. As a consequence, the phase of the upper part of the beam can be retarded in $\lambda/2$ steps, where λ is the wavelength of light. The polarisation rotor is also based on the rotation of liquid crystal molecules by means of an applied voltage. When the polarisation rotor is switched on, the polarisation is rotated by 90°. The entrance and the exit plates of the θ-cell are linearly and circularly rubbed, respectively. Azimuthally polarised light is achieved for light incident parallel to the rubbing direction. Radially polarised light is achieved for light incident perpendicular to the cell axis.

2.3.2 Tip alignment

TERS experiments are performed by raster-scanning the sample, using a xy-piezo stage, while keeping the tip and the focal spot aligned. The alignment procedure consists of three steps. The tip is roughly aligned with

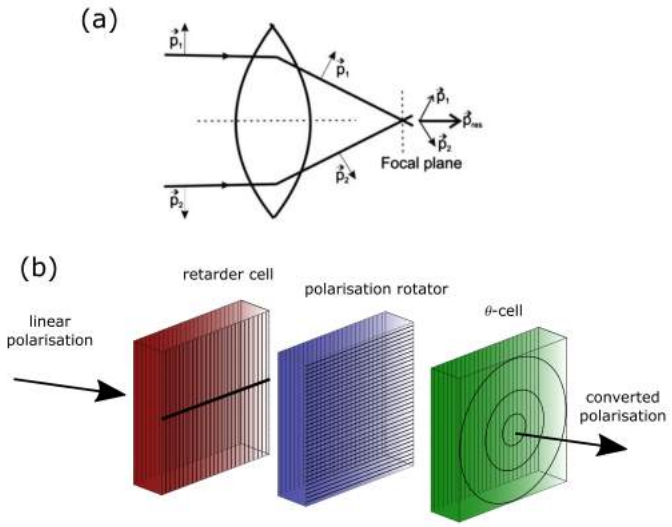

Figure 2.2: (a) Schematic representation of a radially polarised beam tightly focused on a focal spot via a high-NA lens, giving rise to a longitudinal polarisation. (b) Components of the polariser converting the beam linear polarisation to azimuthal or radial. Adapted from Ref. 80.

the optical view of a camera first. This is done by focusing a LED light 10 μm above the sample. The tip position in xy is then controlled by a stepper motor until the tip reaches the camera field of view. The second step is a rough alignment of the focal spot with the tip. The tip is landed on the sample and appears as a shadow spot in the optical view. The objective is controlled by a piezo scanner which moves it in the desired position. In the third step, the focal spot is finely aligned with the tip by progressively moving the objective while recording and maximising the Raman intensity. A typical objective map of this type is shown in Fig. 2.3. The maximum Raman or PL intensity, due to the plasmonic enhancement, is reached when the probe and the objective are aligned.

2.4 Tip fabrication

TERS probes are prepared through the thermal evaporation of a 50 nm thick Ag layer (pressure of 10^6 millibars and evaporation rate of 0.5/s) onto silicon AFM tips, purchased from MikroMasch (model HQ:CSC17/No Al).

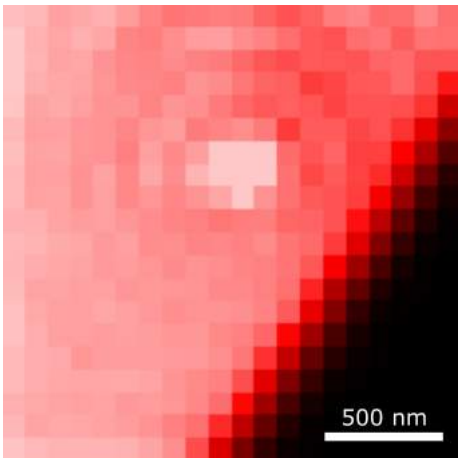

Figure 2.3: Photoluminescence objective map of a single-layer MoS_2 flake showing a 'hotspot' due to the presence of the tip landed on the sample.

The refractive index of the substrate material (silicon: n≅4.15 at 532nm) of the tip is modified by growing a 300 nm thick layer of wet oxide (silicon oxide: n≅1.46 at 532nm) in a furnace at 1000°C for 45 min, with water vapour flowing. With this method, the plasmon resonance of the metallic layer is blue-shifted, to reach the wavelength of interest (532 nm). This was shown in the literature both theoretically[81] and experimentally[82,83]. The tip radius of curvature is determined using SEM and is typically of ∼20-50 nm (Fig. 2.4 (a, b)).

Cleanliness of the Ag layer is particularly important in order to obtain signal enhancement and spectra free of Raman signatures from contamination. For this reason, the metal evaporator is maintained in a nitrogen gas environment of a glovebox. As-prepared probes are also stored in such environment in order to avoid the bulk oxidation of Ag. With this method the probes can remain functional for at least 6 months.

An alternative AFM operational mode can be used in order to perform tip-sample dependent optical measurements. For this purpose, robust knowledge of tip-sample distance during approach is needed. While it may be possible to perform such measurements using a contact mode AFM tip, which will be used for TERS imaging throughout this thesis, major challenges arise due to the cantilever deflection. During the closest phases of the approach,

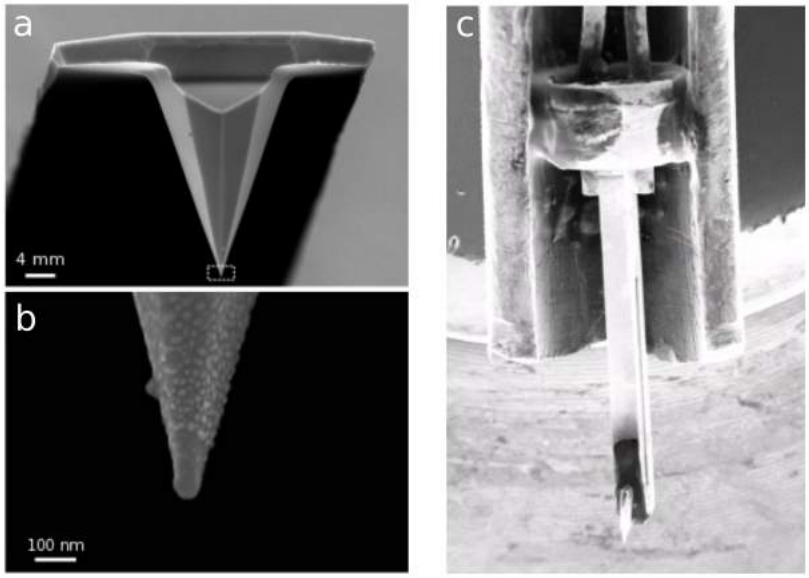

Figure 2.4: SEM images of near-field probes. (a) An oxidised and Ag-coated AFM tip; a close-up is shown in (b). (c) An electrochemically etched tip attached to a tuning fork.

the interaction exerted on the tip by the sample makes the former snap, hence it may be not be anymore assumed that the cantilever distance from the sample varies at the same pace as the tip-sample distance. An effective solution is enabled by lateral shear-force mode operation, based on metal tip attached to one prong of a quartz tuning fork (as shown in Fig. 2.4(c)), a rigid element not suffering from the above mentioned deflection issues.

The tuning fork takes advantage of the piezoelectric properties of crystalline quartz, whereby the application of a driving force (e.g. an oscillating voltage) is translated to a mechanical oscillation. The piezoelectric current generated as a result of the tuning fork mechanical oscillation can be subsequently measured. Both arms of the tuning fork move in the same direction, and the amplitude of the displacement of the tuning fork is detected by measuring an alternating current signal from the tuning fork. One should note that a perfectly balanced tuning fork would not produce any current as both arms would move exactly identically. Thus, the tip mounted parallel to one arm of the tuning fork (oscillating nearly parallel to the surface of

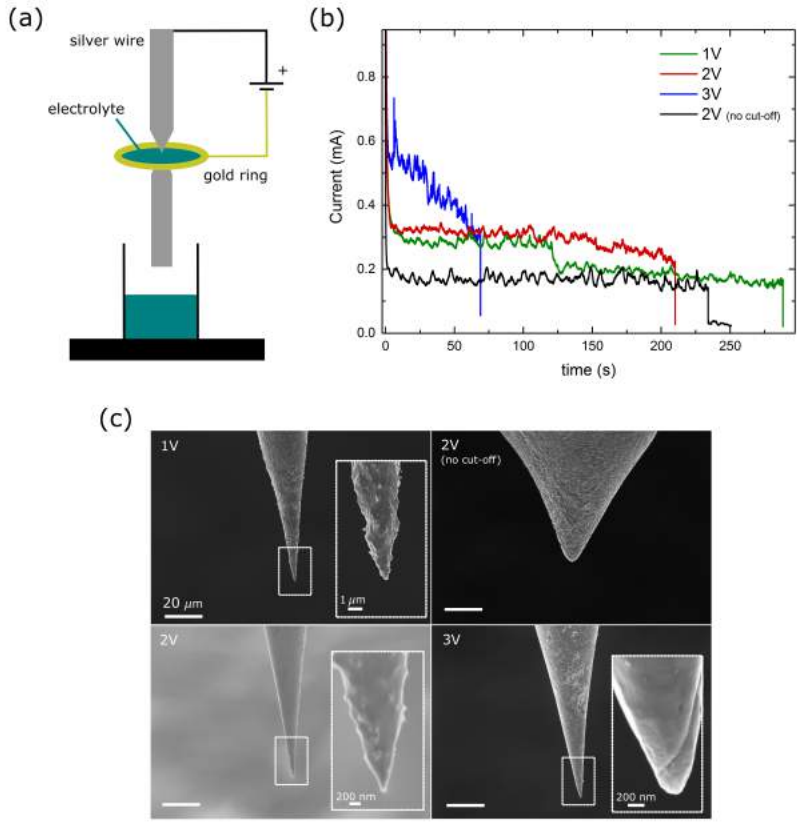

Figure 2.5: (a) Schematic of etching set-up for Ag tips. (b) Time evolution of the current during tip etching for different DC voltage applied: 1, 2, 3 V using a threshold cut-off, and 2 V without using threshold cut-off. (c) Tips corresponding to the curves in (b).

the sample), changes the mass and stiffness of that arm thus generating a net current. Under resonant conditions, the tuning fork arm has the biggest displacement that corresponds to the maximum oscillation amplitude. Upon approaching the sample, a variation of the oscillation frequency, accompanied by a decrease in the oscillation amplitude, is observed, due to tip-sample interaction. This results in a decrease in the output current signal, which is sent to an I-V converted and an amplifier to increase the signal-to-noise-ratio. The decreased output signal during tip-sample approach is compared with a set-point of a feedback circuit and the resulting difference is fed back to a scanner, in order to precisely control the probe-sample distance during scanning. Both the amplitude and the phase of the output signal can be used

as distance control parameter in the feedback system, however the phase has been found to result in an improved stability of the feedback system[84].

Electrochemical etching allows the fabrication of tips from Ag wires, that can then be attached to a tuning fork to be used in shear-mode or tapping-mode AFM. The experimental setup for electrochemically etched tip fabrication is shown in Fig. 2.5(a). A Methoohm Autolab system is used. The solvent is nitric acid, which has been reported to produce sharp Ag tips in literature[85]. A Au ring (from a 1 mm thick wire), with diameter of 1 cm, acts as the cathode electrode whereas the Ag wire (100 nm thick) acts as the anode electrode. A membrane (or lamella) is first created in the Au ring by immersion in nitric acid. The Ag wire is carefully immersed in the membrane. The application of a voltage between the Ag wire and the Au ring etches away the Ag. The tip is formed on the upper part of the wire as soon as the lower part of the wire drops off. Any further etching after this point is avoided by opening the circuit. This can be controlled by setting a threshold for the change in current over time (dI/dt). Fig. 2.5b shows the variation of the current over time during the etching for different voltages. The SEM images of the respective probes are shown in Fig. 2.5c.

3

Near-field Raman scattering from point-like scatterers and defects in graphene

3.1 Introduction to Raman spectroscopy of defective graphene

Raman spectroscopy is widely used to characterise the quality of graphene layers. The issue of quantifying the level of disorder in sp^2 carbon materials via Raman spectroscopy has been investigated since the pioneering work by Tuinstra and Koenig[48], which reported the presence of a defect-induced Raman peak at $\cong$ 1340 cm^{-1} in nanocrystalline graphite, now commonly known as the D-peak (see Section 1.4 for further details). This was assigned to a breathing mode with A_{1g} symmetry at the **K**-point of the Brillouin

zone, and an inverse proportionality relationship was established between the relative intensity of the Raman D- and G-peaks, i.e. $I(\mathrm{D})/I(\mathrm{G})$, and the crystallite lateral size[48].

In the following years, several works focused on the origin of the D- and D'-peaks in graphite and on the use of Raman spectroscopy to quantify crystallite size, defect concentration and defect type. In graphene research, the physical origin of $I(\mathrm{D})/I(\mathrm{G})$ has been investigated by various groups[86–88], by systematically introducing point defects via ion-bombardment. Lucchese et al.[86,87] have studied ion-bombarded graphene by varying the density, n_D, of point defects, or equivalently, the average inter-defect distance, L_D. The induced damage results in a distribution of vacancy point-like defects. While the pristine parts of the graphene layer give rise to the G-peak, the D-peak is localised within few nanometers from a disruption of the crystal lattice symmetry, i.e. point defects in this case. In Lucchese's model, two distinct spatial regions are used to describe a defect. A 'structurally disordered region' (type S) of radius r_S is created from the impact of the ion, whereas an 'activated region' (type A) of radius r_A describes the pristine area around the defect, giving rise to the D-peak (Fig. 3.1(a)). In practice, the annulus between r_A and r_S is eventually responsible for the D-peak intensity. The radius r_A can be also be written as $r_S + \ell$. By following this model, a phenomenological expression linking $I(\mathrm{D})/I(\mathrm{G})$ to L_D, can be derived as[86]

$$\begin{aligned}\frac{I(D)}{I(G)} =& C_A f_A(L_D) + C_S f_S(L_D) \\ =& C_A \frac{r_A^2 - r_S^2}{r_A^2 - 2r_S^2}[e^{-\pi r_S^2/L_D^2} - e^{-\pi(r_A^2 - r_S^2)/L_D^2}] + C_S(1 - e^{-\pi r_S^2/L_D^2}),\end{aligned} \tag{3.1}$$

where $f_A(L_D)$ and $f_S(L_D)$ are the fractions of the areas of type A and S respectivily, in the graphene lattice. The evolution of the two areas of type A and S is depicted in Fig. 3.1(b) for different levels of disorder, corresponding to different L_D; C_A and C_S are the factors describing, respectively, the contribution of the areas of type A and S to the D-peak intensity. In particular, C_A is the ratio of the relative Raman cross-sections of the D- and the

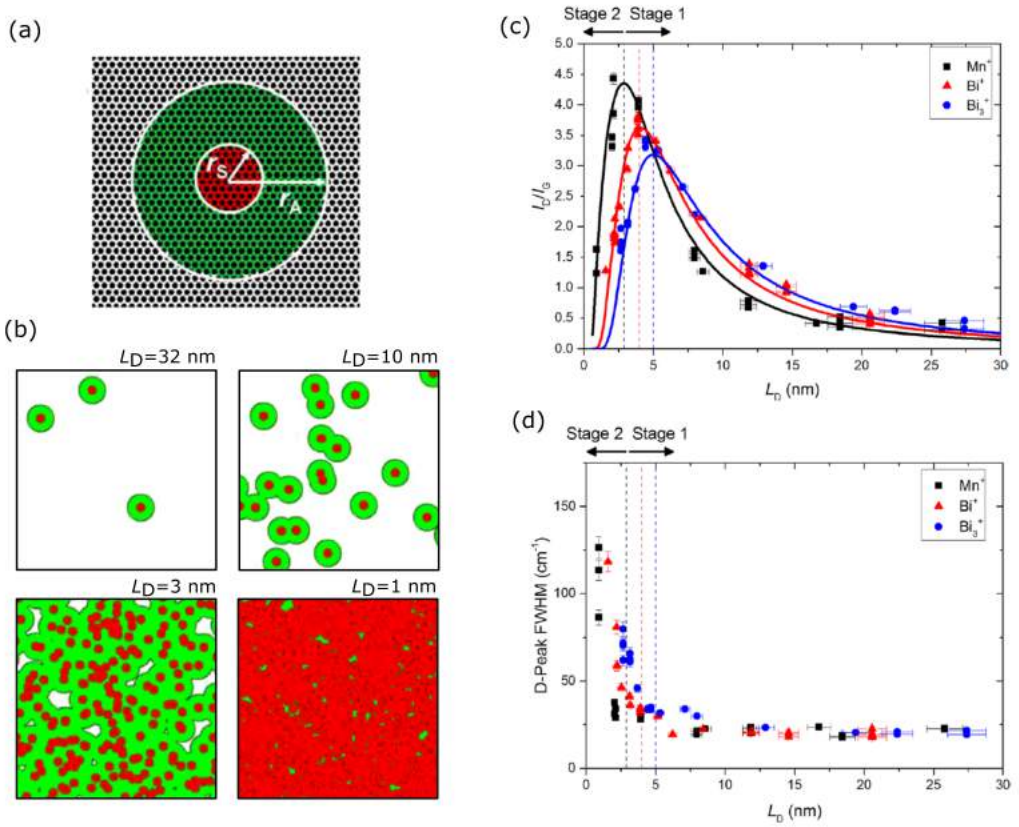

Figure 3.1: (a) Visual description of 'activated region' in green and 'structurally disordered' region in red, adapted from Ref.86. (b) Simulations of structural evolution in 45x45 nm areas within a graphene layer. These corresponds to bombardment of 10^{11} ions/cm^2 ($L_D = 32$), 10^{12} ions/cm^2 ($L_D = 10$) 10^{13} ions/cm^2, ($L_D = 3$) 10^{14} ions/cm^2, ($L_D = 1$), adapted from Ref.86. (c) Evolution of I(D)/I(G) and (d) D-peak FWHM for different defect size/ions and L_D, adapted from Ref.88.

G-peak, and was found to be excitation energy dependent[87]. As suggested in Refs.[89,90], C_S can be considered to be dependent on the defect type. For the purpose of this work the contribution of the latter factor will be considered null, as the focus is on vacancy-type defect, therefore the S regions do not contribute to either D- or G-peak intensity.

Fig. 3.1(c) shows the experimental I(D)/I(G), measured by Pollard et al., as a function of L_D and for different ion types (adapted from Ref.88).

The experimental data are fitted using Eq.3.1; two distinct regimes can be identified. As L_D decreases, the total area of type A on the graphene layer increases (green area in Fig. 3.1(a-b)). The contribution to the D-peak increases and therefore $I(\mathrm{D})/I(\mathrm{G})$ increases until a peak is reached in correspondence of small L_D (3-5 nm). This regime is referred as stage 1 in the literature. As L_D is further decreased, the total area of type S (red area in Fig. 3.1(a-b)) outweighs the total area of type A and $I(\mathrm{D})/I(\mathrm{G})$ tends to vanish. This regime is referred as stage 2. The distinction of the two stages can be also seen in the behaviour of the D-peak full width at half maximum (FWHM), which is constant to $\simeq$20-30 cm^{-1} in stage 1 and dramatically increases up to $\simeq$100 cm^{-1} in stage 2, due to phonon spatial confinement[91] (Fig. 3.1(d)).

There are however several issues with conventional confocal Raman spectroscopy when investigating nanoscale defects. Due to the diffraction limit, confocal Raman spectroscopy provides an averaged spectrum over the probe size (typical sizes vary from several hundred nanometres to around 1 μm^2 depending on the laser wavelength and numerical aperture), whereas the electron-hole pair involved in the D-peak process is expected to recombine within a few nanometres from the defect[55,92,93]. Therefore, for typical defect densities it is not possible to spatially resolve individual defects; additionally, inferring the distribution of defects based on the analysis of a confocal Raman spectrum is challenging. Moreover, the confocal Raman spectroscopy signal strength from individual defects is extremely weak, making detection difficult in the case of a very low defect density. Confocal Raman spectroscopy also does not allow a straightforward discrimination among different types of defects when they are present together within the same sample. For example, both vacancies and grain boundaries in chemical vapour deposition (CVD) grown graphene can be regarded as defects, however they cannot be distinguished and quantified separately using confocal Raman spectroscopy. Specific defects, such as dopant atoms to modify the carrier density of graphene[94], or sp^3 hybridised bonds in oxidised[95] or fluorinated[96] graphene, can be deliberately introduced rather than being an undesired result of the graphene production process. Hence, knowledge of their

distribution is highly desirable to optimise defect engineering in graphene. The quantification of defects in liquid-phase exfoliated graphene using Raman spectroscopy is also particularly challenging[97], as the graphene flake size is comparable to the confocal probe size and the D-peak signal from the edge is therefore always probed in these measurements. Although other techniques such as electron microscopies or scanning tunnelling microscopy (STM) can be used to resolve individual lattice defects to overcome many of these obstacles, they may be destructive or restricted to conductive substrates, respectively.

In this chapter, a demonstration of the ability to resolve the near-field Raman scattering signal from a point defect in graphene using TERS is given. The analysis of the measured near-field Raman spectra enables direct and non-destructive enumeration of defects within the graphene sheet, thus greatly reducing the uncertainty in L_D when compared with its determination using confocal Raman spectroscopy (which is only able to provide an estimate of the average inter-defect distance). To further gain insight into the physics of near-field enhancement of point-like Raman scatterers, a theoretical model is also developed and further extended to generalised zero-dimensional Raman scatterers, including molecules.

3.2 Methods

Graphene samples were produced through mechanical exfoliation of highly oriented pyrolytic graphite (HOPG) on to glass coverslips. A single-layer graphene flake was identified on the substrate through a combination of AFM and confocal Raman spectroscopy. Defects were introduced by means of Bi_3^+ ion bombardment (performed by B. Brennan), with an ion energy of 25 keV, as described in detail in Refs 98, 99. These bombardment conditions result in a defect radius of $r_S = 1.9 \pm 0.1$ nm, as previously determined using STM[98]; an example STM image (acquired by A. Pollard) of a point defect in bombarded HOPG is shown in Fig 3.2(c). The ion current and the exposure time were tuned[98] to obtain a defect density of n_D=10^{10} ions/cm^2, which corresponds to an average inter-defect distance $L_D \cong$100 nm, according to

$L_D = 1/\sqrt{n_D}$.

3.3 Experimental Results

Post-bombardment, a very weak D-peak appears in the confocal Raman spectrum, revealing $I(\mathrm{D})/I(\mathrm{G})$=0.03 ± 0.01 (Fig.3.2(d)). This measurement was performed at the centre of the graphene flake, in order to rule out any contribution of the D-peak arising from the graphene edges. Based on Eq.(3.1), an $I(\mathrm{D})/I(\mathrm{G})$ value of this order is expected for such a low density of defects. However, due to the uncertainty on the estimated values of C_A, r_S, and ℓ reported in literature[86,87,98], as well as the uncertainty on the estimated $I(\mathrm{D})/I(\mathrm{G})$ value (arising from the low intensity of the D-peak measured in the Raman spectrum) a precise determination of an average inter-defect distance of this order cannot be obtained using Eq. (3.1). Here, an average inter-defect distance L_D=100±40 nm can be derived from confocal Raman spectroscopy. The large uncertainty in this value results from an application of the worst case uncertainty analysis to Eq. (3.1), where $I(\mathrm{D})/I(\mathrm{G})$=0.03±0.01, as found in this work, and $C_A = 5.0 \pm 0.9$, $r_S = 1.9 \pm 0.1$ and $\ell = 2.4 \pm 0.6$ as reported in Ref. 98, obtained by fitting Eq. (3.1) to the experimental variation of $I(\mathrm{D})/I(\mathrm{G})$ as a function of L_D.

In general, a scaling factor dependent on the Fermi level energy, E_F, should be taken into account in Eq. (3.1) whenever doping is introduced[100]. The position of the G-peak (Pos(G)), the FWHM of the G-peak (FWHM(G)), the position of the 2D-peak (Pos(2D)), and the intensity ratio between the 2D- and the G-peak, $I(\mathrm{2D})/I(\mathrm{G})$, are sensitive to doping and can subsequently be used to estimate E_F[101]. The Raman spectrum of the graphene flake here investigated shows Pos(G)≅1581 cm^{-1}, FWHM(G)≅14 cm^{-1}, Pos(2D)≅2670 cm^{-1}, and $I(\mathrm{2D})/I(\mathrm{G})$≅4.8, that are consistent with negligible doping[100] (E_F<100 meV). Therefore, the effect of doping in Eq. (3.1) can be neglected. Such doping occurs naturally upon exfoliation, due to a combination of surface adsorbates after exposure of the graphene flake to ambient conditions[102], and of charge transfer with the substrate[103]. These values do not vary significantly when defects are introduced and therefore

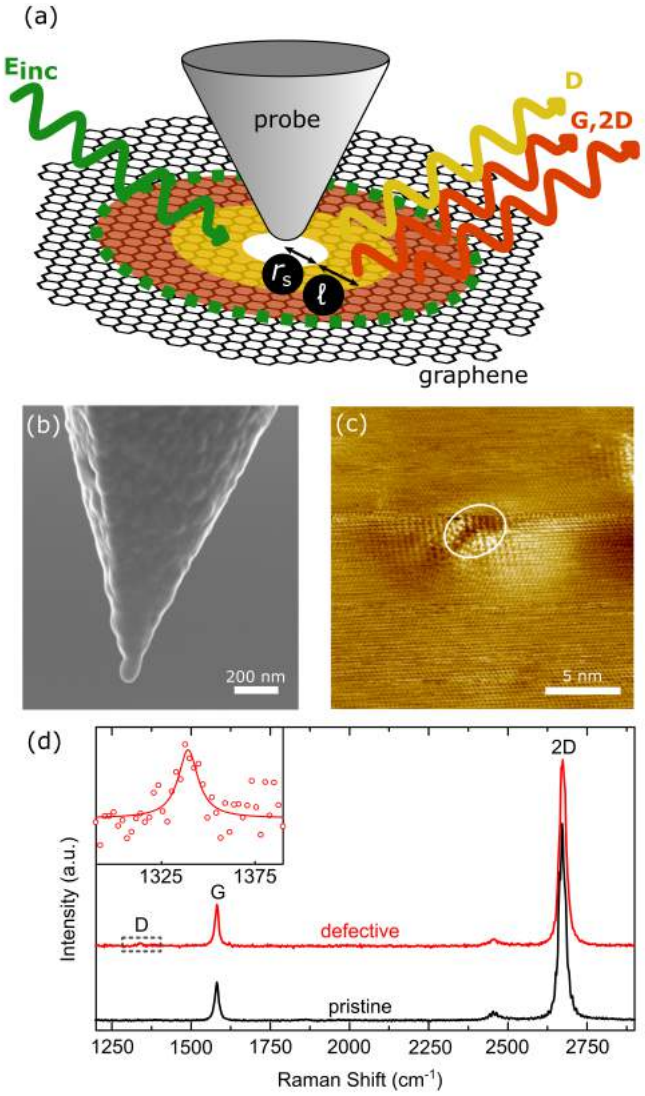

Figure 3.2: (a) Schematic diagram of TERS experiment using an Ag-coated AFM probe on a vacancy defect (white disk) in a graphene flake. The incident green light (E_{inc}) illuminates the defect and the TERS probe. The Raman scattering is enhanced from the near-field region (delimited by the green dashed line) where the defect is located. The Raman D-peak scattering occurs in the region around the defect (yellow), whereas the Raman G-peak scattering is present for all areas of the graphene flake that are illuminated (Image not to scale). (b) SEM image of an Ag-coated AFM probe used in this work. (c) STM image (acquired by A. Pollard) of a HOPG surface with a defect (white ellipse) created by bombarding the surface with Bi_3^+ ions (sample voltage 50 mV, tunnel current 1.0 nA). (d) Comparison of the confocal Raman spectrum of pristine and defective graphene. Inset shows the D-peak spectral region in the defective graphene Raman spectrum. Symbols are experimental points and the solid line is a Lorentzian fit.

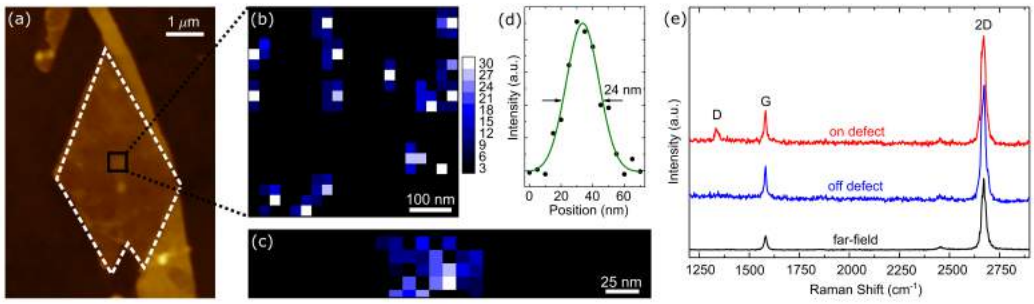

Figure 3.3: (a) AFM topography image of a single-layer graphene flake (marked by the white dashed line). (b) TERS map obtained using the Raman D-peak intensity (a.u.), showing the distribution of point defects within the flake. Pixel step-size 25 nm. (c) High resolution TERS image of a point defect obtained using the D-peak intensity. (d) Line profile of the TERS D-peak intensity across a point defect. Dots are experimental points, the solid green line is a Gaussian fit. (e) Comparison of one representative far-field, and two near-field Raman spectra. TERS spectra for when the TERS probe is located at a graphene point defect and when the probe is away from any defects are shown. Integration time per pixel in all TERS data is 5 s.

there is no evidence of induced doping.

Fig. 3.3(b) shows a TERS D-peak map (500×500 nm^2) of the defective graphene flake shown in Fig. 3.3(a), and a high-resolution map of an individual defect is shown in Fig. 3.3(c). From visual inspection of Fig. 3.3(b) and the representative Raman spectra (red and blue lines in Fig. 3.3(e)) extracted from this TERS map, it is evident that I(D) is distinctively more intense (I(D)/I(G)≅0.3) where point defects are located. For these points, the FWHM of the D-peak is ∼20 cm^{-1}, consistent with the low disorder regime[87]. No commensurate changes can be observed in the intensities or FWHM of the G- and 2D-peaks, which are uniform over the scanned area.

The ability to visualise the Raman scattering from each point defect enables a direct quantitative analysis. This is particularly important for very low defect densities, where the value of L_D becomes comparable to the confocal Raman probe size, and the associated error of L_D, when determined using Eq. (3.1), increases significantly. However, from Fig. 3.3(b), it can be observed that the inferred value of $L_D \cong 100$ nm determined from the

ion bombardment is consistent with the distribution of individual defects revealed using TERS imaging, from which $L_D \cong$130 nm is determined.

Ref.104 suggested a different model for assessment of L_D based on $I(\mathrm{D})/I(\mathrm{G})$ in carbon nanotubes, i.e. the relationship $I(\mathrm{D})/I(\mathrm{G}) \propto 0.5\mathrm{nm} \times 1/L_D$. However, as Ref.104 could not spatially resolve point defects they could not provide a quantitative comparison between the confocal $I(\mathrm{D})/I(\mathrm{G})$ and the number of defects, as has been presented here. In addition to this, the present analysis allows one to compare the different enhancement of the D- and G-peaks (as will be shown later), which was neglected in the model suggested by Ref.104.

A TERS map of a given Raman peak is always the convolution of the spatial distribution of the Raman scattering signal itself with the spatial extent of the region where the field enhancement takes place, which corresponds to the TERS spatial resolution. In the case of an effective zero-dimensional object, such as a point defect, the line-profile essentially corresponds to the spatial resolution of the TERS probe, which in this case is ∼24 nm (Fig. 3.3(d)). To resolve the shape of the ring associated to the D-peak (shown as a yellow area in Fig. 3.2(a)) the spatial resolution must be much improved (down to 1-2 nm). This resolution has been demonstrated in particular experimental conditions such as cryogenic temperature, ultra-high vacuum[64] or STM-based TERS[105], where a conductive substrate is required. However, the present TERS measurements are conducted without any environmental constraint.

In order to compare the confocal and tip-enhanced Raman spectra few relevant concepts and notations are introduced in the following. In a tip-enhanced Raman spectrum, the peak intensities represent the sum of two Raman scattering contributions arising from the near-field enhancement region and from the region illuminated by the confocal probe, i.e. the far-field. The enhancement factor (η) is defined as[106]

$$\eta = \alpha \frac{I_{NF}}{I_{FF}}, \tag{3.2}$$

where NF and FF stand for near-field and far-field respectively. I_{NF} and

I_{FF} are the peak intensities, with the ratio I_{NF}/I_{FF} usually referred to as contrast[83]. The G- and 2D-peaks are allowed Raman modes arising from the whole of the probed graphene area. The value of η for the G- and 2D-peaks can be calculated using Eq. 3.2 through consideration of A_{NF} and A_{FF}, the areas of the sample that produce the specific Raman scattering peak under investigation, such that $\alpha = A_{FF}/A_{NF}$. Therefore A_{NF} and A_{FF} are calculated for these peaks using the near-field and far-field spatial resolutions respectively, where A_{FF} is determined using a diameter of the confocal probe[83] of 225 nm, and A_{NF} is determined using the near-field spatial resolution previously calculated from Fig. 3.3(d). Contrarily, D-peak Raman scattering is localised close to defects and therefore, for a spatial resolution greater than $2r_A$, $\alpha = n_D \times A_{FF}$, that is the number of defects within the probed far-field area. Here, $\alpha \cong 4$ for $L_D = 100$ nm.

The values of the enhancement factor η and the calculated contrasts of the D-, G- and 2D-peaks are summarised in Fig. 3.4. The contrast of the D-peak is $\sim$40 times higher in comparison to the G- and 2D-peaks, mainly due to the high localisation of the D-peak around the defects and the very low number of defects probed within the far-field area.

The analysis of the enhancement factor is far from trivial as it depends on several factors[107–110], such as the probe-sample distance, the incident laser polarisation, the angle of the probe to the sample normal, the symmetry of the modes, the dimensionality of the Raman scatterer, the coherence of the Raman scattering and the plasmonic resonance profile of the probe.

In particular, one can note that the enhancement factor of the G-peak is $\sim$1.5 times lower than that of the D-peak. This is expected when the spatial resolution is less than the coherence length of the phonons, i.e. $\cong$ 30 nm for optical phonons in graphene[109]. In the fully coherent regime, the intensity of the G-peak from the near-field region should in principle vanish due to destructive interference effects[109] arising from the particular symmetry of the mode (E_{2g}), for a polarisation that is perpendicular to the sample. However, an enhancement for the G-peak is still observed here, as the angle of the probe dipole is generally randomly oriented. As the D-peak is assigned to the A_{1g} symmetry, the corresponding signals from the near-field region add

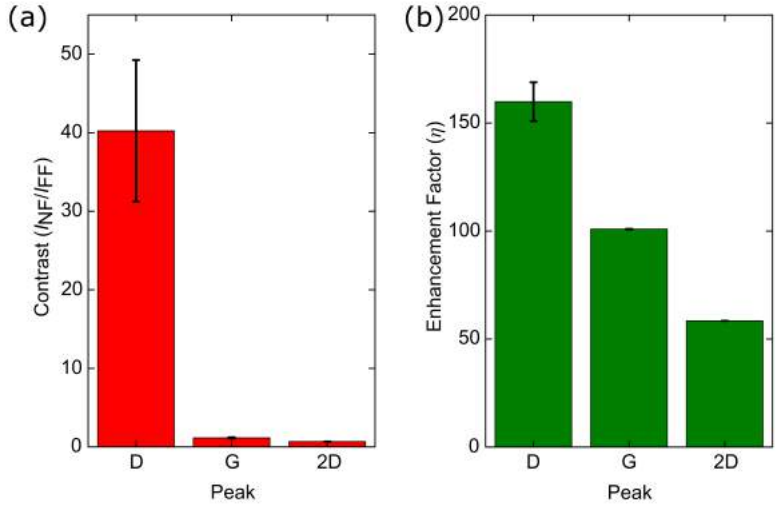

Figure 3.4: (a) Contrast and (b) enhancement factor for the main Raman scattering peaks. Error bars represent the standard error from the fitting process. The contrast for the D-peak depends on the number of defects probed within the far-field area, equal to α.

in-phase[109]. However, one should note that in this case the D-peak is heavily enhanced due to the fact that the defect acts as a zero-dimensional point source, i.e. a steeper D-peak signal increase is expected as the probe approaches the sample[109]. Although the 2D-peak shares the same A_{1g} symmetry, a much lower enhancement factor is observed for the 2D-peak, compared to both the D- and the G-peaks. This observation can be attributed to the frequency-dependent enhancement due to the plasmonic resonance profile of the Ag-coated TERS probe, leading to a different scale of enhancement for the 2D-peak, as the associated Raman shift ($\sim$2670 cm^{-1}) is much higher than that of the D- and G-peaks. This effect is particularly relevant for Ag-coated probes, as Ag exhibits much sharper resonances[111,112] when compared to Au[113], which is also frequently used for TERS measurements.

One should note that the probe position, relative to the sample and the laser focus, could affect the calculation of contrast and enhancement factor using Eq. (3.2) (as mentioned above). This effect can be separated in two contributions: the movement of the probe in the plane of the sample, affecting the tip-laser alignment, and the movement of the probe in the direction

perpendicular to the sample. In the plane of the sample, the probe is placed within the confocal probe diameter of 225 nm, corresponding to the FWHM of its Gaussian spatial intensity profile, such that TERS enhancement has a very weak dependence on any small misalignment between the probe and the laser focus. On the other hand, in the direction perpendicular to the sample, the probe position is governed by the AFM feedback control. As this is much less than the radius of curvature of the probe, the enhancement factor is not expected to be affected.

Ref. 110 reported on a theoretical study of the enhancement factors for graphene's most prominent Raman peaks, occurring in proximity to a one-dimensional scattering site. The authors predicted a symmetry-dependent enhancement of the D-peak, which was experimentally validated later in Ref. 109 via a TERS scan across a graphene edge. A similar qualitative selectivity - albeit with a different numerical value of enhancement factor - should in principle be observed for a lower dimensionality scatterer. To the best of my knowledge, the observed preferential enhancement of the D-peak at a point defect site observed in this report, constitutes the first experimental validation of the selective D-peak enhancement in zero-dimensional sources.

3.4 Model for near-field scattering

In this section a model for near-field Raman scattering of 0-D sources is presented, with the purpose of gaining insight into the underlying principles governing the resulting enhancement and spatial resolution. In the following, a description of the geometry used for the model is given, which is schematically depicted in Fig.3.5.

When the probe-sample system is excited by an incident electric field, both the probe and the sample undergo multiple scattering events. The case of interest, which gives the most significant Raman signal at the detector, is the one where: (i) the incident field is enhanced by the probe, (ii) the enhanced field excites the sample, (iii) the excited Raman signal is enhanced by the probe and then collected. The incident electric field at the probe

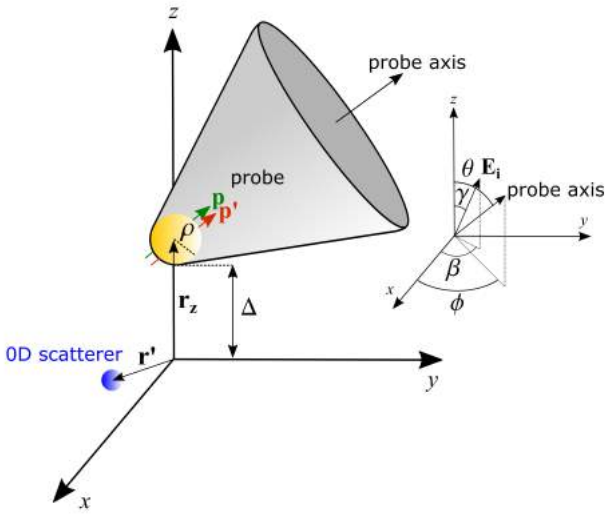

Figure 3.5: Schematics of the model, representing a near-field probe on a 0-D Raman scatterer. Δ is the distance between the probe and the plane xy, where the 0-D Raman scatterer is located. In yellow is the probe apex, described by a curvature radius ρ. r' and r_z indicate the location of the 0-D Raman scatter and the center of the probe apex, respectively. p and p' are the dipole moments at the probe apex, aligned with the probe axis, and described by the angles θ and ϕ with respect to the z and x axes, respectively. E_i is the incident field described by the angles γ and β relative to the z and x axes, respectively.

apex, located at r_z, can be written as

$$\begin{aligned} E_i(r_z,\omega) =& E_i(\sin\gamma\cos\beta\hat{\mathbf{x}} + \sin\gamma\sin\beta\hat{\mathbf{y}} + \cos\gamma\hat{\mathbf{z}}) \\ =& E_{||}(\cos\beta\hat{\mathbf{x}} + \sin\beta\hat{\mathbf{y}} + E_z\hat{\mathbf{z}}) \\ =& E_x\hat{\mathbf{x}} + E_y\hat{\mathbf{y}} + E_z\hat{\mathbf{z}}, \end{aligned} \tag{3.3}$$

where E_i is the amplitude of the electric field, $\hat{\mathbf{x}}$, $\hat{\mathbf{y}}$ and $\hat{\mathbf{z}}$ represent the unit vectors of the Cartesian coordinates system, γ is the angle between the electric field and the z-axis and β is the angle between the projection of the electric field on the xy-plane and the x-axis. The metal probe can be modelled as a metal sphere with radius ρ, whose surface is at distance Δ from a 0-D scatterer located on the xy-plane. Given an electric field of wavelength λ and frequency ω, one typically has $\lambda >> \rho$ in near-field experiments,

and therefore the incident electric field induces a simple dipole at the probe apex, as also confirmed experimentally[114]. In practice, the elongation of the probe needs to be taken in account: for highly enhancing probes the dipole is oriented along the probe axis. Within this model, the polarisability of the metal probe can be written as[108]

$$\bar{\bar{\alpha}}_{\mathbf{p}}(\omega) = 2\pi_0\rho^3\tilde{f}(\omega)\times\begin{pmatrix} \cos^2\varphi\sin^2\theta & \cos\varphi\sin\varphi\sin^2\theta & \cos\varphi\cos\theta\sin\theta \\ \cos\varphi\sin\varphi\sin^2\theta & \sin^2\varphi\sin^2\theta & \sin\varphi\cos\theta\sin\theta \\ \cos\varphi\cos\theta\sin\theta & \sin\varphi\cos\theta\sin\theta & \cos^2\theta \end{pmatrix},$$

(3.4)

where θ is the angle between the probe symmetry axis and the z-axis, φ is the angle between the projection of the probe symmetry axis on the xy-plane and the x-axis. Here a complex enhancement factor, $\tilde{f}(\omega)$ is used, dependent on material and geometry of the probe. The field generated by the dipole moment $p(r_z,\omega) = \alpha_p(\omega)E_i(r_z,\omega)$ at the probe apex generates a field propagating to the point-like scatterer, located at r'. The electric field at r' can be written as

$$E'(r',\omega) = \frac{\omega^2}{\epsilon_0 c^2}\bar{\bar{G}}(r_z,r';\omega)\cdot\bar{\bar{\alpha}}_p(\omega)\cdot E_i(r,\omega), \tag{3.5}$$

with the near-field term of the free-space Green's function

$$\bar{\bar{\mathbf{G}}}(r_z,r';\omega) = \frac{e^{i/c}}{4\frac{\omega^2}{c^2}R^3}(-\bar{\bar{I}} + \frac{3RR}{R^2}), \tag{3.6}$$

where $R = r_z - r'$, $R = |R|$, $\bar{\bar{I}}$ is the identity dyadic, c is the vacuum speed of light. A Raman dipole $d(r',\omega_S) = \bar{\bar{\alpha}}_R(\omega_S,\omega)\cdot E'(r',\omega)$ is induced in the

point-like scatterer, which is described by a Raman tensor

$$\bar{\bar{\alpha}}_{\mathbf{R}}(\omega_S,\omega)=\begin{pmatrix}\alpha_{11}&\alpha_{12}&\alpha_{13}\\ \alpha_{21}&\alpha_{22}&\alpha_{23}\\ \alpha_{31}&\alpha_{32}&\alpha_{33}\end{pmatrix}, \tag{3.7}$$

with ω_S being the frequency of the Raman signal. The electric field emitted by the Raman dipole reaching the probe apex is

$$E''(r_z,\omega_S)=\omega_S^2/(\epsilon_0c^2)\bar{\bar{G}}(r',r_z;\omega_S)\cdot\bar{\bar{R}}(\omega_s,\omega)\cdot E'(r',\omega), \tag{3.8}$$

which in turn induces a secondary dipole $p'(r_z,\omega_S)=\bar{\bar{\alpha}}_p(\omega_S)E''(r_z,\omega_S)$. Using Eqs. 3.5-3.8, the collected field intensity I assumes the form

$$I\propto|p'(r_z,\omega_S)|^2=\frac{\omega^4\omega_S^4}{\epsilon_0^4c^8}|\bar{\bar{\alpha}}_p(\omega_S)\cdot\bar{\bar{G}}(r',r_z;\omega_S)\cdot\bar{\bar{\alpha}}_R(\omega_S,\omega)\bar{\bar{G}}(r_z,r';\omega)\cdot\bar{\bar{G}}_p(\omega)\cdot E_i(r,\omega)|^2. \tag{3.9}$$

Fixing the position of the Raman scatterer at $r'=(0,0,0)$, i.e. underneath the probe apex, Eq. 3.9 can be simplified to

$$\begin{aligned}I\propto&\frac{\rho^{12}}{16(\Delta+\rho)^{12}}E_i^2|\tilde{f}(\omega)\tilde{f}(\omega_S)|^2\\&\times[\cos\gamma\cos\theta+\cos(\beta-\varphi)\sin\gamma\sin\theta^2]^2\\&\times4\alpha_{33}\cos^2\theta-\sin2\theta[(\alpha_{13}+\alpha_{31})\cos\varphi+(\alpha_{23}+\alpha_{32})\sin\varphi]\\&+\sin^2\theta[\alpha_{11}\cos^2\varphi+(\alpha_{12}+\alpha_{21})\cos\varphi\sin\varphi+\alpha_{22}\sin^2\varphi]^2.\end{aligned} \tag{3.10}$$

From Eq. 3.10, one can note that the Raman intensity is inversely proportional to the 12^{th} power of probe-sample distance, this dependence being steeper than that found in 1-D[107] and 2-D[108] scatterers. In fact, assuming the Raman dipoles as coherent (incoherent) sources, the Raman intensity will be inversely proportional to the 10^{th} (11^{th}) power for 1-D and to the 8^{th} (10^{th}) power for 2-D systems, respectively. One can also note the presence of the factor $|\tilde{f}(\omega)\tilde{f}(\omega_S)|^2$ which, for $\tilde{f}(\omega)\cong f(\omega_S)$ (usually valid for Raman scattering), reduces to $|\tilde{f}(\omega)|^4$, usually identified as the overall enhancement

factor in near-field Raman experiments. However, if the Raman modes of interest have a rather large spectral separation, the wavelength dependence of the plasmons activated at the probe apex may start to play a non-negligible role on the different enhancement experienced by each mode. Additionally, the analytical formula shown here allows one to highlight the importance of taking into account both the probe dipole orientation and the Raman tensors in the interpretation of the experimental overall enhancement factors, which may vary significantly depending on these properties.

3.4.1 Point defects in graphene

In this section the model is applied to point defects in graphene. Indeed, as pointed out in section 3.1, the D-peak can be spatially localized in a nanometer-sized area around a vacancy point-like defect, which *defacto* acts as a point Raman source for the typical spatial resolution of near-field spectroscopy ($\cong$ 20 nm). In Fig.3.6 the spatial Raman maps arising from the D-peak of a point defect in graphene is shown, computed using Eq. 3.9, for different orientations of the incident field and of the probe. The azimuthal angles $\varphi = \beta = 0°$ and the electric field angle $\gamma = 30°$, whilst moving the angle of the probe, θ, was moved in the xz plane. The intensity is calculated by varying the position of the point defect in the xy plane, i.e. r'. In the computation, the Raman tensor for the A_{1g} symmetry associated to the D-peak was used:

$$\bar{\bar{\alpha}}_D(\omega_S, \omega) = \alpha_D \begin{pmatrix} 1 & 0 & 0 \\ 0 & 1 & 0 \\ 0 & 0 & 0 \end{pmatrix}, \tag{3.11}$$

where α_D is a constant, and x, y, and z were fixed as the principal axes of the crystal. For the curvature radius of the probe apex and for the probe-scatterer distance typical experimental geometry parameters were used, i.e. ρ=20 nm and Δ=1 nm, respectively.

As shown in Fig. 3.6 , when the probe is perpendicular to the sample (θ=0°), the TERS intensity pattern resembles a circular ring. For a slight

tilting angle, which is inevitably present in experimental conditions[114], an asymmetry starts developing in the TERS pattern which becomes a single (and slightly asymmetric) peak for the probe approaching a direction parallel to the sample. The image shape is independent on the electric field orientation (i.e. β and γ) whose only role is to affect the efficiency of the excitation of the probe dipole, and therefore the overall TERS intensity. One can also note that the patterns obtained in Fig. 3.6 reflect the probe dipole field distribution, and in particular the intensity of the in-plane electric field component incident on the sample. This is due to the structure of the A_{1g} Raman tensor adopted here, where only the diagonal components are not zero. In general, more complex shapes are expected for different Raman tensors.

In the literature it is often assumed that the resolution of a TERS image is equivalent to the extent of electric field enhancement around the probe or the probe apex radius[115]. From the patterns calculated with this model one can find that the resolution is greatly affected by the probe angle, a phenomenon neglected in literature so far, yet in experimental studies the probe is seldom oriented normal to the sample surface. For example, in the present calculation, the spatial extent of the near-field Raman signal (which, in practice, corresponds to the mapping resolution) ranges between $\sim 2(\Delta + \rho)$ for $\theta = 0°$ (ring-like map) and $\sim (\Delta + \rho)/2$ for $\theta \cong 90°$ (a single maximum), as shown in the line profiles of Fig. 3.6. Moreover, in the case of highly tilted probes (large θ), the intensity maximum occurs when the location of the probe is shifted from that of the scatterer.

Fig. 3.7 shows the dependence of the maximum TERS intensity that can be obtained in a single map on the respective orientation of the probe and electric field. The effect of the tilting angles for the electric field and the probe is first analysed, by keeping the azimuthal angles fixed ($\varphi = \beta = 0°$). In order to maximize the intensity, the condition $\gamma \cong \theta$ needs to be satisfied for high tilting angle of the electric field ($\gamma \to 90°$). When γ is lowered, the maximum intensity is achieved for θ increasingly higher than γ, and, in the limit $\gamma = 0°$, it is achieved for $\theta \cong 20°$. This trend arises as a consequence of the trade-off that needs to be reached between the condition of maximum

enhancement of the exciting light ($\gamma = \theta$) and of the Raman scattering (θ=90° for in-plane modes). Therefore, given a certain excitation incidence, the angle of the probe needs to be calibrated taking the polarisability of the sample into account. One can note that in the available literature it is often assumed that probe axis and incident electric field need to be aligned[116] and the effect introduced by the specific Raman tensor is neglected. For the sake of completeness, Fig.3.7(b) also shows the relation between the maximum TERS intensity and the azimuthal angles of the probe and the electric field (that is, their orientation with respect to one another and to the Raman tensor principal axes), which needs to satisfy the condition $\varphi = \beta$ in order for the enhancement to be maximized. The graph is plotted by keeping $\theta = \gamma = 45°$ fixed; however the shape of the plot is independent of these angles.

Knowledge of the orientation of the incident electric field at the probe axis ($E_i(r_z, \omega)$ in Eq.3.3) is required in order to compute correctly the relative Raman intensity when the probe angle is varied. However, although a focused laser beam is characterized by a dominant polarisation of the electric field, a distribution of polarisations occurs on the focal plane of a highly focused Gaussian beam[117]. As a consequence, the polarisation of $E_i(r_z, \omega)$ is dependent on the alignment of the probe apex with the focused laser beam. From the experimental point of view, the probe apex can be illuminated sideways by a linearly polarised beam (reflection mode), or through a transparent substrate by a tightly focused radially polarised beam (transmission mode). The field strength of the spurious component of E_i will depend on the numerical aperture NA of the objective lens and on the index of refraction n of the medium. To discuss the contribution of the spurious components, one can analyse the case of NA=1.4 and n=1.5, and a beam waist matching with the back aperture of the objective. For an x-polarised focused Gaussian beam, in the worst case scenario[117] (i.e. the case when the deviation from the dominant polarisation is highest, occurring in specific points within the focal plane), one has $|E_y|^2 \cong 0.003|E_x|^2$ and $|E_z|^2 \cong 0.12|E_x|^2$. When a radially polarised beam is focused, the center of the focal spot is dominated by the component E_z, whereas the intensity of the transverse component $E_{||}$ domi-

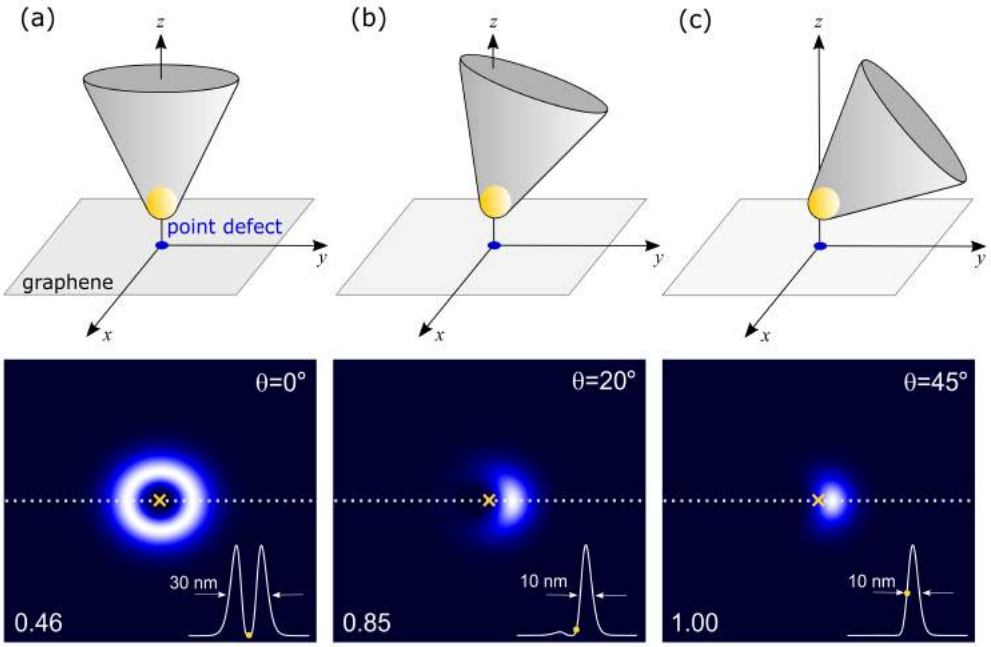

Figure 3.6: Calculated near-field intensity maps of Raman D-peak from an individual point defect in graphene, for a probe of apex radius ρ =20 nm, angles of the incident electric field γ=30° and $\beta = \varphi$. The angle θ is equal to (a) 0° (b) 20° (c) 45°. In the bottom-right sections of each panel, the relative line profile corresponding to the dotted lines are indicated. Yellow symbols indicates the point where the probe apex and the point defect are aligned along the z-axis. Relative intensities are reported in the bottom left of each figure.

nates as one moves away from the center, in a ring-like shape. In the worst case scenario, one has[117] $|E_{||}|^2 \cong 0.3|E_z|^2$. In practice, the orientation of E_i can be affected by misalignment more effectively when radial polarisation is used in comparison to linear polarisation.

3.4.2 Effect of Raman tensor on near-field Raman mapping: biomolecules

In this section, the model developed in Section 3.4 is extended to the study of the Raman tensor of a generic 0-D scatterer, demonstrating how the symmetry of the Raman tensor is reflected in the near-field map. For

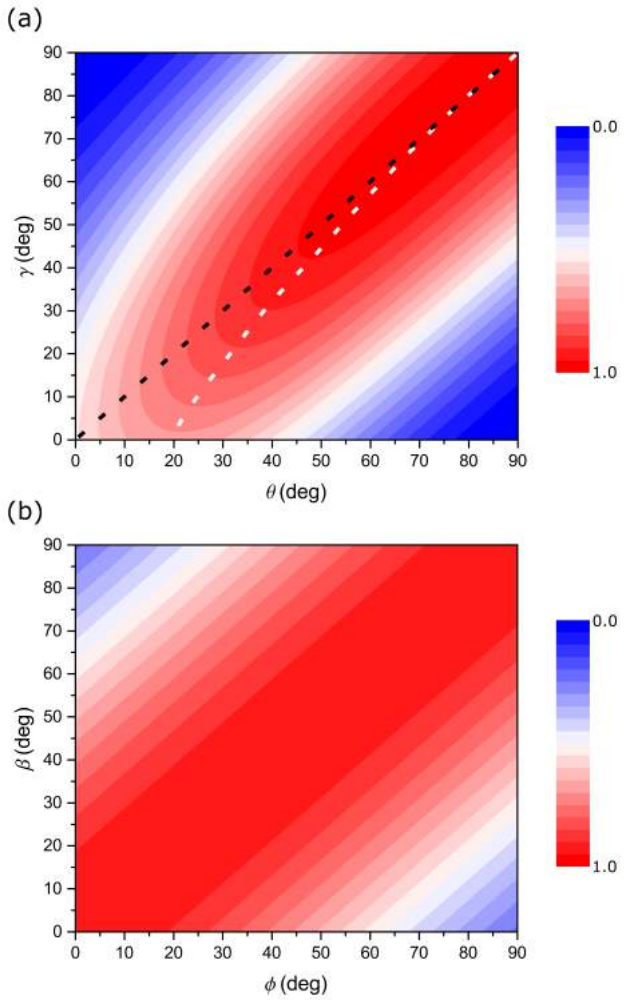

Figure 3.7: Calculated maximum intensity from near-field D-peak Raman maps of an individual point defect in graphene, as a function of the (a) inclination angles and the (b) azimuthal angles of the probe and the electric field. In (a) the optimal inclination angle of the probe, given a certain inclination angle of the electric field, is marked by the white dotted line. The black dotted line indicates the condition corresponding to $\gamma = \theta$.

the sake of simplicity, the probe is kept fixed and oriented along the z-axis, whereas the Raman tensor is varied. One can consider a general diagonalized Raman tensor of the form

$$\bar{\bar{\alpha}}^{\mathbf{0}}_{\mathbf{R}}(\omega_S, \omega) = \begin{pmatrix} \alpha_1 & 0 & 0 \\ 0 & \alpha_2 & 0 \\ 0 & 0 & \alpha_3 \end{pmatrix}, \tag{3.12}$$

with respect to a set of principal axes x', y' and z', of the particular Raman active mode, such that the Raman tensor can be expressed using a transformation matrix as

$$\bar{\bar{\alpha}}_{\mathbf{R}}(\omega_S, \omega) = \bar{\bar{\mathbf{R}}}^{T} \cdot \bar{\bar{\alpha}}^{0}_{R} \cdot \bar{\bar{\mathbf{R}}}. \tag{3.13}$$

For the present purposes only the relative magnitude of the tensor elements are relevant, therefore one can define

$$r_1 = \frac{\alpha_1}{\alpha_3} \quad r_2 = \frac{\alpha_2}{\alpha_3} \tag{3.14}$$

which totally describe the Raman tensors. A possible graphical visualization capturing $\bar{\bar{\alpha}}^{\mathbf{0}}_{\mathbf{R}}$, can be constructed by plotting the polarised Raman intensity[118]

$$I = \left| \mathbf{e} \cdot \bar{\bar{\alpha}}^{0}_{R} \cdot \mathbf{e} \right|^2, \tag{3.15}$$

where $\mathbf{e}$ is a unit vector rotating in the xyz space. In other terms, the spatial plot of I could be generated with an ideal experiment where the excitation and collection polarisers are varied in all the directions, while kept parallel to each other.

Biomolecules are of particular interest for TERS, which has been used to distinguish individual DNA and RNA bases[76,119]. DNA bases are a valuable example for the present purposes, as they have planar structures and they can lay flat on a surface. In Fig. 3.8 the four DNA bases (adenine, cytosine, guanine, thymine) are depicted, along with two other widely studied molecules, tyrosine and peptide amide III. The principal axes (blue and

red arrows), and the corresponding values of r_1 and r_2 for specific Raman modes (indicated by the blue and red numerical values, respectively), are also shown in Fig. 3.8, as reported in polarisation studies which can be found in the literature[120].

For each Raman mode of the selected molecules, both the spherical plot of Eq. 3.15, and the spatial TERS map computed using Eq. 3.9 are reported. It is possible to note a qualitative resemblance between the two spatial distributions of the plots, which allows one to gain information about the structure of the Raman tensor giving rise to a specific vibration in a molecule, via inspection of the spatial TERS map experimentally acquired on the molecule.

The determination of Raman tensors of molecules is not usually straightforward. An experimental method[120,121] to determine the tensor elements requires polarised measurements (i.e. excitation and collection polarisers are parallel) on a crystalline molecular structure first. As a second step, the depolarisation ratio, as given by cross-polarised measurements on randomly oriented molecules[122], needs to be calculated. The combination of these measurements makes both the determination of the principal axes of the molecule as well as its elements possible, however multiple measurements on two different samples are required. On the theoretical side, ab initio molecular orbital calculations can also be employed. In contrast, here the symmetry of the Raman tensor can be qualitatively inferred by acquiring the near-field intensity map of its related molecular vibration.

3.4.3 Enhancement of Raman scattering and fluorescence - a comparison

The TERS patterns presented in Sec.3.4.1 and 3.4.2 share qualitative analogies with the near-field fluorescence images of molecules and quantum dots, although the physical mechanism involved in these two optical processes is intrinsically different. Fluorescence imaging has been reported in the literature using near-field techniques such as near-field scanning optical microscopy (NSOM)[123–126] and tip-enhanced fluorescence[127].

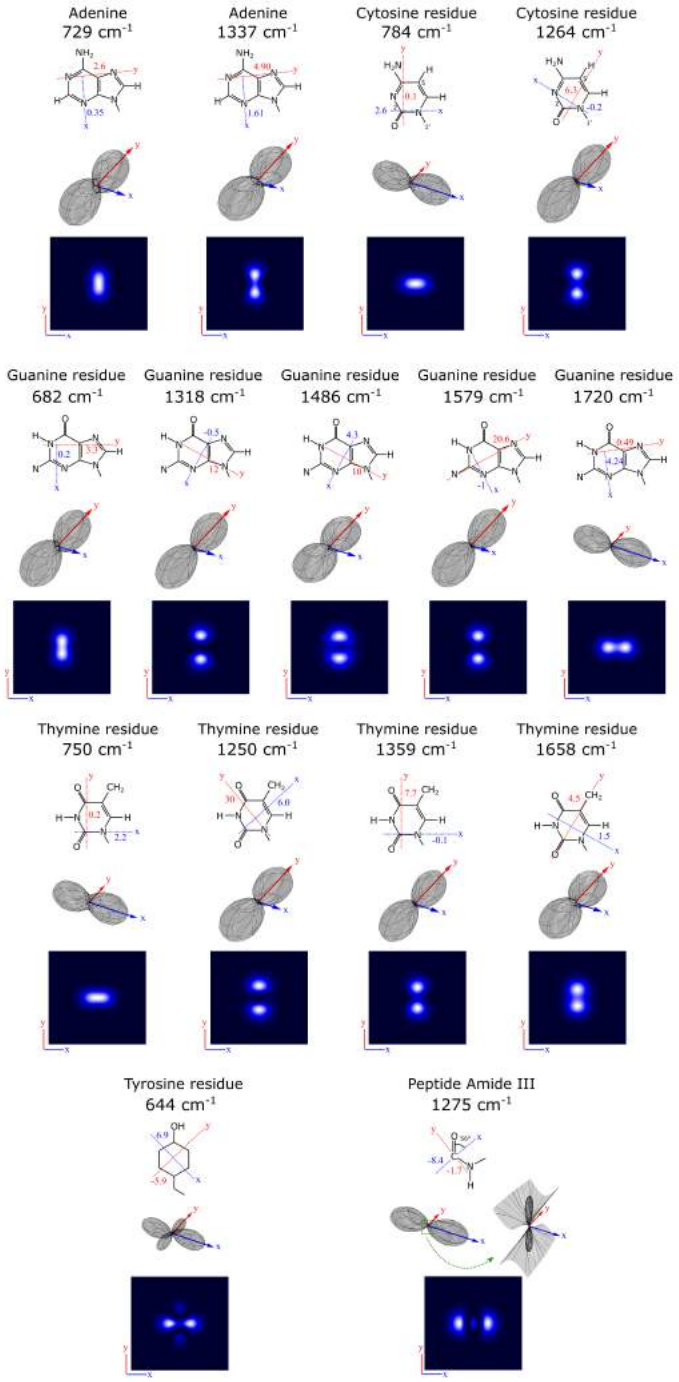

Figure 3.8: Near-field Raman maps of different bands in biomolecules (Adenine, Cytosine, Guanine, Thymine, Tyrosine and peptide Amide III) and the corresponding 3D representation of the Raman tensor. Principal axes x and y and the corresponding tensor elements, as reported in Ref. 120, are indicated in blue and red respectively.

NSOM utilizes a sub-wavelength aperture at the end of a fiber guiding the exciting light, whose polarisation determines the fluorescence intensity pattern. In tip-enhanced fluorescence microscopy, the intensity patterns are determined by the near-field generated by a sharp probe which is, to a good approximation, a dipolar field[114]. As a consequence, the intensity patterns in tip-enhanced fluorescence are less dependent on the spatial envelope of the incident field, as long as there is a sufficient z-component of polarisation in the incident field to induce a strong field enhancement. One should also note that metal probes, when placed in close proximity to a molecule (at a distance of few nanometers), can decrease the molecular quantum yield, resulting in a quenching of fluorescence[128,129] and quantitatively affecting the tip-enhanced fluorescence patterns.

In addition, a fluorescent molecule is described well by a single dipole, which can be described by a uniaxial tensor, whereas the case of Raman scattering is qualitatively more complex. The symmetry of the Raman tensor was demonstrated to have significant impact on the TERS intensity pattern. The differences between the intensity patterns of molecules with different Raman tensors are distinctive, and this can be potentially used to distinguish different molecules with different types of Raman tensors, or even different Raman modes within the same molecule.

3.5 Conclusion

In conclusion, the near-field Raman scattering arising from individual point defects in graphene was investigated. It was demonstrated for the first time that, by overcoming the diffraction limit of confocal Raman spectroscopy, tip-enhanced Raman spectroscopy enables detection of highly localised defects in graphene via their D-peak, with a resolution of ≈24 nm. A near-field Raman map was shown to allow a direct assessment of the amount and distribution of point defects within the probed graphene area, thus overcoming the large uncertainty in the average inter-defect distance when determined using confocal Raman spectroscopy. The analysis of contrast and enhancement factors evaluated in proximity to a point defect has highlighted

a selective, symmetry-dependent enhancement of the D-peak intensity at a zero-dimensional site.

A comprehensive analytical model was developed to calculate the intensity patterns in tip-enhanced Raman scattering experiments of zero-dimensional sources, such as localized Raman modes within a crystal, molecules, nanoparticles etc. The model was first applied to the study of the Raman D-peak originated from point defects in graphene. The optimal angle of the probe (maximizing the enhancement) was found to be dependent not only on the excitation incidence, as commonly accepted, but also on the Raman polarisability. The TERS patterns were also found to be sensitive to the probe orientation, thus determining the spatial resolution. The model was then applied to the study of representative biological molecules with a fixed, but arbitrary, orientation and for a range of Raman tensor symmetries. The results can be useful to determine the orientation of single molecules and differentiate molecules with diverse Raman tensors, or Raman modes with different Raman tensors from the same molecule.

4

Effect of disorder on the Raman scattering of single-layer MoS_2

4.1 Introduction

In this chapter, I will discuss the determination of the effects of defects, induced by ion-bombardment, on the Raman spectrum of single-layer molybdenum disulphide (1L-MoS_2). The evolution of both the line-widths and frequency shifts of the first-order Raman bands with the density of defects is explained with a phonon confinement model, with the aid of phonon dispersion curves computed by N. Bonini using density functional theory. Several defect-induced Raman scattering peaks arising from zone-edge phonon modes are identified. Among these, the most prominent is the LA(M)-peak at $\sim$227 cm^{-1}; its intensity, relative to the one of first-order Raman bands, is found to be proportional to the density of defects. These results provide a practical route to quantify defects in 1L-MoS_2 using Raman spectroscopy and

highlight an analogy between the LA(M)-peak in MoS_2 and the D-peak in graphene. Furthermore, multiwavelength Raman spectroscopy allows deeper understanding of both the LA-peak and the second-order Raman spectrum dominated by the 2LA band, shedding light on double-resonance Raman scattering processes occurring in 1L-MoS_2.

4.2 Methods

Using micromechanical cleavage,[1] natural bulk MoS_2 was exfoliated and deposited on Si substrates covered with 300 nm SiO_2. Photoluminescence[12] and Raman spectroscopy[43] were used to unambiguously identify 1L-MoS_2 flakes. The 1L-MoS_2 flakes were bombarded with Mn^+, each with a different ion dose, in an ultrahigh vacuum (UHV) time-of-flight secondary ion mass spectrometry (TOF-SIMS IV) instrument (ION-TOF GmbH, Muenster, Germany), equipped with a liquid metal ion gun at an angle of 45° to the surface normal and using an ion beam kinetic energy of 25 keV (ion dosing was performed by B. Brennan). Each 1L-MoS_2 flake was on a different Si substrate and was dosed during different experiments, in order to verify the reproducibility of the results. The ion beam current was measured using a Faraday cup. The uncertainty in the current measurement is ≈3% and is reflected as the uncertainty in the inter-defect distance.

Raman spectra (532 nm excitation wavelength) were collected at room temperature, in ambient conditions, on both the pristine and bombarded flakes, using a confocal system (LabRAM HR800, Horiba Jobin Yvon) in backscattering geometry, equipped with a 100× objective (numerical aperture NA=0.9) and a 600 lines/mm grating. The spectral resolution is ∼2 cm^{-1}, as derived from the line-width of the Rayleigh peak, with an uncertainty in the Raman shift position of ±1 cm^{-1} due to instrumentation. The multi-wavelength Raman measurements were carried out, in collaboration with the research group of M. Pimenta, on both a DILOR XY and a Horiba T64000 triple-monochromator spectrometers by using different laser sources (Ar/Kr, dye laser with DCM special and rhodamine 6G, and He-Cd laser) covering a wide excitation energy range from 1.85 to 2.81 eV. The laser power

was kept below 100 μW to avoid heating effects and thermal damage. The Si Raman band at 520 cm^{-1} was used as a reference for the calibration of the Raman shift.

The phonon frequencies of 1L-MoS_2 were computed by N. Bonini using density functional theory (DFT) and density-functional perturbation theory as implemented in the QUANTUM-ESPRESSO distribution,[130] within the Local Density Approximation,[131] using norm-conserving pseudopotentials. A plane-wave expansion up to a 90 Ry cut-off was used and the Brillouin zone was sampled with a $12 \times 12 \times 1$ Monkhorst-Pack mesh. The single-layer MoS_2 was modelled using a supercell approach and an interlayer spacing of 1.0 nm. The dynamical matrices were calculated on an $8 \times 8 \times 1$ uniform mesh and Fourier interpolation was used to compute the phonon dispersion on finer grids.

Resonant Raman calculations were performed by M. Pimenta's team using phonon dispersions sampled on a 400 x 400 x 1 grid for 1L-MoS_2 and a 200 x 200 x 50 grid for bulk. Since the absolute Raman shifts are prone to slight (1%) over/under-estimates due to limitations of DFT, the calculated phonon frequencies were shifted by within 1% to allow better comparison with the respective experimental dispersions. This shift leaves the calculated dispersion in the Raman shift with laser energy (which reflects the influence of the phonon and electron band structures on the double resonance Raman process) unchanged.

4.3 Results and Discussion

Figure 4.1 shows the development of representative Raman spectra of 1L-MoS_2 flakes, excited at 532 nm excitation wavelength, and bombarded with Mn^+, for an increasing density of defects. In order to induce a controllable level of surface damage, the ion beam was rastered over the 1L-MoS_2 surface. The density of ions impinging on the surface (σ) is calculated as $\sigma = It/Ae$, where I is the ion current, t the exposure time to the ion beam, A the rastered area, and e the elementary charge. By varying t it is possible to tune the defect density between 10^{12} and 10^{14} ions/cm^2. These correspond to an

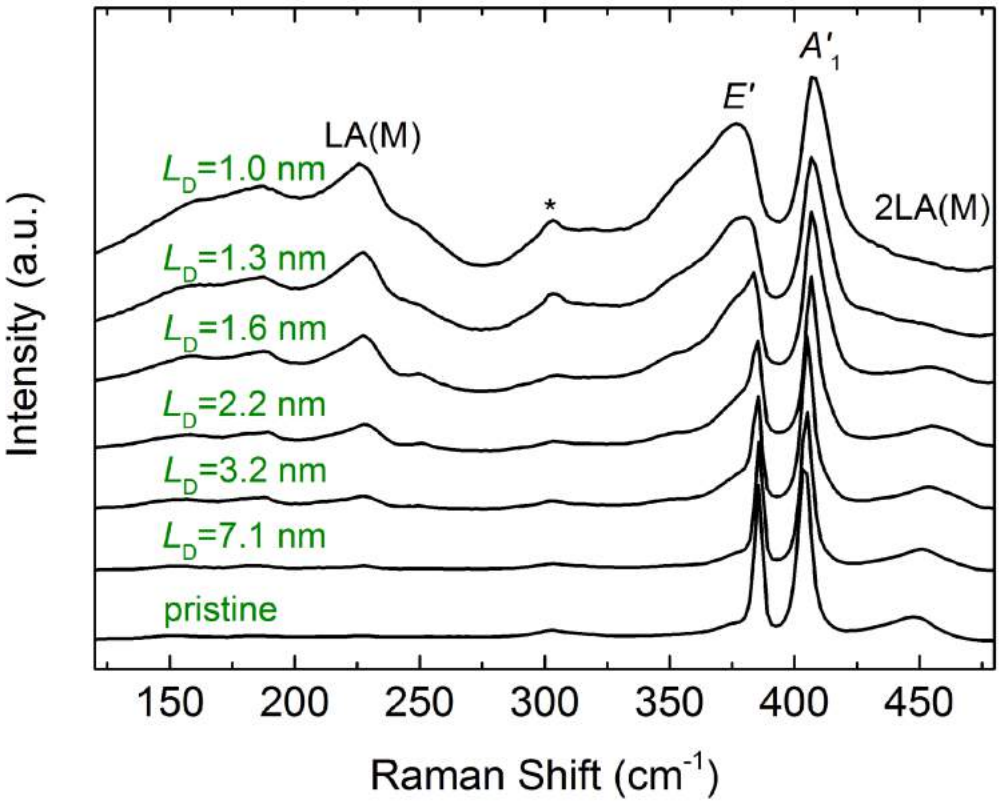

Figure 4.1: Raman spectra of 1L-MoS_2 flakes with varying inter-defect distances L_D. The asterisk refers to the 2TA(X) Raman peak of the Si substrate. The spectra have been normalized to the intensity of the A_1'-peak, as seen from the relative increase of 2TA(X) with decreasing L_D.

average inter-defect distance (L_D) ranging from 10 nm to 1 nm ($L_D = 1/\sqrt{\sigma}$). The bottom Raman spectrum of Figure 4.1 is for a pristine flake and is shown for comparison. Notably, as observed in Figure 4.1, the Raman spectrum gradually evolves as a function of L_D. This evolution can be summarized in two main points: (i) the first-order Raman bands show changes in both their widths and positions, and (ii) new Raman scattering peaks arise in the spectral region $\sim 140 - 420$ cm^{-1}.

Focusing on the two main first-order Raman bands (Figure 4.3), as L_D decreases the peak position of E', Pos(E'), downshifts while that of A_1', Pos(A_1'), upshifts, whereas the full width at half maxima, Γ, of both bands, $\Gamma(E')$ and $\Gamma(A_1')$, increase upon decreasing L_D. In order to exclude any possi-

ble contribution of temperature-induced broadening and shifts of the Raman scattering peaks, the Raman spectra were also measured as a function of laser power, confirming that no significant variation is found in the Raman spectra for a laser power range 1μW-1 mW, as evidenced in Fig. 4.2. It is worth noting that ion-induced defects in 2-D materials are usually associated with doping[17] and strain,[132] which can affect the vibrational modes. Indeed, it has been previously observed that Pos(A_1') and $\Gamma(A_1')$ are sensitive to doping, whereas E' remains unaffected.[133] However, the upshift of Pos(A_1') should be accompanied by a decrease of $\Gamma(A_1')$,[133] which is inconsistent with the present observation, allowing one to rule out the doping effect as the main mechanism involved. One could also associate the shifts in peak positions with an induced strain localized around defects. It has indeed been reported that both Pos(E') and Pos(A'$_1$) decrease (increase) with tensile (compressive) in-plane strain,[134,135] which is once again contrary to the present experimental observations. However, although doping and strain will have an effect on the Raman spectra, the observed disorder-related evolution of the first-order peaks can instead be explained using a "phonon confinement model", which has been successfully applied to explain the Raman scattering from several ion-bombarded crystals, for example, graphene,[91] graphite[136] and GaAs,[137] as well as to estimate the domain size of microcrystalline silicon[138,139] and the width of silicon nanowires.[140]

For a crystalline material, the vibrational normal modes have an infinite spatial correlation. Therefore, Raman active phonons can be described as plane-waves with finite wave vector $q \cong 0$ (known as the Raman fundamental selection rule). The corresponding Raman bands have Lorentzian line-shapes centered at frequency ω of the zone-center of the Brillouin zone, with a full width at half maximum, Γ_0, which is inversely proportional to the phonon lifetime. When defects are introduced, these perturb the spatial translational invariance of the system; as a consequence, the phonon correlation length, L_C, becomes finite, causing the breakdown of the fundamental selection rule.[138] The relaxation of the selection rule determined by the presence of disorder can be taken into account by considering an "effective" circular region, with diameter equal to L_C, within which the phonons

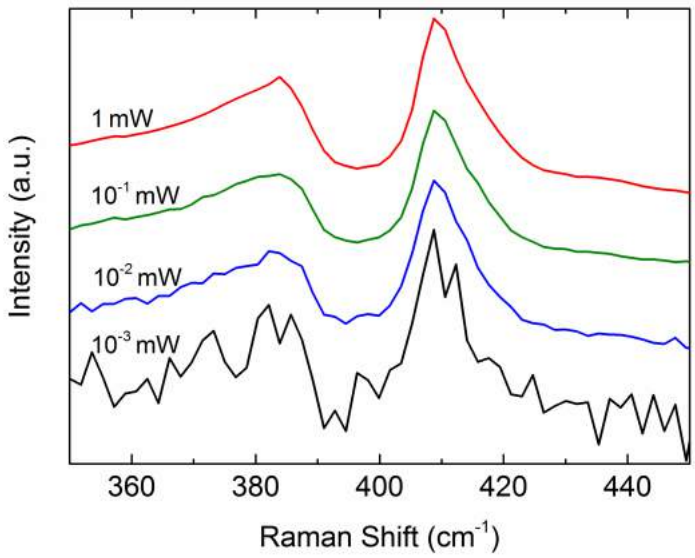

Figure 4.2: Raman spectra of defective 1L-MoS_2 (L_D=1.6nm) excited with 532 nm laser, at different laser power.

are confined, leading to a Gaussian attenuation factor of exp(-2r^2/L$_C^2$), where **r** is the spatial coordinate. In the reciprocal lattice space, this corresponds to a phonon wave-packet of exp(-q^{2}L$_C^2$/4). As a consequence, the intensity I of a Raman band can be generalized as

$$I(\omega) = \int_{BZ} \frac{e^{(-\frac{\mathbf{q}^2 L_C^2}{4})}}{[\omega - \omega(\mathbf{q})]^2 + \frac{\Gamma_0^2}{2}} d^2\mathbf{q} \tag{4.1}$$

where $\omega(q)$ is the phonon dispersion and the integral is extended over the Brillouin zone (BZ). For pristine materials, L_C tends to infinity and Eq. (4.1) reduces to a single Lorentzian centered at $\omega(0)$.

In this work, the line-shapes of the first-order peaks are modeled using Eq. (4.1), where Γ_0 is taken as the experimental width of each Raman scattering peak, as found in the pristine flakes. The phonon dispersion ω(q) of 1L-MoS_2 was calculated using DFT (credits to N. Bonini). The region of ω(q) which is of interest for the E'- and A_1'-peaks is shown in Figure 4.3(a). At

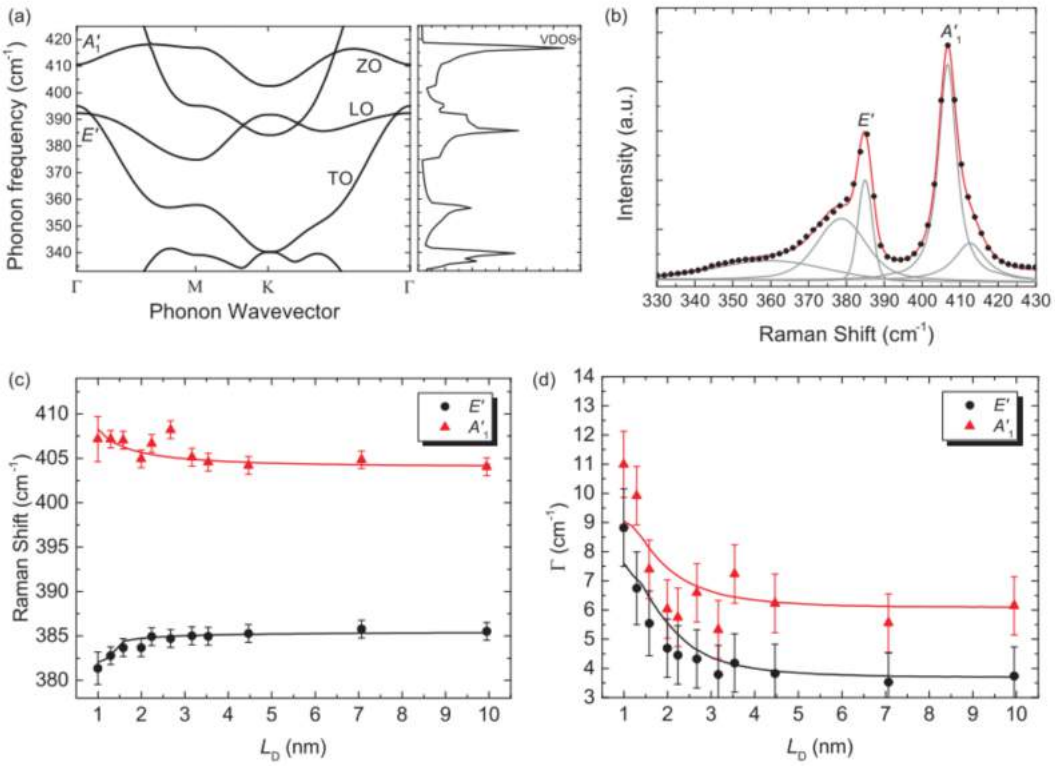

Figure 4.3: (a) Phonon dispersion and vibrational density of states (VDOS) of 1L-MoS_2 calculated by N. Bonini. (b) Close-up of the spectral region where the first-order peaks are located, for sample with $L_D = 2.2$ nm. The gray lines are the fitted Voigt peaks, and the red line is the cumulative spectrum from the Voigt fitting process. Symbols represent the experimental spectrum. (c) Position and (d) Γ of E' and A_1' as a function of L_D. Symbols refer to experimental data, continuous lines refer to the phonon confinement model described in the main text. The error bars for the peak position and Γ represent the largest uncertainty present (the spectrometer resolution or the standard error from the fitting process).

the $\mathbf{\Gamma}$-point, the out-of-plane optical (ZO) branch gives rise to the A_1' mode. The slight polarity of MoS_2 breaks the degeneracy of the longitudinal optical (LO) and transverse optical (TO) branches at the zone-center. However, due to the small LO-TO splitting, only one peak, E', is detectable using Raman spectroscopy measurements.[134,141]

Fig. 4.4 presents the line-shapes of the A_1'- and E'-peaks, numerically calculated from Eq. (4.1) using the corresponding branches of the phonon dispersion curves. For the A_1'-peak, this is the dispersion of the ZO branch. Eq.(4.1) is calculated for the LO and TO branches of the dispersion curve and then the sum of the two integrals is taken for the E'-peak. It is therefore assumed that the LO and TO branches equally contribute to the line-shape of the E' peak. The calculated phonon branches giving rise to the A_1' and E_1' peaks are rigidly shifted by -6.6 cm^{-1}, -7.0 cm^{-1}, and -9.7 cm^{-1} (for the ZO, TO and LO branches, respectively), to match each $\mathbf{\Gamma}$-point value to the experimental peak frequencies measured for pristine 1L-MoS_2. In the calculation, the phonon correlation length is taken to be proportional to the inter-defect distance,[91] that is $L_C = \alpha L_D$, where α is a real, positive number.

Figures 4.3(c) and 4.3(d) show the experimental evolution of the position and line-width of the E'- and A_1'-peaks as a function of L_D, calculated using Voigt peak-fits as there are contributions from multiple peaks in this spectral range, as shown in Figure 4.3(b). The upward and downward shifts of Pos(A_1') and Pos(E') respectively, resemble the phonon dispersion of the corresponding branches: moving away from the $\mathbf{\Gamma}$-point ($\mathbf{q} \cong 0$), the upward trend for the ZO frequencies and the downward trend for the LO and TO frequencies are observed. α is an adjustable factor, as the defect scattering cross sections are expected to be quite different for in-plane (E') and out-of-plane (A_1') modes. Here, α is determined by achieving the best agreement with the experimental trends of Pos(E'), Pos(A_1'), $\Gamma(E')$ and $\Gamma(A_1')$. From Figure 4.3, the optimal values for α are found to be 0.5 ± 0.1 and 0.8 ± 0.1 for the A_1'- and E'-peaks, respectively. Therefore the phonon correlation length and the inter-defect distance are of the same order of magnitude, supporting the validity of the proposed model. Note that these results are consistent with experiments on ion-bombarded graphene that show a proportionality between

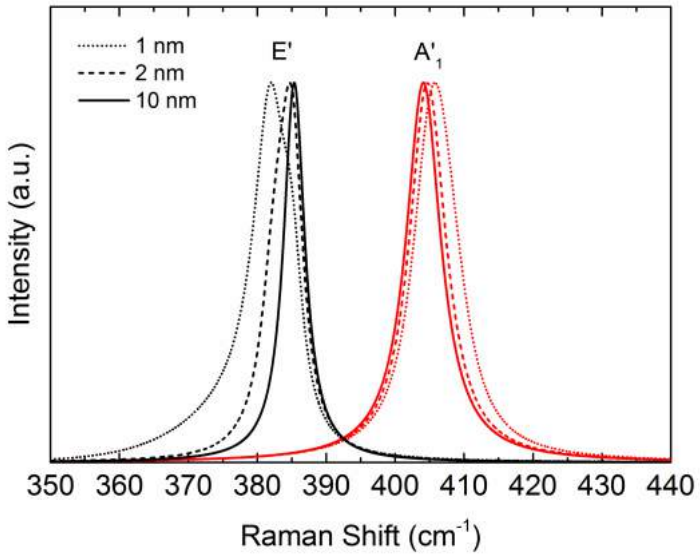

Figure 4.4: Line-shapes of the E'- and A_1'-peaks, calculated using Eq. (4.1) for different inter-defect distances L_D.

L_C and L_D, with different values of α associated to different modes.[91]

Other than the effects of phonon confinement on the two first-order 1L-MoS_2 Raman peaks, the Raman spectra of the Mn^+ bombarded samples are also characterized by the presence of defect-activated peaks. The peak positions and relative assignments, based on the correlation with peaks in the theoretical phonon dispersion (Figures 4.3(a) and 4.6(a)), are reported in Table 4.1. These modes involve phonons at the zone-edge of the Brillouin zone, which may be activated by the momentum contribution of a defect, allowing the Raman selection rule to be satisfied. Similar peaks have been previously reported in other transition metal dichalcogenides under electronic resonance condition, and ascribed to disorder-induced modes originated at the zone-edge.[143] Some of these modes, while still clearly distinguishable, overlap with the E'- and A_1' peaks, affecting the uncertainty in the fitting process. For peaks in close proximity to the first-order peaks, the defect-induced peak at $\sim$357 cm^{-1} can be assigned to the TO branch at the **M**-point, whilst at the high frequency side of the A_1' peak it is possible to distinguish

Table 4.1: Disorder-activated Raman band position and respective assignment.

Band (cm^{-1})	Assignment
154.5 ± 2.4	TA(M)
180.6 ± 1.9	ZA(M)
187.9 ± 0.8	TA(K)
215.2 ± 2.0	-
227.6 ± 0.7	LA(M)[a]
250.4 ± 1.5	-
357.7 ± 2.8	TO(M)
377.0 ± 1.1	LO(M)
411.9 ± 1.2	ZO(M)

[a]Assignment from Ref.142.

a peak centered at ∼411 cm^{-1} that is assigned to ZO(M).

Of particular interest is the peak at ∼377 cm^{-1}, which overlaps with the E' peak until it becomes barely distinguishable for high levels of disorder. Indeed, the ∼377 cm^{-1} was previously identified not as a distinct peak, but as a broadening of the E'-peak.[144] This is not the case, as clearly evidenced from the comparison between the spectra with different levels of disorder (Figure 4.1). The distinctive identity of the ∼377 cm^{-1} peak is further confirmed by its presence in pristine 1L-MoS_2, where it manifests itself as a weak shoulder located at the low-frequency side of the E'-peak. The existence of a similar shoulder has been previously reported for bulk MoS_2, and it has been assigned to Raman-inactive TO phonons with E^2_{1u} symmetry,[44,145] arising from an atomic displacement pattern similar to that of E^1_{2g}. This assignment is questionable, as reflectivity measurements show this peak at the higher frequency side of the E'-peak.[146] Moreover, the distinction between the E^1_{2g} and the E^2_{1u} modes is not present in 1L-MoS_2,[147] where a single E'-peak should be observed. Therefore, the origin of the low frequency shoulder cannot be attributed to ${E_{1u}}^2$. This study enables the ∼377 cm^{-1} feature to be identified as a disorder-induced peak, suggesting that it is a mode originated at the edge of the Brillouin zone (LO(M)).

Analysing the low-frequency region of the Raman spectrum (150-280 cm^{-1}) of Mn^+ bombarded 1L-MoS_2 (see Figure 4.1), the appearance of new

bands is observed. Among these, the most intense peak is located at ∼227 cm^{-1}. It has previously been shown that exposure to ambient conditions can cause partial oxidation of MoS_2, therefore leading to the presence of molybdenum oxides, with MoO_3 displaying Raman bands[148] in the spectral region 120-1110 cm^{-1}. The most prominent peak of MoO_3 is located at ∼820 cm^{-1} and is attributed to a symmetric stretch of the oxygen atoms in the O-Mo-O bond,[148] whilst a very weak band is also present at ∼227 cm^{-1}. Therefore, one possible assignment of the ∼227 cm^{-1} peak in 1L-MoS_2 could be an increased level of partial oxidation on the MoS_2 samples, as vacancy sites are expected to interact with molecular oxygen, thus promoting the formation of Mo-O bonds. However, if this were the case, the onset of the MoO_3 band at ∼227 cm^{-1} should be accompanied by a distinct appearance of a much more intense peak at ∼820 cm^{-1}. In the Raman spectra of Mn^+ bombarded MoS_2, a peak is observed at ∼820 cm^{-1} but its intensity does not increase as a function of disorder, indicating that it corresponds to a higher order MoS_2 peak[149,150] (see Fig.4.5).

A prominent peak at ∼227 cm^{-1} has also previously been reported in the literature for deposited MoS_2 films[152] and MoS_2 nanoparticles.[142,153] Studying MoS_2 nanoparticles, Frey et al.[142,153] attributed the ∼227 cm^{-1} peak to disorder-induced Raman scattering. This peak has been linked to the presence of a local maximum in the vibrational density of states (VDOS), located at the energy corresponding to the longitudinal acoustic (LA) branch at the edge of the Brillouin zone[147] (Figure 4.6(a)). The emerging peak has been assigned to LA phonons with momentum q≠0 at **M**-point, and referred in literature as LA(M),[142,153] which is the term that will also be used henceforth. However, restricting the origin of the peak to **M**-point phonons may not be completely justified, as (a) the VDOS presents a van Hove singularity between the **M**- and **K**-point, and (b) the LA branch is almost dispersionless over the entire edge of the Brillouin zone, that is, all the phonons at the zone-edge have similar energies and could potentially contribute to the ∼227 cm^{-1} peak. The second order of LA(M) is also present in the spectra at ∼454 cm^{-1} and it is denoted as 2LA(M) (Figure 4.1). The origin of this band is interesting and will also be discussed later. While the notations LA(M) and

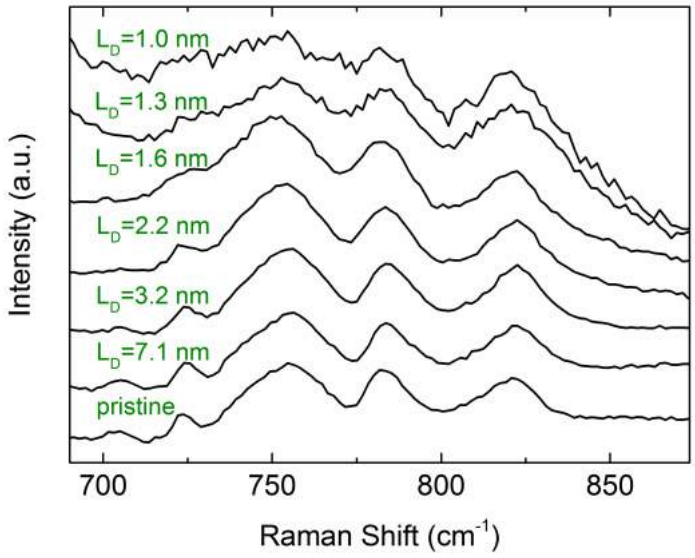

Figure 4.5: High frequency region of the Raman spectra of 1L-MoS_2 flakes with different inter-defect distances L_D. The spectra are normalized to the A_1'-peak intensity. The peaks at ∼754 cm^{-1}, ∼784 cm^{-1} and ∼820 cm^{-1} are assigned in literature to second-order peaks [149,151].

2LA(M) will be used for consistency with previous literature, in the light of the above there is no reason for restricting their origin to the **M**-point; to this end, the comprehesive multiwavelength analysis presented Section 4.5 will unveil their detailed assignement.

To further validate the strong correlation between the ∼227 cm^{-1} peak and structural defects, the evolution of the intensity (peak height) of the LA(M) peak, normalized to the E'-peak, I(LA)/I(E'), and the A_1' peak, I(LA)/I(A_1'), respectively, as a function of L_D is shown in 4.6(b). The increase of these intensity ratios is the combination of two concomitant factors occurring upon increasing disorder: (a) an increase in the absolute intensity of the ∼227 cm^{-1} peak, caused by the increase in disorder, and (b) a decrease in the intensity of the E'- and A_1'-peaks that is possibly due to the progressive ablation of the material caused by the ions bombarding the MoS_2 flakes. The latter is observed in Figure 4.1 from the increase in the intensity of the 2TA(X) Si peak, observed at ∼300 cm^{-1} and labelled with an asterisk, with

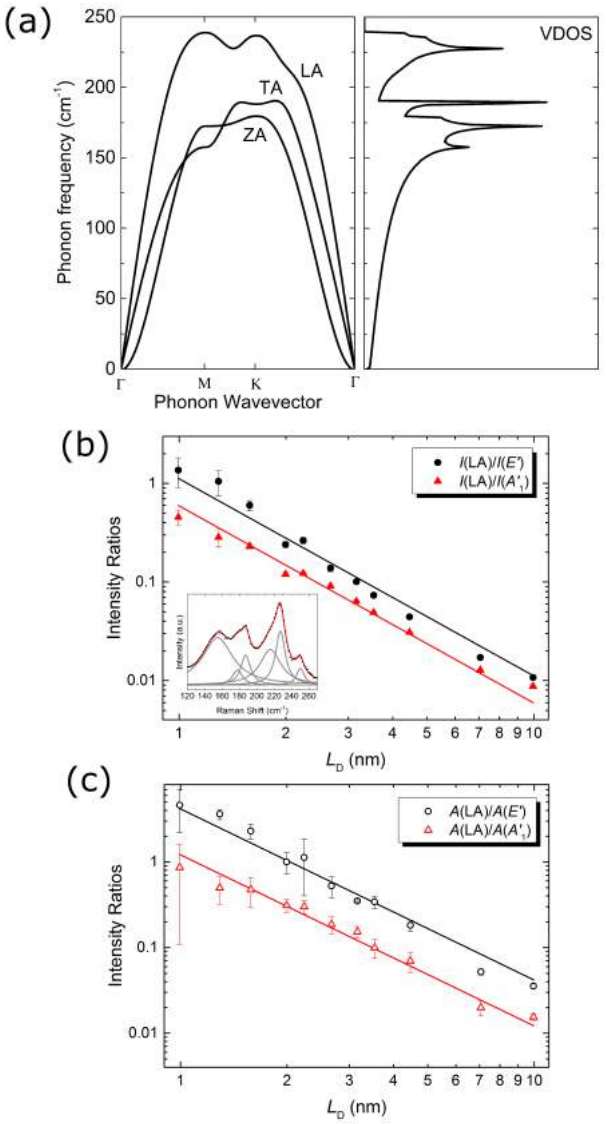

Figure 4.6: (a) Phonon dispersion and vibrational density of states of 1L-MoS_2 calculated by N. Bonini. (b) Experimental intensity ratios [$I(\mathrm{LA})/I(A_1')$ and $I(\mathrm{LA})/I(E')$] and (c) integrated area ratios [$A(\mathrm{LA})/A(A_1')$ and $A(\mathrm{LA})/A(E')$] are reported in symbols. The error bars represent the standard error from the fitting process. The solid lines are linear fits with slope equal to -2. The low frequency bands, where the LA peak is located at ≈227 cm^{-1}, are shown in the inset, along with the corresponding Lorentzian fits.

decreasing L_D (note that the spectra in Figure 4.1 are normalized to the A_1' peak). On the basis of these observations, $I(\mathrm{LA})/\mathrm{I}(E')$ and $I(\mathrm{LA})/\mathrm{I}(A_1')$ are found to be inversely proportional to L_D^2, or, equivalently, directly proportional to the total number of ions impinging on the surface ($1/L_D^2$). Fitting the data in Figure 4.6(b) using

$$I(LA)/I(X) = \frac{C(X)^2}{L_D}, \tag{4.2}$$

where X = E' or A_1', reveals that C(E') = 1.11±0.08 nm^2 and C(A_1') = 0.59 ± 0.03 nm^2. These values are expected to be dependent on the laser excitation energy used for the Raman measurements. A similar relationship is found when using the frequency-integrated peak intensities (Fig. 4.6(c)). Interestingly, these intensity ratios behave analogously to the intensity ratio of the D- and the G-peak, $I(\mathrm{D})/I(\mathrm{G})$, in graphene, which is largely used to assess the level of disorder within the lattice[86,87,91,98].

Besides the prominent mode at ≈227 cm^{-1}, one can resolve other peaks in the region 150-260 cm^{-1}, whose intensities increase with disorder. Similarly to the ∼227 cm^{-1} peak, from Figure 4.6(a), these bands appear to be linked to acoustic zone-edge phonons: the peaks located at ∼154 cm^{-1}, ∼180 cm^{-1} and ∼187 cm^{-1} are assigned to the TA(M), ZA(M) and TA(K) modes respectively.

It is interesting to observe that all disorder-induced peaks in Table 1 originate from **M**- and **K**-point phonons. The explanation for this preferential phonon activation within the Brillouin zone might be similar to the one suggested for the origin of the 2LA(**M**) band[154,155]. Indeed, it has been recently shown that this band becomes more intense than the first-order A_1'- and E'-peaks when the Raman experiment is performed with laser energies around 2 eV, which corresponds to the B exciton energy in 1L-MoS_2[155]. The mechanism proposed to account for this behaviour is a double resonance scattering process involving two LA phonons with equal and opposite momentum.

At the origin of the defect-induced peaks in 1L-MoS_2 there could be a similar double resonance mechanism, involving scattering with defects for momentum conservation. This would be similar to graphene, where the defect-

induced D-peak and the relative second-order 2D-peak are activated by a double resonance process.[156] In order to check the validity of the double resonance mechanism in 1L-MoS_2, a resonance Raman study with varying laser excitation energy is needed. A discussion of the multi-wavelength Raman spectra of both 1L- and bulk-MoS_2 is presented in Section 4.5.

4.4 Polarised Raman spectroscopy

The spectra for parallel (XX) and cross (YX) polarisation with increasing disorder are reported in Fig.4.7(a) and (b), respectively. In Fig. 4.7(c) a direct comparison of the spectra for XX and YX polarisations is also shown for a pristine sample. XX (YX) indicates the polarisation of the incident laser and the analyser's polarisation being parallel (perpendicular).

Concerning the pristine material, as expected from symmetry considerations[157,158], the A_1' peak disappears in the YX configuration whereas E' maintains its intensity unchanged. However, one can still observe a small A_1' peak for YX polarisation, which is due to polariser imperfections. In the YX configuration, one can also observe that the low- frequency E' shoulder vanishes. In the low-frequency region of the pristine spectrum, weak features are found at $\sim$ 150, $\sim$ 180, and $\sim$ 227 cm^{-1}. The $\sim$ 227 cm^{-1} peak, previously assigned to the LA branch, vanishes for YX polarisation, as seen in Fig.4.7(c). The Raman band assigned to 2LA(M) also diminishes under YX polarisation and notably its line shape undergo modifications as well; this may suggest that such feature is composed of multiple peaks (four distinct peaks will in fact be isolated within the 2LA band, using multiwavelength Raman spectroscopy, presented in the next section). There are no available reports on the symmetry of this mode from which its polarisation behaviour can be inferred; however, strikingly, a similar polarisation behaviour can be noticed for both the LA and the 2LA modes. Similarly to the pristine case, the LA peak appears to be sensitive to the polarisation in the bombarded samples; however, its intensity does not vanishes under YX polarisation but only diminishes in intensity. While these preliminary observations reveal a plethora of unexplored physical mechanisms, additional experimental studies

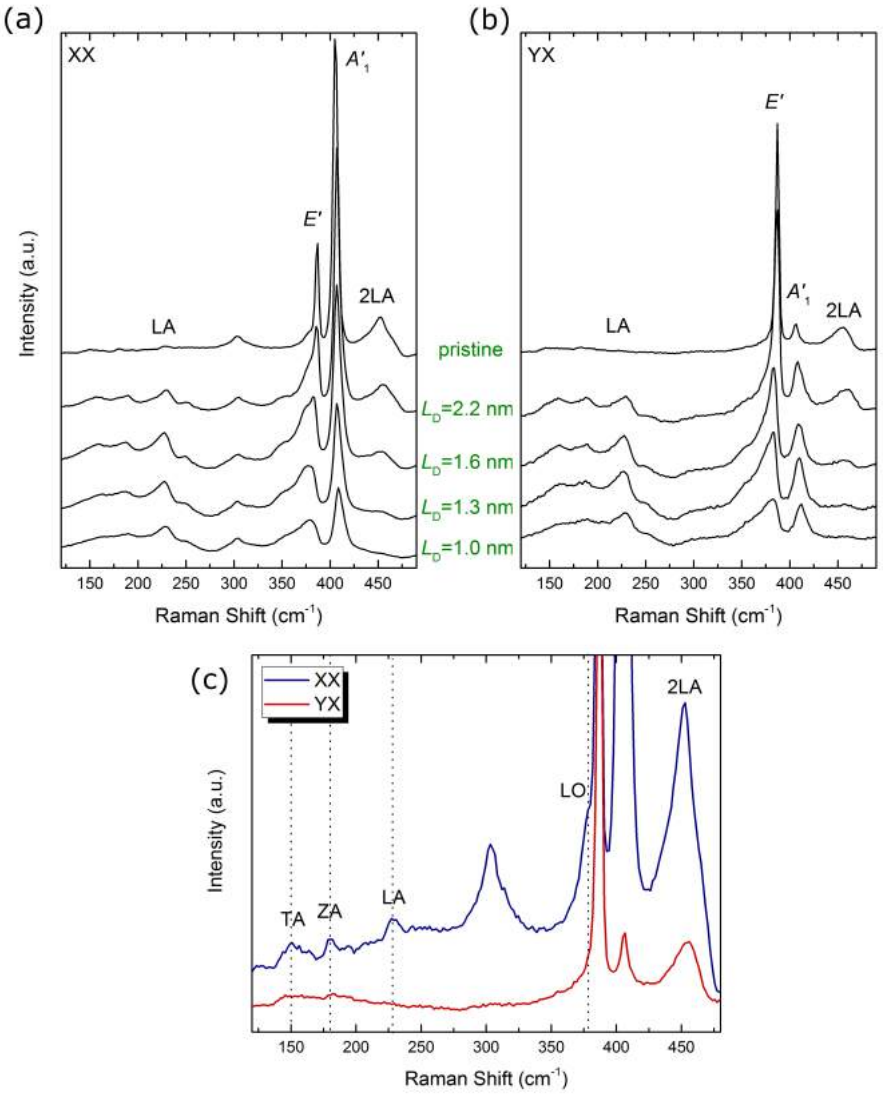

Figure 4.7: (a) Parallel and (b) cross polarised Raman spectra for pristine and defective 1L-MoS_2 on Silicon. (c) Second-order Raman bands in pristine 1L-MoS_2 in parallel (XX) and cross (YX) polarisation configurations.

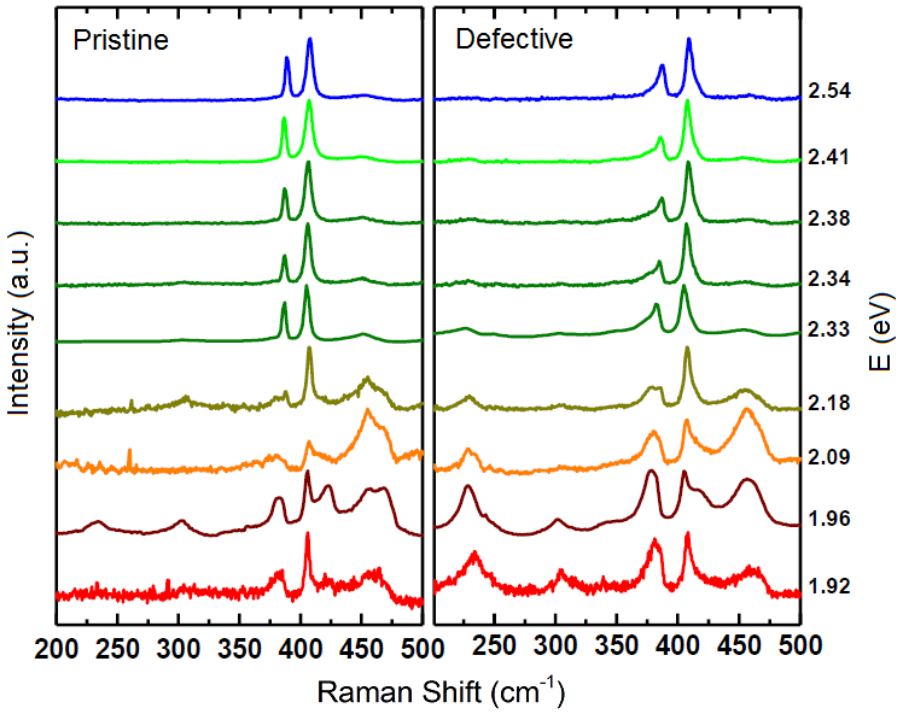

Figure 4.8: Evolution of the Raman spectra of pristine and defective 1L-MoS_2 ($L_D = 2.2$ nm) for an excitation energy in the 1.85-2.54 eV range.

and data analyses will be needed to shed light into the observed polarisation behaviour. In the next section, a multiwavelength Raman spectroscopy analysis allows gaining further insight into the origin of the 2LA band.

4.5 Resonance Raman spectroscopy

Resonance Raman spectroscopy provides important insight into the interaction of phonons with electrons or excitons. The use of multiple excitation energies is pivotal to unveiling the rich physical phenomena underlying the intervalley scattering processes in MoS_2 as well as its complex second-order Raman spectrum. Fig. 4.8 shows the evolution of the Raman spectrum for pristine (left) and defective (right) 1L-MoS_2 for multiple excitation energies E_L within the 1.85-2.54 eV range. It can clearly be seen that the intensity of the first-order Raman modes is highly dependent on the excitation en-

ergy for both pristine and defective 1L-MoS_2. As anticipated, of particular interest is the spectral region featuring the second-order Raman processes, in the range 400-480 cm^{-1}. The second-order Raman spectrum of MoS_2 and other semiconducting transition-metal dichalcogenides hosts a rich variety of features, which are strongly dependent on the number of layers and the excitation laser energy. However, in the published works on 2-D MoS_2, the second-order Raman bands were probed using only few laser excitation lines[159].

Fig. 4.9(c, d) shows a multiple excitation Raman map for pristine 1L-MoS_2 and bulk MoS_2. The horizontal scale represents the Raman shift, whereas the vertical scale is the laser excitation energy. One can clearly observe the resonances of all Raman bands across the A ($\sim$1.89 eV) and B ($\sim$2.06 eV) excitonic transitions, which are marked by horizontal dashed lines. A multiple Lorentzian peak fit has been used to identify the spectral position of the measured Raman bands. Although the determination of the lineshapes would require a complete theoretical description of the Raman intensities, a sum of Lorentzian curves provides a means to associate each feature in the spectrum to a specific phonon. This is only intended to provide a reliable estimate of the spectral position of the different contributions to the second-order Raman bands. The central goal of this work is to achieve a quantitative comparison between the measured and the calculated spectra within the entire spectral range considered, while making use of a dense sampling in terms of laser energies. Constant values for the FWHM have been imposed as constrains in the fitting analysis, leaving intensities and positions unconstrained. This procedure was adopted to decrease the number of fitting parameters since the FWHM is not expected to depend significantly on the laser energy within this narrow energy range (1.85-2.18 eV). The number of Lorentzians is gradually increased until a pre-defined convergence threshold is reached.

An important result is the dispersion of some Raman features as the laser energy changes, as clearly revealed by the dashed lines tracking the Raman peak positions. In particular, in this analysis, the 2LA band was fitted with four peaks (see Fig. 4.9 (a, b)): a peak around 440 cm^{-1} and three

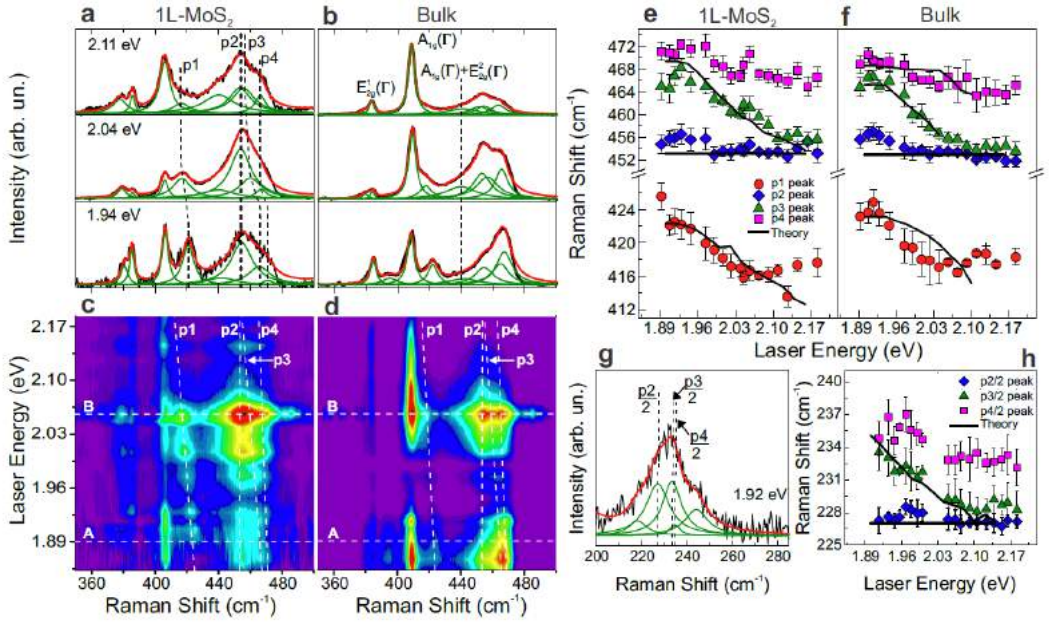

Figure 4.9: (a) and (b) Raman spectra (red curves) and fits (green curves) of 1L and bulk MoS_2 measured with three laser excitation energies: 1.94 eV, 2.04 eV and 2.11 eV. The second-order bands of interest are denoted p_1, p_2, p_3, p_4. The 440 cm^{-1} peak is assigned to the $A_{1g}+ E^2_{2g}$ combination mode after Ref.[147]. (c, d) Resonant Raman maps with more than 20 different laser lines of 1L and bulk MoS_2 showing the enhancement of the Raman bands across the A and B excitons (horizontal dashed lines). (e, f) Laser energy dependence of the experimental values of the positions of the p_1, p_2, p_3, p_4 peaks (symbols) of 1L and bulk MoS_2 , and the calculated dispersion of these peaks (solid curves). (g) Raman spectrum of a defective 1L-MoS_2 sample, showing the disorder-induced bands associated with acoustic phonons near the edges of the Brillouin zone. The band was fit to a sum of Lorentzians with frequencies half the frequencies of p_2, p_3, p_4. (h) Laser energy dependence of the experimental values of $p_2/2$, $p_3/2$, and $p_4/2$ (symbols) shown in (g), and the calculated dispersion of these disorder-induced peaks (solid curves) assuming one-phonon-defect DRR scattering. The absence of the theoretical curve for the p_4 peak in e,h is due to its weak intensity, not observable in the calculated Raman spectra. The error bars in e,f,h represent the standard error from the fitting process.

peaks hereby named p_2, p_3, p_4. The 440 cm^{-1} peak was recently ascribed in Ref.[147] to the $A_{1g}+ E^2_{2g}$ combination mode. In addition, Fig. 4.9 (a, b) highlights the presence of an additional band, referred to as p_1 henceforth. Most notably, the p_1, p_3 and p_4 peaks red-shift as the laser excitation energy increases. Such dispersive behaviour is characteristic of double-resonance Raman (DRR) processes. DRR is a kind of second-order process that involves the resonant scattering of excited electrons by phonons, and can be used as a unique experimental tool to study electrons, phonons, and their interplay. By varying the incoming photon energy, the DRR condition selects different electronic states and different pairs of phonons with opposite finite momenta within the interior of the BZ. For graphene, the most important DRR features, the D and 2D bands, provide rich physical information about the sample.

To support the identification and assignment of the different contributions to the DRR process, first-principles calculations of the second-order Raman spectra of 1L-MoS_2 and bulk MoS_2 have been performed using the electronic structure and phonon dispersion obtained from DFT, by the team led by M. Pimenta. The Methods section and Ref. 160 contain additional details of the calculations. In essence, the intensity of a second-order Raman process is obtained within the perturbation theory framework, which describes microscopically the inelastic light by phonons. Matrix elements including electron-phonon interactions represent each the complex amplitude of the corresponding elementary process. Given the matrix elements, the intensity of the Raman process can be computed by summing the matrix element squares over the phonon wavevector. Only electron-electron processes are included in the calculations; processes involving hole scattering events have not been taken into account at present.

The different contributions to the 2LA band are identified by comparing the experimental and calculated multiple excitation Raman spectra of 1L- and bulk MoS_2.The calculated spectral positions of each Raman feature (represented by black solid lines) as a function of the laser energy are superposed on the experimental data (coloured symbols) in Fig. 4.9(e, f), showing a very good agreement between the experimental and calculated results. The

non-dispersive behaviour of p_2 (see Fig. 4.9(e, f)) shows that it corresponds to a conventional second-order Raman process. The experimental frequency of p_2 is found to match with twice the calculated frequency of the van Hove singularity in the phonon density of states from a saddle point between M and K. Thus, the origin of p_2 is ascribed to such van Hove singularity. On the other hand, p_1, p_3 and p_4 exhibit a dispersive behaviour, a signature of a DRR process due to photons with different energies selecting electrons and phonons with different wave vectors in the BZ.

Fig. 4.9(e, f) shows an excellent agreement between the experimental values of the p_1 positions (red circles) and the dispersion of the calculated peak (black curve), when considering an intervalley DRR process involving one LA phonon and one TA phonon in the vicinity of **K**. Thus, p_1 is assigned to LA($\sim$(K))+TA($\sim$(K)). According to the calculations, the combined energy of the relevant LA + TA phonons near **K** is found to red-shift as the incident laser energy increases, dispersing at a rate of $\sim$ 43 cm^{-1}/eV, which is reproduced in the experiments.

Following similar arguments based on the comparison between the experimental and calculated dispersion rate, the p_3 and p_4 peaks are assigned to 2LA($\sim$**K**) and 2LA($\sim$**M**), respectively. As the laser energy increases, p_3, and p_4 disperse at rates of $\sim$ 49 and $\sim$ 21 cm^{-1}/eV, respectively, and this result reflects the different slopes of the LA phonon dispersion near **K** and **M** of MoS_2. The p_3 peak is representative of a scattering process between **K** and **K'**, involving two LA phonons in the vicinity of the **K** point, whereas p_4 is related to the scattering of excited electrons bewteen the **K** and **Q** valleys, by two LA phonons near **M**.

Therefore, the broad and asymmetric band centered around 460 cm^{-1} can be overall explained by contributions from LA phonons near the saddle point between **K** and **M**, and from LA phonons near $\sim$**K** and $\sim$**M**, which are enhanced in the spectra by the intervalley DRR process. By varying the incoming photon energy, the DRR condition, schematically depicted in Fig. 4.10 (a), selects different electronic states in the **K** valley, and different pairs of phonons with opposite finite momenta near the **M** and **K** points of the BZ (see Fig. 4.10(b)).

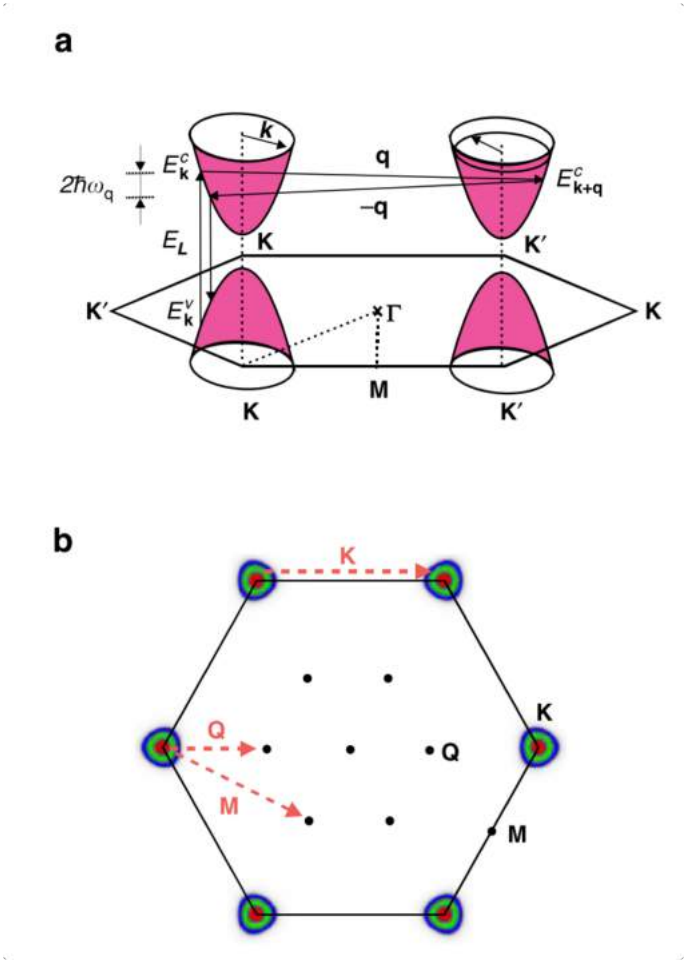

Figure 4.10: (a) Schematic representation of a DRR process where excited electronic states are connected by two phonons with opposite momenta **q** and **-q**. The DRR process begins with an incoming photon creating an electron-hole pair near the **K** valley. The electron is then inelastically scattered by the emission of a phonon with wave vector **q** to the **K'** valley. After that, the electron is scattered back to the **K** valley by the emission of a second phonon with wave vector **-q**, and the electron-hole pair recombines emitting a photon (Stokes scattering). (b) Locus of electronic states that participate in the DRR Raman process around **K** for laser energies of 1.9, 2.0 and 2.1 eV in red, green and blue. Possible phonon wave vectors that connect these states with each other and with other high-symmetry points (**M** and **Q**) are shown as red dashed arrows. **Q** is another conduction band local minimum located halfway between **Γ** and **K**. Besides the two main scattering processes giving rise to p_3 and p_4 (indicated by the **K** and **M** dashed arrows, respectively), there is another possible scattering process between the **K** and the **Q** valley, indicated by the **Q** dashed arrow . This was not detected experimentally in the present study due to its almost vanishing electron-phonon coupling.

As a further verification of the proposed DRR conclusions, a defect-induced resonant Raman spectrum is shown in Fig. 4.9(g) for defective 1L-MoS_2, for an excitation energy of 1.92 eV. From a fit of the defect-induced Raman band around 227 cm^{-1}, one can identify three peaks located at 227 cm^{-1}, 234 cm^{-1}, and 235 cm^{-1}, corresponding respectively to one-half the frequencies of the p_2, p_3, and p_4 peaks. Fig. 4.9(g) indicates the presence of two additional peaks, needed in order to ensure the convergence of the fitting process. While their origin is at present uncertain, they might be related to other contributions, in the phonon density of states, to second-order Raman scattering . Fig. 4.9(h) shows half the frequencies of p_2, p_3, and p_4 as a function of the laser excitation energy, superposed on the calculated dispersion of the DRR features considering, now, scattering by a phonon and a defect. This process is similar to the disorder-induced D band in graphene, which also comes from a DRR process involving just one phonon, where momentum conservation is provided by elastic scattering of the excited electron by a defect.The excellent agreement with the theory and experiment further supports the interpretation of the second-order DRR features, and highlights the role of intervalley elastic scattering by defects.

4.6 Photoluminescence

Fig.4.11 shows the PL spectrum of pristine 1L-MoS_2. Fitting the curve with Lorentzian lineshapes, one can resolve features corresponding to the A (1.88 eV) and the B (2.0 eV) exciton peaks, originating from the valence band splitting at **K**-point[11,12]. The prominent trion peak A^- (1.83 eV) is an indication that the as-prepared samples are n-doped[21], as usually expected in mechanically exfoliated MoS_2 on Si/SiO_2 substrates[10].

With increasing ion dosing, one can observe an overall reduction of PL intensity (see Fig.4.11a). This is due to defects acting as quenching sites for PL processes. Similar results have been obtained previously using low-energy Ar^+ bombardment[161]. However, a new feature is also present at 1.7 eV (X^0) (see Fig.4.11), which can be attributed to bound excitons (A excitons bound to defects)[162,163]. As shown in Fig.4.11(c), the intensity of the defect-induced

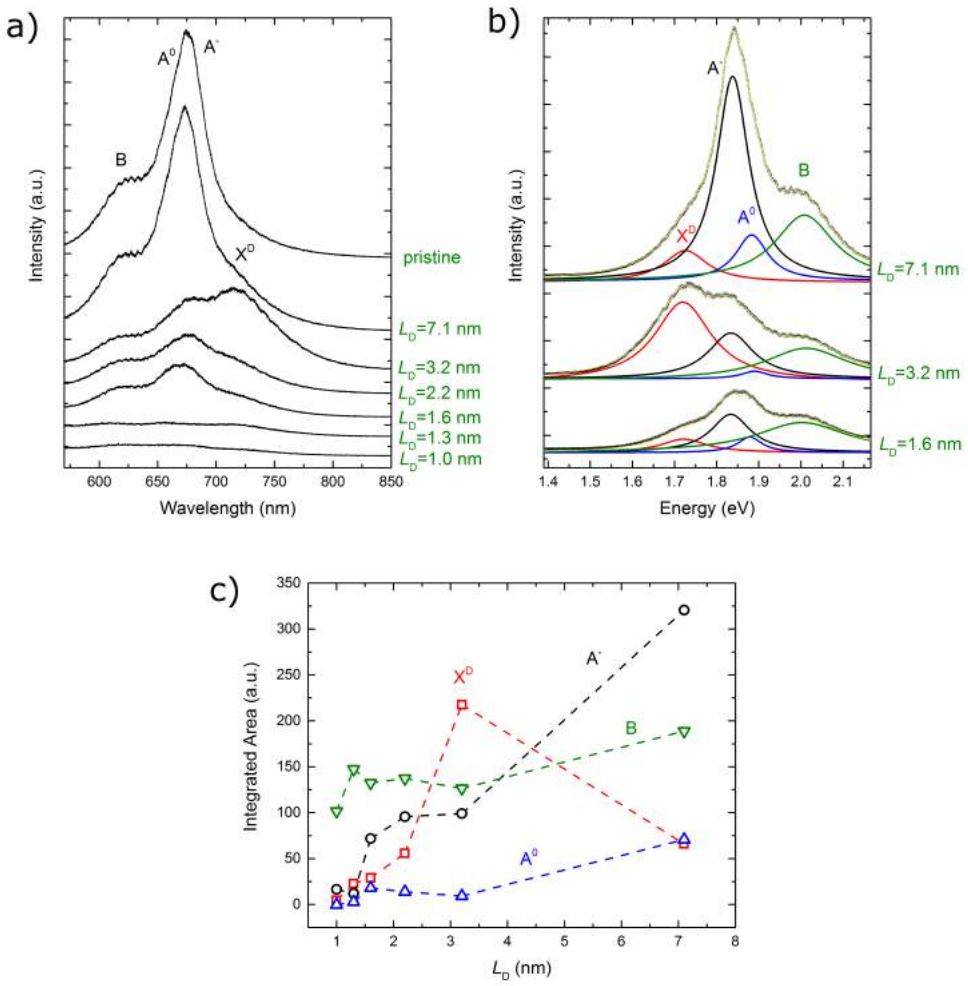

Figure 4.11: (a) Evolution of the PL signal, (b) corresponding fits and (c) evolution of the PL integrated areas for the distint PL contributions A^0, A−, B, X^0 of 1L-MoS_2 as a function of decreasing inter-defect distance.

feature X^0 initially increases with disorder (decreasing L_D), and then vanishes together with the overall PL signal intensity for L_D<3 nm.

4.7 Conclusion

In summary, a comprehensive investigation of the effects of defects induced by Mn^+ ion bombardment in the Raman spectrum of 1L-MoS_2 has been carried out. The degree of disorder has been quantified by the inter-defect distance L_D. The E' peak and the A_1' peak have been found to broaden upon increasing the defect density, which is accompanied by a downshift of the position of the E'-peak and an upshift of the position of the A_1'-peak. Using DFT calculations of the phonon dispersion, the evolution of these first-order peaks has been explained as due to phonon confinement. Moreover, the introduced disorder activates new Raman modes, many of which have not been observed in the literature, and have been assigned as arising from zone-edge phonons. Among these, a particular attention has been given to the $\sim$227 cm^{-1} peak, which has been assigned to LA phonons at the **M**-point. A phenomenological relationship between the intensity ratio of the LA(M) peak and each of the first-order peaks has been proposed, allowing a fast and practical quantification of defects in 1L-MoS_2 using Raman spectroscopy. Finally, multiwavelength Raman spectroscopy has shed light on double resonance Raman scattering phenomena, which are likely to trigger a debate on the role of the electron-phonon coupling in the Raman scattering of 1L-MoS_2 and other two-dimensional transition metal dichalcogenides.

5

Conclusions and future outlook

In conclusion, a high-resolution, near-field spectroscopy setup (described in Chapter 2) has enabled me to study the nanoscale details of 2-D crystals surface structure, which plays a crucial role towards understanding of the impact of defects on the properties of atomically thin materials. I have outlined that, despite defects may be seen as detrimental for the optoelectronic properties of 2-D materials, their intentional creation on the nanoscale may offer an additional degree of freedom for engineering their properties.

As reported in Chapter 3, I have probed the nanoscale distribution of point-like defects in graphene. The measured TERS spectra have enabled direct determination of the average inter-defect distance within the graphene sheet; furthermore, analysis of the TERS enhancement factor of the graphene Raman peaks has highlighted the preferential enhancement and symmetry-dependent selectivity of the defective D-peak intensity. Motivated by the latter experimental finding, I have developed an analytical model to describe near-field imaging of point-like Raman sources, which can be regarded as

zero-dimensional scatterers. The near-field images constructed from the computed Raman intensities has been found to depend on the symmetry of the corresponding Raman tensors and on the orientation of the scatterers. This model can be both used to explain the different near-field Raman enhancement found for different Raman bands in graphene, and it can be generally applied to inelastic scattering of molecules.

In the light of the successful optical characterization of nanoscale defects in graphene by means of Raman spectroscopy, I have found it timely to expand the study of structural defects to other less investigated two-dimensional crystals, such as MoS_2. In Chapter 4, I have studied defect-induced Raman scattering of single-layer MoS_2 by means of the controlled introduction of defects using ion-bombardment. I have used a phonon confinement model to explain the systematic evolution of peak widths and shifts as a function of defect density, and I have developed a metric based on the measured Raman intensities to quantify defect density. Multiwavelength Raman spectroscopy has revealed the origin of the defective and second-order Raman bands, and ascribed it to double-resonance Raman scattering.

Bibliography

1. K. S. Novoselov, D. Jiang, F. Schedin, T. J. Booth, V. V. Khotkevich, S. V. Morozov, and A. K. Geim, "Two-dimensional atomic crystals.," *Proceedings of the National Academy of Sciences of the United States of America*, vol. 102, no. 30, pp. 10451–10453, 2005.

2. R. Peierls, "Quelques proprietes typiques des corpes solides," *Ann. I. H. Poincare*, vol. 5, 1935.

3. L. D. Landau, "Zur theorie der phasenumwandlungen," *Phys. Z. Sowjetunion*, vol. 11, no. 6, p. 26, 1935.

4. N. Mermin and Wagner H., "Absence of Ferromagnetism or Antiferromagnetism in One- or Two-Dimensional Isotropic Heisenberg Models," vol. 17, no. 22, pp. 1133–1136, 1966.

5. J. C. Meyer, a. K. Geim, M. I. Katsnelson, K. S. Novoselov, T. J. Booth, and S. Roth, "The structure of suspended graphene sheets.," *Nature*, vol. 446, no. 7131, pp. 60–3, 2007.

6. A. K. Geim and K. S. Novoselov, "The rise of graphene.," *Nature Materials*, vol. 6, no. 3, pp. 183–91, 2007.

7. A. S. Mayorov, R. V. Gorbachev, S. V. Morozov, L. Britnell, R. Jalil, L. A. Ponomarenko, P. Blake, K. S. Novoselov, K. Watanabe, T. Taniguchi, and A. K. Geim, "Micrometer-Scale Ballistic Transport in Encapsulated Graphene at Room Temperature," pp. 2396–2399, 2011.

8. H. Wang, T. Maiyalagan, and X. Wang, "Review on Recent Progress in Nitrogen-Doped Graphene : Synthesis , Characterization , and Its Potential Applications," *ACS Catalysis*, 2012.

9. D. PacileÌĄ, J. C. Meyer, C. O. Girit, and a. Zettl, "The two-dimensional phase of boron nitride: Few-atomic-layer sheets and suspended membranes," *Applied Physics Letters*, vol. 92, no. 13, p. 133107, 2008.

10. B. Radisavljevic, A. Radenovic, J. Brivio, V. Giacometti, and A. Kis, "Single-layer MoS_2 transistors.," *Nature Nanotechnology*, vol. 6, no. 3, pp. 147–150, 2011.

11. K. F. Mak, C. Lee, J. Hone, J. Shan, and T. F. Heinz, "Atomically Thin MoS_2 : A New Direct-Gap Semiconductor," *Physical Review Letters*, vol. 105, p. 136805, 2010.

12. A. Splendiani, L. Sun, Y. Zhang, T. Li, J. Kim, C.-Y. Chim, G. Galli, and F. Wang, "Emerging photoluminescence in monolayer MoS_2.," *Nano Letters*, vol. 10, no. 4, pp. 1271–1275, 2010.

13. R. S. Sundaram, M. Engel, A. Lombardo, R. Krupke, A. C. Ferrari, P. Avouris, and M. Steiner, "Electroluminescence in single layer MoS_2.," *Nano Letters*, vol. 13, no. 4, pp. 1416–21, 2013.

14. K. F. Mak, K. He, J. Shan, and T. F. Heinz, "Control of valley polarization in monolayer MoS_2 by optical helicity," *Nature Nanotechnology*, vol. 7, no. 8, pp. 494–498, 2012.

15. H. Zeng, J. Dai, W. Yao, D. Xiao, and X. Cui, "Valley polarization in MoS_2 monolayers by optical pumping.," *Nature Nanotechnology*, vol. 7, no. 8, pp. 490–3, 2012.

16. R. E. Franklin, "The Structure of Graphitic Carbons," *Acta Cryst.*, vol. 4, p. 253, 1951.

17. A. H. Castro Neto, F. Guinea, N. M. R. Peres, K. S. Novoselov, and A. K. Geim, "The electronic properties of graphene," *Reviews of Modern Physics*, vol. 81, no. 1, pp. 109–162, 2009.

18. Y. Ding, Y. Wang, J. Ni, L. Shi, S. Shi, and W. Tang, "First principles study of structural, vibrational and electronic properties of graphene-like MX2 (M=Mo, Nb, W, Ta; X=S, Se, Te) monolayers," *Physica B: Condensed Matter*, vol. 406, no. 11, pp. 2254–2260, 2011.

19. T. Li and G. Galli, "Electronic Properties of MoS 2 Nanoparticles," vol. 12, pp. 16192–16196, 2007.

20. N. Scheuschner, O. Ochedowski, A.-m. Kaulitz, R. Gillen, M. Schleberger, and J. Maultzsch, "Photoluminescence of freestanding single- and few-layer MoS_2," *Physical Review B*, vol. 89, no. 125406, pp. 1–6, 2013.

21. K. F. Mak, K. He, C. Lee, G. H. Lee, J. Hone, T. F. Heinz, and J. Shan, "Tightly bound trions in monolayer MoS_2," *Nature Materials*, vol. 12, no. 3, pp. 207–11, 2013.

22. F. Bonaccorso, A. Lombardo, T. Hasan, Z. Sun, L. Colombo, and A. C. Ferrari, "Production and processing of graphene and 2d crystals," *Materials Today*, vol. 15, no. 12, pp. 564–589, 2012.

23. H. Li, Q. Zhang, C. C. R. Yap, B. K. Tay, T. H. T. Edwin, A. Olivier, and D. Baillargeat, "From Bulk to Monolayer MoS_2: Evolution of Raman Scattering," *Advanced Functional Materials*, vol. 22, no. 7, pp. 1385–1390, 2012.

24. A. Geim, "Graphene: Status and Prospects," *Science*, no. 6, pp. 1–8, 2009.

25. M. M. Benameur, B. Radisavljevic, J. S. Héron, S. Sahoo, H. Berger, and A. Kis, "Visibility of dichalcogenide nanolayers," *Nanotechnology*, vol. 22, p. 125706, 2011.

26. X. Li, W. Cai, J. An, S. Kim, J. Nah, D. Yang, R. Piner, A. Velamakanni, I. Jung, E. Tutuc, S. K. Banerjee, L. Colombo, and R. S. Ruoff, "Large-area synthesis of high-quality and uniform graphene films on copper foils.," *Science (New York, N.Y.)*, vol. 324, pp. 1312–4, June 2009.

27. J.-U. Lee, D. Yoon, and H. Cheong, "Estimation of Young's Modulus of Graphene by Raman Spectroscopy," *Nano Letters*, vol. 12, pp. 4444–4448, 2012.

28. Y. Zhan, Z. Liu, S. Najmaei, P. M. Ajayan, and J. Lou, "Large-area vapor-phase growth and characterization of MoS(2) atomic layers on a SiO(2) substrate.," *Small (Weinheim an der Bergstrasse, Germany)*, vol. 8, no. 7, pp. 966–71, 2012.

29. K.-K. Liu, W. Zhang, Y.-H. Lee, Y.-C. Lin, M.-T. Chang, C.-Y. Su, C.-S. Chang, H. Li, Y. Shi, H. Zhang, C.-S. Lai, and L.-J. Li, "Growth of large-area and highly crystalline MoS_2 thin layers on insulating substrates.," *Nano letters*, vol. 12, pp. 1538–44, Mar. 2012.

30. S. Balendhran, J. Z. Ou, M. Bhaskaran, S. Sriram, S. Ippolito, Z. Vasic, E. Kats, S. Bhargava, S. Zhuiykov, and K. Kalantar-Zadeh, "Atomically thin layers of MoS_2 via a two step thermal evaporation-exfoliation method.," *Nanoscale*, vol. 4, no. 2, pp. 461–6, 2012.

31. J. Hass, W. a. de Heer, and E. H. Conrad, "The growth and morphology of epitaxial multilayer graphene," *Journal of Physics: Condensed Matter*, vol. 20, no. 32, p. 323202, 2008.

32. A. Charrier, A. Coati, T. Argunova, F. Thibaudau, Y. Garreau, R. Pinchaux, I. Forbeaux, J.-M. Debever, M. Sauvage-Simkin, and J.-M. Themlin, "Solid-state decomposition of silicon carbide for growing ultrathin heteroepitaxial graphite films," *Journal of Applied Physics*, vol. 92, no. 5, p. 2479, 2002.

33. M. Lotya, Y. Hernandez, P. J. King, R. J. Smith, V. Nicolosi, L. S. Karlsson, F. M. Blighe, S. De, Z. Wang, I. T. McGovern, G. S. Duesberg,

and J. N. Coleman, "Liquid phase production of graphene by exfoliation of graphite in surfactant/water solutions.," *Journal of the American Chemical Society*, vol. 131, pp. 3611–20, Mar. 2009.

34. M. Z. Hasan and C. L. Kane, "Colloquium: Topological insulators," *Reviews of Modern Physics*, vol. 82, no. 4, pp. 3045–3067, 2010.

35. A. A. Green and M. C. Hersam, "Solution phase production of graphene with controlled thickness via density differentiation.," *Nano letters*, vol. 9, pp. 4031–6, Dec. 2009.

36. O. M. Maragò, F. Bonaccorso, R. Saija, P. G. Gucciardi, G. Calogero, P. H. Jones, F. Borghese, P. Denti, V. Nicolosi, and A. C. Ferrari, "Brownian Motion of Graphene," *ACS nano*, pp. 1–5, 2010.

37. Y. Hernandez, V. Nicolosi, M. Lotya, F. M. Blighe, Z. Sun, S. De, I. T. McGovern, B. Holland, M. Byrne, Y. K. Gun'Ko, J. J. Boland, P. Niraj, G. Duesberg, S. Krishnamurthy, R. Goodhue, J. Hutchison, V. Scardaci, A. C. Ferrari, and J. N. Coleman, "High-yield production of graphene by liquid-phase exfoliation of graphite.," *Nature nanotechnology*, vol. 3, no. 9, pp. 563–8, 2008.

38. F. Torrisi, T. Hasan, W. Wu, Z. Sun, A. Lombardo, T. S. Kulmala, G.-W. Hsieh, S. Jung, F. Bonaccorso, P. J. Paul, D. Chu, and A. C. Ferrari, "Inkjet-Printed Graphene Electronics," *ACS Nano*, no. 4, pp. 2992–3006, 2012.

39. J. N. Coleman, M. Lotya, A. O'Neill, S. D. Bergin, P. J. King, U. Khan, K. Young, A. Gaucher, S. De, R. J. Smith, I. V. Shvets, S. K. Arora, G. Stanton, H.-Y. Kim, K. Lee, G. T. Kim, G. S. Duesberg, T. Hallam, J. J. Boland, J. J. Wang, J. F. Donegan, J. C. Grunlan, G. Moriarty, A. Shmeliov, R. J. Nicholls, J. M. Perkins, E. M. Grieveson, K. Theuwissen, D. W. McComb, P. D. Nellist, and V. Nicolosi, "Two-dimensional nanosheets produced by liquid exfoliation of layered materials.," *Science (New York, N.Y.)*, vol. 331, no. 6017, pp. 568–71, 2011.

40. K.-G. Zhou, N.-N. Mao, H.-X. Wang, Y. Peng, and H.-L. Zhang, "A mixed-solvent strategy for efficient exfoliation of inorganic graphene analogues.," *Angewandte Chemie (International ed. in English)*, vol. 50, pp. 10839–42, Nov. 2011.

41. A. C. Ferrari and D. M. Basko, "Raman spectroscopy as a versatile tool for studying the properties of graphene.," *Nature Nanotechnology*, vol. 8, no. 4, pp. 235–46, 2013.

42. P. H. Tan, W. P. Han, W. J. Zhao, Z. H. Wu, K. Chang, H. Wang, Y. F. Wang, N. Bonini, N. Marzari, N. Pugno, G. Savini, A. Lombardo, and A. C. Ferrari, "The shear mode of multilayer graphene.," *Nature Materials*, vol. 11, no. 4, pp. 294–300, 2012.

43. C. Lee, H. Yan, L. E. Brus, T. F. Heinz, J. Hone, and S. Ryu, "Anomalous Lattice Vibrations of Single- and Few-Layer MoS_2," *ACS Nano*, vol. 4, no. 5, pp. 2695–2700, 2010.

44. T. Sekine, K. Uchinokura, T. Nakashizu, E. Matsuura, and R. Yoshizaki, "Dispersive Raman Mode of Layered Compound 2H-MoS_2 under the Resonant Condition," *Journal of the Physical Society of Japan*, vol. 53, no. 2, pp. 811–818, 1984.

45. L. M. Malard, M. A. Pimenta, G. Dresselhaus, and M. S. Dresselhaus, "Raman spectroscopy in graphene," *Physics Reports*, vol. 473, no. 5-6, pp. 51–87, 2009.

46. S. Reich and C. Thomsen, "Raman spectroscopy of graphite.," *Philosophical Transactions of the Royal Society of London A*, vol. 362, no. 1824, pp. 2271–88, 2004.

47. A. C. Ferrari and J. Robertson, "Interpretation of Raman spectra of disordered and amorphous carbon," *Physical Review B*, vol. 61, no. 20, pp. 14095–14107, 2000.

48. F. Tuinstra and J. L. Koenig, "Raman Spectrum of Graphite," *The Journal of Chemical Physics*, vol. 53, no. 3, p. 1126, 1970.

49. A. C. Ferrari and J. Robertson, "Raman spectroscopy of amorphous, nanostructured, diamond-like carbon, and nanodiamond.," *Philosophical transactions. Series A, Mathematical, physical, and engineering sciences*, vol. 362, no. 1824, pp. 2477–2512, 2004.

50. A. Ferrari and J. Robertson, "Origin of the 1150-cm-1 Raman mode in nanocrystalline diamond," *Physical Review B*, vol. 63, no. 12, p. 121405, 2001.

51. A. C. Ferrari, "Raman spectroscopy of graphene and graphite: Disorder, electron-phonon coupling, doping and nonadiabatic effects," *Solid State Communications*, vol. 143, no. 1-2, pp. 47–57, 2007.

52. A. C. Ferrari, J. C. Meyer, V. Scardaci, C. Casiraghi, M. Lazzeri, F. Mauri, S. Piscanec, D. Jiang, K. S. Novoselov, S. Roth, and A. K. Geim, "Raman Spectrum of Graphene and Graphene Layers," *Physical Review Letters*, vol. 97, no. 18, p. 187401, 2006.

53. I. Pocsik, M. Hundhausen, M. Koos, and L. Ley, "Origin of the D peak in the Raman spectrum of microcrystalline graphite," *Journal of Non-Crystalline Solids*, pp. 1083–1086, 1998.

54. F. Herziger, P. May, and J. Maultzsch, "Layer-number determination in graphene by out-of-plane phonons," *Physical Review B - Condensed Matter and Materials Physics*, vol. 85, no. 23, pp. 1–5, 2012.

55. C. Casiraghi, A. Hartschuh, H. Qian, S. Piscanec, C. Georgi, A. Fasoli, K. S. Novoselov, D. M. Basko, and A. C. Ferrari, "Raman spectroscopy of graphene edges," *Nano Letters*, vol. 9, no. 4, pp. 1433–41, 2009.

56. L. G. Cançado, M. Pimenta, B. Neves, M. Dantas, and A. Jorio, "Influence of the Atomic Structure on the Raman Spectra of Graphite Edges," *Physical Review Letters*, vol. 93, no. 24, p. 247401, 2004.

57. N. Scheuschner, R. Gillen, M. Staiger, and J. Maultzsch, "Interlayer resonant Raman modes in few-layer MoS_2," *Physical Review B*, vol. 91, no. 23, pp. 1–10, 2015.

58. A. G. Bagnall, W. Y. Liang, E. A. Marseglia, and B. Welber, "Raman Studies of MoS_2 at High Pressure," *Physica 99B*, pp. 343–346, 1980.

59. J. Wessel, "Surface-enhanced optical microscopy," *Journal of the Optical Society of America B*, vol. 2, no. 9, p. 1538, 1985.

60. R. M. Stockle, Y. D. Suh, V. Deckert, and R. Zenobi, "Nanoscale chemical analysis by tip-enhanced Raman spectroscopy," *Chemical Physics Letters*, vol. 318, pp. 131–136, 2000.

61. N. Hayazawa, Y. Inouye, Z. Sekkat, and S. Kawata, "Metallized tip amplification of near-field Raman scattering," *Optics Communications*, vol. 183, pp. 333–336, 2000.

62. M. S. Anderson, "Locally enhanced Raman spectroscopy with an atomic force microscope," *Applied Physics Letters*, vol. 76, no. 21, p. 3130, 2000.

63. C. Blum, L. Opilik, J. M. Atkin, K. Braun, S. B. Kämmer, V. Kravtsov, N. Kumar, S. Lemeshko, J.-F. Li, K. Luszcz, T. Maleki, A. J. Meixner, S. Minne, M. B. Raschke, B. Ren, J. Rogalski, D. Roy, B. Stephanidis, X. Wang, D. Zhang, J.-H. Zhong, and R. Zenobi, "Tip-enhanced Raman spectroscopy - an interlaboratory reproducibility and comparison study," *Journal of Raman Spectroscopy*, vol. 45, no. 1, pp. 22–31, 2014.

64. R. Zhang, Y. Zhang, Z. C. Dong, S. Jiang, C. Zhang, L. G. Chen, L. Zhang, Y. Liao, J. Aizpurua, Y. Luo, J. L. Yang, and J. G. Hou, "Chemical mapping of a single molecule by plasmon-enhanced Raman scattering.," *Nature*, vol. 498, no. 7452, pp. 82–6, 2013.

65. S. Najjar, D. Talaga, L. Schue, Y. Coffinier, S. Szunerits, R. Boukherroub, L. Servant, V. Rodriguez, and S. Bonhommeau, "Tip-enhanced raman spectroscopy of combed double-stranded DNA bundles," *Journal of Physical Chemistry C*, vol. 118, no. 2, pp. 1174–1181, 2014.

66. H. Wang, J. H. Strait, P. a. George, S. Shivaraman, V. B. Shields, M. Chandrashekhar, J. Hwang, F. Rana, M. G. Spencer, C. S. Ruiz-Vargas, and J. Park, "Ultrafast relaxation dynamics of hot optical

phonons in graphene," *Applied Physics Letters*, vol. 96, no. 8, p. 081917, 2010.

67. E. M. van Schrojenstein Lantman, T. Deckert-Gaudig, A. J. G. Mank, V. Deckert, and B. M. Weckhuysen, "Catalytic processes monitored at the nanoscale with tip-enhanced Raman spectroscopy.," *Nature Nanotechnology*, vol. 7, no. 9, pp. 583–6, 2012.

68. N. Lee, R. D. Hartschuh, D. Mehtani, A. Kisliuk, J. F. Maguire, M. Green, M. D. Foster, and A. P. Sokolov, "High contrast scanning nano-Raman spectroscopy of silicon," *Journal of Raman Spectroscopy*, pp. 789–796, 2007.

69. Y. Okuno, Y. Saito, S. Kawata, and P. Verma, "Tip-Enhanced Raman Investigation of Extremely Localized Semiconductor-to-Metal Transition of a Carbon Nanotube," *Physical Review Letters*, vol. 111, no. 21, p. 216101, 2013.

70. W. Su and D. Roy, "Visualizing graphene edges using tip-enhanced Raman spectroscopy," *Journal of Vacuum Science & Technology B: Microelectronics and Nanometer Structures*, vol. 31, no. 4, p. 041808, 2013.

71. B.-S. Yeo, J. Stadler, T. Schmid, R. Zenobi, and W. Zhang, "Tip-enhanced Raman Spectroscopy âĂŞ Its status, challenges and future directions," *Chemical Physics Letters*, vol. 472, no. 1-3, pp. 1–13, 2009.

72. T. Schmid, B. Yeo, G. Leong, J. Stadler, and R. Zenobi, "Performing tip-enhanced Raman spectroscopy in liquids," *Journal of Raman Spectroscy*, vol. 40, pp. 1392–9, 2009.

73. B. Huang, M. Bates, and X. Zhuang, "Super-resolution fluorescence microscopy.," *Annu Rev Biochem.*, vol. 78, pp. 993–1016, 2009.

74. B. R. Wood, E. Bailo, M. A. Khiavi, L. Tilley, S. Deed, and T. Deckert-Gaudig, "Tip-enhanced Raman scattering (TERS) from hemozoin crystals within a sectioned erythrocyte.," *Nano Letters*, vol. 11, pp. 1868–73, 2011.

75. R. Bohme, M. Richter, D. Cialla, P. Rosch, V. Deckert, and J. Popp, "Towards a specific characterisation of components on a cell surface - combined TERS-investigations of lipids and human cells.," *Journal of Raman Spectroscy*, vol. 40, pp. 1452–7, 2009.

76. E. Lipiec, R. Sekine, J. Bielecki, W. M. Kwiatek, and B. R. Wood, "Molecular characterization of DNA double strand breaks with tip-enhanced Raman scattering," *Angewandte Chemie - International Edition*, vol. 53, no. 1, pp. 169–172, 2014.

77. T. Deckert-Gaudig and V. Deckert, "Ultraflat transparent gold nanoplates–ideal substrates for tip-enhanced Raman scattering experiments.," *Small*, vol. 5, no. 4, pp. 432–6, 2009.

78. D. Kurouski, S. Zaleski, F. Casadio, R. P. V. Duyne, and N. C. Shah, "Tip-Enhanced Raman Spectroscopy (TERS) for in Situ Identification of Indigo and Iron Gall Ink on Paper," *Journal of the American Chemical Society*, vol. 136, pp. 8677–8684, 2014.

79. L. N. Hecht and B., *Principles of Nano-Optics*. New York: Cambridge University Press, 2006.

80. D. Roy and C. Williams, "High resolution Raman imaging of single wall carbon nanotubes using electrochemically etched gold tips and a radially polarized annular beam," *Journal of Vacuum Science & Technology A: Vacuum, Surfaces, and Films*, vol. 28, no. 3, p. 472, 2010.

81. A. Taguchi, N. Hayazawa, Y. Saito, H. Ishitobi, A. Tarun, and S. Kawata, "Controlling the plasmon resonance wavelength in metal-coated probe using refractive index modification.," *Optics Express*, vol. 17, no. 8, pp. 6509–18, 2009.

82. N. Hayazawa, T.-A. Yano, and S. Kawata, "Highly reproducible tip-enhanced Raman scattering using an oxidized and metallized silicon cantilever tip as a tool for everyone," *Journal of Raman Spectroscopy*, vol. 43, pp. 1177–1182, 2012.

83. N. Kumar, A. Rae, and D. Roy, "Accurate measurement of enhancement factor in tip-enhanced Raman spectroscopy through elimination of far-field artefacts," *Applied Physics Letters*, vol. 104, no. 12, p. 123106, 2014.

84. A. G. T. Ruiter, K. O. Van Der Werf, J. A. Veerman, M. F. Garcia-Parajo, W. H. J. Rensen, and N. F. Van Hulst, "Tuning fork shear-force feedback," *Ultramicroscopy*, vol. 71, no. 1-4, pp. 149–157, 1998.

85. J. S. Lloyd, A. Williams, R. H. Rickman, A. McCowen, and P. R. Dunstan, "Reproducible electrochemical etching of silver probes with a radius of curvature of 20 nm for tip-enhanced Raman applications," *Applied Physics Letters*, vol. 99, no. 14, pp. 2011–2014, 2011.

86. M. M. Lucchese, F. Stavale, E. H. M. Ferreira, C. Vilani, M. V. O. Moutinho, R. B. Capaz, C. A. Achete, and A. Jorio, "Quantifying ion-induced defects and Raman relaxation length in graphene," *Carbon*, vol. 48, no. 5, pp. 1592–1597, 2010.

87. L. G. Cançado, A. Jorio, E. H. M. Ferreira, F. Stavale, C. A. Achete, R. B. Capaz, M. V. O. Moutinho, A. Lombardo, T. S. Kulmala, and A. C. Ferrari, "Quantifying Defects in Graphene via Raman Spectroscopy at Different Excitation Energies," *Nano Letters*, vol. 11, pp. 3190–3196, 2011.

88. A. J. Pollard, B. Brennan, H. Stec, B. J. Tyler, M. P. Seah, I. S. Gilmore, and D. Roy, "Quantitative characterization of defect size in graphene using Raman spectroscopy," *Applied Physics Letters*, vol. 105, p. 253107, dec 2014.

89. A. Eckmann, A. Felten, A. Mishchenko, L. Britnell, R. Krupke, K. S. Novoselov, and C. Casiraghi, "Probing the nature of defects in graphene by Raman spectroscopy.," *Nano Letters*, vol. 12, no. 8, pp. 3925–30, 2012.

90. A. Eckmann, A. Felten, I. Verzhbitskiy, R. Davey, and C. Casiraghi, "Raman study on defective graphene: Effect of the excitation energy, type, and amount of defects," *Physical Review B*, vol. 88, no. 3, p. 035426, 2013.

91. E. H. Martins Ferreira, M. V. O. Moutinho, F. Stavale, M. M. Lucchese, R. B. Capaz, C. A. Achete, and A. Jorio, "Evolution of the Raman spectra from single-, few-, and many-layer graphene with increasing disorder," *Physical Review B*, vol. 82, no. 12, p. 125429, 2010.

92. D. M. Basko, S. Piscanec, and a. C. Ferrari, "Electron-electron interactions and doping dependence of the two-phonon Raman intensity in graphene," *Physical Review B*, vol. 80, no. 16, p. 165413, 2009.

93. R. Beams, L. G. Cancado, and L. Novotny, "Low Temperature Raman Study of the Electron Coherence Length near Graphene Edges," *Nano Letters*, vol. 11, pp. 1177–1181, 2011.

94. H. Wang, Q. Wang, Y. Cheng, K. Li, Y. Yao, Q. Zhang, C. Dong, P. Wang, U. Schwingenschlögl, W. Yang, and X. X. Zhang, "Doping monolayer graphene with single atom substitutions.," *Nano Letters*, vol. 12, no. 1, pp. 141–4, 2012.

95. R. K. Joshi, P. Carbone, F. C. Wang, V. G. Kravets, Y. Su, I. V. Grigorieva, H. a. Wu, a. K. Geim, and R. R. Nair, "Precise and ultrafast molecular sieving through graphene oxide membranes.," *Science*, vol. 343, no. 6043, pp. 752–4, 2014.

96. F. Withers, M. Dubois, and a. K. Savchenko, "Electron properties of fluorinated single-layer graphene transistors," *Physical Review B - Condensed Matter and Materials Physics*, vol. 82, no. 7, pp. 1–4, 2010.

97. K. R. Paton, "Scalable production of large quantities of defect-free few-layer graphene by shear exfoliation in liquids," pp. 1–7, 2014.

98. A. J. Pollard, N. Kumar, A. Rae, S. Mignuzzi, W. Su, and D. Roy, "Nanoscale optical spectroscopy: an emerging tool for the character-

ization of graphene and related 2-D materials," *Journal of Materials NanoScience*, vol. 1, no. 1, pp. 39–49, 2014.

99. S. Mignuzzi, A. J. Pollard, N. Bonini, B. Brennan, I. S. Gilmore, M. A. Pimenta, D. Richards, and D. Roy, "Effect of disorder on Raman scattering of single-layer MoS_2," *Physical Review B*, vol. 91, p. 195411, 2015.

100. M. Bruna, A. K. Ott, M. Ijas, D. Yoon, U. Sassi, and A. C. Ferrari, "Doping dependence of the Raman spectrum of defected graphene," *ACS Nano*, vol. 8, no. 7, pp. 7432–7441, 2014.

101. A. Das, S. Pisana, B. Chakraborty, S. Piscanec, S. K. Saha, U. V. Waghmare, K. S. Novoselov, H. R. Krishnamurthy, A. K. Geim, A. C. Ferrari, and A. K. Sood, "Monitoring dopants by Raman scattering in an electrochemically top-gated graphene transistor.," *Nature Nanotechnology*, vol. 3, no. 4, pp. 210–5, 2008.

102. F. Schedin, a. K. Geim, S. V. Morozov, E. W. Hill, P. Blake, M. I. Katsnelson, and K. S. Novoselov, "Detection of individual gas molecules adsorbed on graphene.," *Nature Materials*, vol. 6, no. 9, pp. 652–5, 2007.

103. Y. Shi, X. Dong, P. Chen, J. Wang, and L. J. Li, "Effective doping of single-layer graphene from underlying SiO2 substrates," *Physical Review B - Condensed Matter and Materials Physics*, vol. 79, no. 11, pp. 1–4, 2009.

104. C. Georgi and A. Hartschuh, "Tip-enhanced Raman spectroscopic imaging of localized defects in carbon nanotubes," *Applied Physics Letters*, vol. 97, no. 14, p. 143117, 2010.

105. C. Chen, N. Hayazawa, and S. Kawata, "A 1.7 nm resolution chemical analysis of carbon nanotubes by tip-enhanced Raman imaging in the ambient.," *Nature Communications*, vol. 5, p. 3312, 2014.

106. N. Kumar, B. Stephanidis, R. Zenobi, A. J. Wain, and D. Roy, "Nanoscale Mapping of Catalytic Activity Using Tip-enhanced Raman Spectroscopy," *Nanoscale*, 2015.

107. L. G. Cançado, A. Jorio, A. Ismach, E. Joselevich, A. Hartschuh, and L. Novotny, "Mechanism of Near-Field Raman Enhancement in One-Dimensional Systems," *Physical Review Letters*, vol. 103, no. 18, p. 186101, 2009.

108. R. V. Maximiano, R. Beams, L. Novotny, A. Jorio, and L. G. Cançado, "Mechanism of near-field Raman enhancement in two-dimensional systems," *Physical Review B*, vol. 85, no. 23, p. 235434, 2012.

109. R. Beams, L. G. Cançado, S.-H. Oh, A. Jorio, and L. Novotny, "Spatial Coherence in Near-Field Raman Scattering," *Physical Review Letters*, vol. 113, no. 18, p. 186101, 2014.

110. L. G. Cançado, R. Beams, A. Jorio, and L. Novotny, "Theory of Spatial Coherence in Near-Field Raman Scattering," *Physical Review X*, vol. 4, no. 3, p. 031054, 2014.

111. F. Demming, J. Jersch, K. Dickmann, and P. I. Geshev, "Calculation of the field enhancement on laser-illuminated scanning probe tips by the boundary element method," *Applied Physics B: Lasers and Optics*, vol. 66, no. 5, pp. 593–598, 1998.

112. P. I. Geshev, S. Klein, T. Witting, K. Dickmann, and M. Hietschold, "Calculation of the electric-field enhancement at nanoparticles of arbitrary shape in close proximity to a metallic surface," *Physical Review B - Condensed Matter and Materials Physics*, vol. 70, no. 7, p. 075402, 2004.

113. C. Sönnichsen, S. Geier, N. E. Hecker, G. von Plessen, J. Feldmann, H. Ditlbacher, B. Lamprecht, J. R. Krenn, F. R. Aussenegg, V. Z.-H. Z.-H. Chan, J. P. Spatz, and M. Möller, "Spectroscopy of single metallic nanoparticles using total internal reflection microscopy," *Applied Physics Letters*, vol. 77, no. 19, pp. 2949—-2951, 2000.

114. T. Mino, Y. Saito, and P. Verma, "Quantitative Analysis of Polarization- Controlled Tip-Enhanced Raman Imaging through the

Evaluation of the Tip Dipole," *ACS Nano*, vol. 8, no. 10, pp. 10187–10195, 2014.

115. N. Behr and M. B. Raschke, "Optical antenna properties of scanning probe tips: Plasmonic light scattering, tip-sample coupling, and near-field enhancement," *Journal of Physical Chemistry C*, vol. 112, no. 10, pp. 3766–3773, 2008.

116. D. Roy, C. M. Williams, and K. Mingard, "Single-crystal gold tip for tip-enhanced Raman spectroscopy," *Journal of Vacuum Science & Technology B: Microelectronics and Nanometer Structures*, vol. 28, no. 3, p. 631, 2010.

117. L. Novotny and S. J. Stranick, "Near-field optical microscopy and spectroscopy with pointed probes.," *Annual Review of Physical Chemistry*, vol. 57, pp. 303–331, 2006.

118. E. Ru and P. Etchegoin, *Principles of surface-enhanced Raman spectroscopy and related plasmonic effects*. Elsevier, 2009.

119. E. Bailo and V. Deckert, "Tip-enhanced Raman spectroscopy of single RNA strands: towards a novel direct-sequencing method.," *Angewandte Chemie (International ed. in English)*, vol. 47, no. 9, pp. 1658–61, 2008.

120. M. Tsuboi, J. M. Benevides, and G. J. Thomas, "Raman tensors and their application in structural studies of biological systems.," *Proceedings of the Japan Academy. Series B, Physical and biological sciences*, vol. 85, no. 3, pp. 83–97, 2009.

121. M. Tsuboi, T. Ueda, K. Ushizawa, Y. Ezaki, S. a. Overman, and G. J. Thomas, "Raman tensors for the tryptophan side chain in proteins determined by polarized Raman microspectroscopy of oriented N-acetyl-l-tryptophan crystals," *Journal of Molecular Structure*, vol. 379, no. 95, pp. 43–50, 1996.

122. W. Hayes and R. Loudon, *Scattering of Light by Crystals*. John Wiley and Sons Inc., 1978.

123. E. Betzig and R. J. Chichester, "Single molecules observed by near-field scanning optical microscopy.," *Science*, vol. 262, no. 5138, pp. 1422–1425, 1993.

124. J. a. Veerman, M. F. Garcia-Parajo, L. Kuipers, and N. F. Van Hulst, "Single molecule mapping of the optical field distribution of probes for near-field microscopy," *Journal of Microscopy*, vol. 194, no. 2-3, pp. 477–482, 1999.

125. C. W. Hollars and R. C. Dunn, "Probing single molecule orientations in model lipid membranes with near-field scanning optical microscopy," *Journal of Chemical Physics*, vol. 112, no. 18, pp. 7822–7830, 2000.

126. N. F. van Hulst, J.-A. Veerman, M. F. Garcia-Parajo, Kuipers, and L. (Kobus), "Analysis of individual (macro)molecules and proteins using near-field optics," *Journal of Chemical Physics*, vol. 112, no. 18, pp. 7799–7810, 2000.

127. F. M. Huang, F. Festy, and D. Richards, "Tip-enhanced fluorescence imaging of quantum dots," *Applied Physics Letters*, vol. 87, no. 18, pp. 1–3, 2005.

128. P. Anger, P. Bharadwaj, and L. Novotny, "Enhancement and quenching of single-molecule fluorescence," *Physical Review Letters*, vol. 96, no. 11, pp. 3–6, 2006.

129. F. M. Huang and D. Richards, "Fluorescence enhancement and energy transfer in apertureless scanning near-field optical microscopy," *Journal of Optics A: Pure and Applied Optics*, vol. 8, no. 4, pp. S234–S238, 2006.

130. P. Giannozzi, S. Baroni, N. Bonini, M. Calandra, R. Car, C. Cavazzoni, D. Ceresoli, G. L. Chiarotti, M. Cococcioni, I. Dabo, A. Dal Corso, S. de Gironcoli, S. Fabris, G. Fratesi, R. Gebauer, U. Gerstmann, C. Gougoussis, A. Kokalj, M. Lazzeri, L. Martin-Samos, N. Marzari, F. Mauri, R. Mazzarello, S. Paolini, A. Pasquarello, L. Paulatto, C. Sbraccia, S. Scandolo, G. Sclauzero, A. P. Seitsonen, A. Smogunov,

P. Umari, and R. M. Wentzcovitch, "QUANTUM ESPRESSO: a modular and open-source software project for quantum simulations of materials.," *Journal of Physics: Condensed Matter*, vol. 21, p. 395502, 2009.

131. J. P. Perdew and A. Zunger, "Self-interaction correction to density-functional approximations for many-electron systems," *Physical Review B*, vol. 23, no. 10, pp. 5048–5079, 1981.

132. N. Blanc, F. Jean, A. V. Krasheninnikov, G. Renaud, and J. Coraux, "Strains Induced by Point Defects in Graphene on a Metal," *Physical Review Letters*, vol. 111, no. 8, p. 085501, 2013.

133. B. Chakraborty, A. Bera, D. V. S. Muthu, S. Bhowmick, U. V. Waghmare, and A. K. Sood, "Symmetry-dependent phonon renormalization in monolayer MoS_2 transistor," *Physical Review B*, vol. 85, no. 16, p. 161403(R), 2012.

134. C. Rice, R. J. Young, R. Zan, U. Bangert, D. Wolverson, T. Georgiou, R. Jalil, and K. S. Novoselov, "Raman-scattering measurements and first-principles calculations of strain-induced phonon shifts in monolayer MoS_2," *Physical Review B*, vol. 87, no. 8, p. 081307(R), 2013.

135. E. Scalise, M. Houssa, G. Pourtois, V. AfanasâĂšev, and A. Stesmans, "First-principles study of strained 2D MoS_2," *Physica E*, vol. 56, pp. 416–421, 2014.

136. E. Asari, I. Kamioka, K. G. Nakamura, T. Kawabe, W. A. Lewis, and M. Kitajima, "Lattice disordering in graphite under rare-gas ion irradiation studied by Raman spectroscopy," *Physical Review B*, vol. 49, no. 2, pp. 1011–1015, 1994.

137. K. Ishioka, K. G. Nakamura, and M. Kitajima, "Phonon confinement in GaAs by defect formation studied by real-time Raman measurements," *Physical Review B*, vol. 52, no. 4, pp. 2539–2542, 1995.

138. H. Richter, Z. P. Wang, and L. Ley, "The One Phonon Raman Spectrum in Microcrystalline Silicon," *Solid State Communications*, vol. 39, pp. 625–629, 1981.

139. I. H. Campbell and P. M. Fauchet, "The Effects of Microcrystal Size and Shape on the One Phonon Raman Spectra of Crystalline Semiconductors," *Solid State Communications*, vol. 58, no. 10, pp. 739–741, 1986.

140. S. Piscanec, M. Cantoro, a. Ferrari, J. Zapien, Y. Lifshitz, S. Lee, S. Hofmann, and J. Robertson, "Raman spectroscopy of silicon nanowires," *Physical Review B*, vol. 68, no. 24, p. 241312, 2003.

141. H. J. Conley, B. Wang, J. I. Ziegler, R. F. Haglund, S. T. Pantelides, and K. I. Bolotin, "Bandgap engineering of strained monolayer and bilayer MoS_2.," *Nano Letters*, vol. 13, no. 8, pp. 3626–30, 2013.

142. G. L. Frey, R. Tenne, M. J. Matthews, M. S. Dresselhaus, and G. Dresselhaus, "Optical properties of MS2 (M=Mo, W) inorganic fullerene-like and nanotube material optical absorption and resonance Raman measurements," *Journal of Materials Research*, vol. 13, no. 9, pp. 2412–2417, 1998.

143. E. del Corro, H. Terrones, A. Elias, C. Fantini, S. Feng, M. A. Nguyen, T. E. Mallouk, M. Terrones, and M. A. Pimenta, "Excited Excitonic States in 1L, 2L, 3L, and Bulk WSe_2 Observed by Resonant Raman Spectroscopy," *ACS Nano*, no. 9, pp. 9629–9635, 2014.

144. J. Liu, Q. Li, Y. Zou, Q. Qian, Y. Jin, G. Li, K. Jiang, and S. Fan, "The dependence of graphene Raman D-band on carrier density.," *Nano Letters*, vol. 13, no. 12, pp. 6170–5, 2013.

145. T. Livneh and E. Sterer, "Resonant Raman scattering at exciton states tuned by pressure and temperature in 2H-MoS_2," *Physical Review B*, vol. 81, no. 19, p. 195209, 2010.

146. T. J. Wieting and J. L. Verble, "Infrared and Raman Studies of Long-Wavelength Optical Phonons in Hexagonal MoS_2," *Physical Review B*, vol. 3, no. 12, pp. 4286–4292, 1971.

147. A. Molina-Sánchez and L. Wirtz, "Phonons in single-layer and few-layer MoS_2 and WS_2," *Physical Review B*, vol. 84, no. 15, p. 155413, 2011.

148. B. C. Windom, W. G. Sawyer, and D. W. Hahn, "A Raman Spectroscopic Study of MoS_2 and MoO3: Applications to Tribological Systems," *Tribology Letters*, vol. 42, no. 3, pp. 301–310, 2011.

149. J. M. Chen and C. S. Wang, "Second Order Raman Spectrum of MoS_2," *Solid State Communications*, vol. 14, pp. 857–860, 1974.

150. Q. C. Sun, D. Mazumdar, L. Yadgarov, R. Rosentsveig, R. Tenne, and J. L. Musfeldt, "Spectroscopic determination of phonon lifetimes in rhenium-doped MoS_2 nanoparticles.," *Nano Letters*, vol. 13, no. 6, pp. 2803–8, 2013.

151. L. Sun, J. Yan, D. Zhan, L. Liu, H. Hu, H. Li, B. K. Tay, J.-L. Kuo, C.-C. Huang, D. W. Hewak, P. S. Lee, and Z. X. Shen, "Spin-Orbit Splitting in Single-Layer MoS_2 Revealed by Triply Resonant Raman Scattering," *Physical Review Letters*, vol. 111, no. 12, p. 126801, 2013.

152. N. T. McDevitt, J. S. Zabinski, and M. S. Donley, "The use of Raman scattering to study disorder in pulsed laser deposited MoS_2 films," *Thin Solid Films*, vol. 240, pp. 76–81, 1994.

153. G. L. Frey, R. Tenne, M. J. Matthews, M. S. Dresselhaus, and G. Dresselhaus, "Raman and resonance Raman investigation of MoS_2 nanoparticles," *Physical Review B*, vol. 60, no. 4, pp. 2883–2892, 1999.

154. A. Berkdemir, H. R. Gutiérrez, A. R. Botello-Méndez, N. Perea-López, A. L. Elías, C.-I. Chia, B. Wang, V. H. Crespi, F. López-Urías, J.-C. Charlier, H. Terrones, and M. Terrones, "Identification of individual and few layers of WS_2 using Raman spectroscopy.," *Scientific Reports*, vol. 3, p. 1755, 2013.

155. M. A. Pimenta, E. Corro, B. R. Carvalho, C. Fantini, and L. M. Malard, "Comparative Study of Raman Spectroscopy in Graphene and MoS_2-type Transition Metal Dichalcogenides," *Accounts of Chemical Research*, p. 253107, 2014.

156. P. Venezuela, M. Lazzeri, and F. Mauri, "Theory of double-resonant Raman spectra in graphene: Intensity and line shape of defect-induced and two-phonon bands," *Physical Review B*, vol. 84, no. 3, p. 035433, 2011.

157. S. J. Sandoval, D. Yang, R. F. Frindt, and J. C. Irwin, "Raman study and lattice dynamics of single molecular layers of MoS_2," *Physical Review B*, vol. 44, no. 8, pp. 3955–3962, 1991.

158. X. Zhang, W. P. Han, J. B. Wu, S. Milana, Y. Lu, Q. Q. Li, A. C. Ferrari, and P. H. Tan, "Raman spectroscopy of shear and layer breathing modes in multilayer MoS_2," *Physical Review B*, vol. 87, no. 11, p. 115413, 2013.

159. K. Golasa, M. Grzeszczyk, P. Leszczyński, C. Faugeras, A. A. L. Nicolet, A. Wysmołek, M. Potemski, and A. Babiński, "Multiphonon resonant Raman scattering in MoS_2," *Applied Physics Letters*, vol. 104, no. 9, p. 092106, 2014.

160. B. Carvalho, Y. Wang, S. Mignuzzi, D. Roy, M. Terrones, C. Fantini, V. H. Crespi, L. M. Malard, and M. A. Pimenta, "Intervalley scattering by acoustic phonons in two-dimensional MoS_2 revealed by double-resonance Raman spectroscopy," *Nature Communications*, vol. 8, p. 14670.

161. Q. Ma, P. M. Odenthal, J. Mann, D. Le, C. S. Wang, Y. Zhu, T. Chen, D. Sun, K. Yamaguchi, T. Tran, M. Wurch, J. L. McKinley, J. Wyrick, K. Magnone, T. F. Heinz, T. S. Rahman, R. Kawakami, and L. Bartels, "Controlled argon beam-induced desulfurization of monolayer molybdenum disulfide.," *Journal of physics: Condensed Matter*, vol. 25, no. 25, p. 252201, 2013.

162. S. Tongay, J. Suh, C. Ataca, W. Fan, A. Luce, J. S. Kang, J. Liu, C. Ko, R. Raghunathanan, J. Zhou, F. Ogletree, J. Li, J. C. Grossman, and J. Wu, "Defects activated photoluminescence in two-dimensional semiconductors: interplay between bound, charged, and free excitons.," *Scientific Reports*, vol. 3, p. 2657, 2013.

163. P. K. Chow, R. B. Jacobs-gedrim, J. Gao, T.-M. Lu, B. Yu, and H. Terrones, "Defect-Induced Photoluminescence in Monolayer Semiconducting Transition Metal Dichalcogenides," *ACS Nano*, no. Xx, 2015.